The Thermal Structure, Dust Loading, and Meridional Transport in the Martian Atmosphere During Late Southern Summer

Thesis by

Michelle Santee

In Partial Fulfillment of the Requirements

for the Degree of

Doctor of Philosophy

California Institute of Technology

Pasadena, California

1993

(Defended 19 June 1992)

©1993

Michelle Santee

All Rights Reserved

Acknowledgments

I would like to express my gratitude first and foremost to Dave Crisp — mentor and friend, advisor and confidant, and machete–wielding editor — for suggesting this project in the first place, for guiding me when I needed it and leaving me alone when I needed it, and for finally recognizing the semicolon as a valid grammatical form. His fundamental understanding of the problem and his patient explanations and advice (not to mention thousands of lines of computer code) were essential to this work. I would also like to thank Andy Ingersoll, who served as my thesis advisor, for his enthusiasm for this project. I am deeply indebted to Bruce Murray, my academic advisor, for his sage counsel over the years, for his uncanny ability to know what I wanted before I did myself, and for taking me to Moscow! I would like to express my appreciation to Yuk Yung, not only for being an invaluable resource on a variety of subjects, but also for his humor and philosophy; to Dewey Muhleman, for his insight, his candid evaluations, and his encouragement at the times I needed it the most; and to Dave Paige, a frequent collaborator, for his boundless enthusiasm for Mariner 9 data in general and my work in particular. In addition, I would like to thank Kay Campbell for her gracious assistance in overcoming my handicap in filling out forms, and for her sympathy and efficiency whenever problems arose.

I would also like to thank many of my colleagues in graduate school: Rich Achterberg, for (on the whole) patiently enduring $4\frac{1}{2}$ years of incessant computer questions; Don Banfield, for always being willing to listen to me about my work, for always being willing to have a conversation (and we had many), and for being a consistently considerate and fun officemate; Bruce Betts, for being such a good comrade in Moscow, and for being the only one around here who seems to see things the way I do; Mike Black, for dropping everything else to attack my computer problems, and for keeping me apprised of upcoming concert events (Stevie!); Bridget Landry, for her

friendship, her unfailing sympathy and support, and her committment to the IDIC philosophy; Julie Moses, for her advice on a myriad of topics, and for keeping me informed about departmental goings–on; and Kathy Pierce Shah, for her insights into both Indian culture and homocidal maniacs, but most of all, for her fine appreciation of Hawaiian lava flows. Also thanks to Bill Anderson, Bryan Butler, Rich Dissly, Janusz Eluszkiewicz (if you don't credit my model I won't help you sell used American cars in Poland), Mimi Gerstell, Mark Gurwell, Mark Hofstadter, Dave Koerner, Steve Leroy, Stuart McMuldroch, Hari Nair (special thanks for help with the photochemical model results), Joel Schwartz, Stuart Stephens, Kim Tryka, and Laurie Watson for enlivening and enriching my time at Caltech. I hope you have found my acquaintance as rewarding as I have found yours.

I would also like to make special mention of friends outside of the planetary science department at Caltech who reminded me that there was, in fact, life outside of the planetary science department at Caltech. To Linda Czyzyk (I'll miss those Monday lunches), Susan Halsell, Lisa McLeod (the girls thank you too), Lisa Green, Lisa White, and Gayle Trager: thanks for listening, for cooking me dinner, or for just being there.

I can never express how much the love and support of my parents, Betty and Bill Hansen, has meant to me. In weekly phone calls to them I was variously optimistic and depressed, planning a long career and planning to quit the next day. My mom, however, never wavered in her belief that I would succeed and never failed to cheer me up. Finally, I offer my profound gratitude to Leigh Leonard, who always listened to me attentively no matter what I was ranting about, who never complained about doing all the chores, who put up with three months of *Achtung Baby* in continuous repeat mode, and who nurtured and cared for me. Every day with her has been a gift.

Abstract

This thesis consists of two papers, both of which investigate the state of the Martian atmosphere during a relatively clear period in late southern summer. The first paper describes a new technique for the simultaneous retrieval of atmospheric temperatures and dust abundances from thermal emission spectra. The second paper describes a diagnostic stream function model which is used with the temperature and dust results of the first paper to solve for the meridional and vertical components of the diabatic circulation simultaneously. The abstracts for the two papers are reproduced below.

PAPER I:

The temperature structure and dust loading of the Martian atmosphere are investigated using thermal emission spectra recorded by the Mariner 9 infrared interferometer spectrometer (IRIS). The analysis is restricted to a subset of the IRIS data consisting of approximately 2400 spectra in a 12–day period extending from $L_S = 343°$ to $L_S = 348°$, corresponding to late southern summer on Mars. Simultaneous retrieval of the vertical distribution of both atmospheric temperature and dust optical depth is accomplished through an iterative procedure which is performed on each spectrum. The inclusion of dust opacity in the retrieval algorithm causes the retrieved temperatures to change by more than 20 K in some atmospheric layers. The largest column–integrated 9 μm dust optical depths ($\sim$ 0.4) occur over the equatorial regions. The highest atmospheric temperatures ($>$ 260 K) are found at low altitudes near the sub–solar latitude ($\sim$ 6°S), while the coldest temperatures ($<$ 150 K) are found at levels near 1.0 mbar over the winter pole. A comparison of temperature maps for 2 PM and 2 AM indicates diurnal temperature variations as large as 80 K at low altitudes near the sub–solar latitude, whereas diurnal temperature changes at pressures less than 1.0 mbar are typically about 10 K. Both dayside and nightside

temperatures above about 0.1 mbar ($\sim$ 40 km) are warmer over the winter (north) polar region than over the equator or the summer (south) polar region. This thermal structure suggests the existence of a net zonally–averaged meridional circulation with rising motion at low latitudes, poleward flow at altitudes above 40 km, and subsidence over the poles. Because a meridional circulation transports atmospheric constituents as well as heat, it has significant implications for the net flux of dust and water into the polar regions.

PAPER II:

The circulation of the Martian atmosphere during late southern summer is calculated diagnostically from the observed atmospheric temperature distribution. We use global maps of temperature and dust optical depth ($\sim 0-60$ km) retrieved from a subset of the Mariner 9 IRIS thermal emission spectra spanning $L_S = 343° - 348°$ [*Santee and Crisp*, 1992]. This thermal structure is characterized by a reversed meridional temperature gradient (temperatures increasing poleward) at altitudes above about 40 km. Zonal–mean zonal winds are derived from the zonally–averaged temperatures assuming gradient wind balance and zero surface zonal wind. Both hemispheres have intense mid–latitude westerly jets (with velocities of 80–90 m/s near 50 km); in the southern tropics the winds are strongly easterly (with velocities of 100 m/s near 50 km). The north–south atmospheric transport includes contributions from the zonal–mean meridional circulation and large–scale waves. Their net effect can be approximated by the diabatic circulation, which is that circulation needed to maintain the observed temperature distribution (warm winter pole, cool tropics) in the presence of the radiative forcing. A radiative transfer model [*Crisp*, 1990] which accounts for absorption, emission and multiple scattering by particles and non–grey gases is used to compute the solar heating and thermal cooling rates from diurnal averages of the retrieved

IRIS temperature and dust distributions. At pressures below 4 mbar, there are large net heating rates (up to 8 K/day) in the equatorial region and large net cooling rates (up to 20 K/day) in the polar regions. These net heating rates are used in a diagnostic stream function model which solves for the meridional and vertical components of the diabatic circulation simultaneously. We find a two–cell circulation, with upwelling over the equator ($\sim$ 1.5 cm/s), poleward motion in both hemispheres ($\sim$ 2 m/s), and subsidence over the poles (1–2 cm/s). This circulation is sufficiently vigorous that the meridional transport time scale is $\sim$ 13 days. Vertical transport is primarily advective in nature, except in the high–altitude winter polar regions, where diffusive processes dominate. Water vapor desorbed from the low–latitude regolith during late northern winter/early northern spring may be transported upward by the ascending branch of this circulation, where it would be transported poleward by the high–altitude meridional winds. This process could provide a high–altitude source of water vapor for the polar hood.

Table of Contents

List of Figures

PAPER I:

PAPER II:

APPENDIX I:

PAPER I

The Thermal Structure and Dust Loading of the Martian Atmosphere During Late Southern Summer: Mariner 9 Revisited

The Thermal Structure and Dust Loading of the Martian Atmosphere During Late Southern Summer: Mariner 9 Revisited

Michelle Santee

Division of Geological and Planetary Sciences
California Institute of Technology
Pasadena, California 91125

and

David Crisp

Earth and Space Sciences Division
Jet Propulsion Laboratory, California Institute of Technology
Pasadena, California 91109

Submitted to: *J. Geophys. Res.*

Contribution number 5095 from the Division of Geological and Planetary Sciences, California Institute of Technology, Pasadena, California 91125.

Abstract

The temperature structure and dust loading of the Martian atmosphere are investigated using thermal emission spectra recorded by the Mariner 9 infrared interferometer spectrometer (IRIS). The analysis is restricted to a subset of the IRIS data consisting of approximately 2400 spectra in a 12–day period extending from $L_S = 343°$ to $L_S = 348°$, corresponding to late southern summer on Mars. Simultaneous retrieval of the vertical distribution of both atmospheric temperature and dust optical depth is accomplished through an iterative procedure which is performed on each spectrum. The inclusion of dust opacity in the retrieval algorithm causes the retrieved temperatures to change by more than 20 K in some atmospheric layers. The largest column–integrated 9 μm dust optical depths ($\sim$ 0.4) occur over the equatorial regions. The highest atmospheric temperatures ($>$ 260 K) are found at low altitudes near the sub–solar latitude ($\sim$ 6°S), while the coldest temperatures ($<$ 150 K) are found at levels near 1.0 mbar over the winter pole. A comparison of temperature maps for 2 PM and 2 AM indicates diurnal temperature variations as large as 80 K at low altitudes near the sub–solar latitude, whereas diurnal temperature changes at pressures less than 1.0 mbar are typically about 10 K. Both dayside and nightside temperatures above about 0.1 mbar ($\sim$ 40 km) are warmer over the winter (north) polar region than over the equator or the summer (south) polar region. This thermal structure suggests the existence of a net zonally–averaged meridional circulation with rising motion at low latitudes, poleward flow at altitudes above 40 km, and subsidence over the poles. Because a meridional circulation transports atmospheric constituents as well as heat, it has significant implications for the net flux of dust and water into the polar regions.

1. Introduction

The temperature structure of the Martian atmosphere has been investigated by a number of spacecraft–borne instruments. The only *in–situ* measurements were made by pressure and temperature sensors onboard the two Viking Landers during their parachute descent through the atmosphere [*Sieff and Kirk*, 1977]. Although the atmospheric structure is characterized very well by these entry profiles, they represent only two geographic locations and two Mars local times of day. A more complete description of the temperature distribution has been developed through several remote sensing experiments. Vertical temperature profiles obtained from the radio occultation experiments on both the Mariner 9 and Viking orbiters [*Kliore et al.*, 1972; *Lindal et al.*, 1979] have high vertical resolution, but they are few in number and consequently have limited spatial and temporal coverage. The 15 μm channel of the Viking Orbiter infrared thermal mapper (IRTM) also provided an estimate of the atmospheric temperature [*Martin and Kieffer*, 1979; *Martin*, 1981], but this instrument sampled a single vertically–extended layer defined by a broad instrumental weighting function centered at about the 25 km level.

The best existing data set for studying the vertical structure of the Martian atmosphere on a global scale was collected by the infrared interferometer spectrometer (IRIS) carried by the Mariner 9 spacecraft in 1971–1972. This instrument measured the thermal emission of Mars with high spectral resolution. Most of the measurements were obtained just past the peak of a severe global dust storm; however, a smaller number of spectra were recorded during and after the decay phase of the storm. Preliminary estimates of atmospheric and surface temperature and pressure, water vapor abundance, dust content, and wind fields have been reported for segments of the IRIS data set [*Hanel et al.*, 1972a; *Conrath et al.*, 1973; *Conrath*, 1975, 1976, 1981], but the majority of these studies focused on observations obtained during the

dustiest conditions. Despite the high dust content of the atmosphere at that time, the early studies neglected the effects of dust absorption in estimating atmospheric temperatures.

Several experimental and theoretical advances have been made since the first IRIS results were published. The AFGL HITRAN database of molecular absorption parameters, including the positions, strengths, and widths of spectral lines, has been established and periodically updated; the edition used here became available in 1986 [*Rothman et al.*, 1987]. The composition and optical properties of the dust suspended in the Martian atmosphere have been better defined [*Toon et al.*, 1977; *Evans and Adams*, 1979; *Singer*, 1982]. Recent refinements in radiative transfer modeling theory [*Crisp*, 1990] greatly reduce the computational time involved in calculating CO_2 transmittances. We have incorporated these changes into a new remote sensing retrieval algorithm which explicitly accounts for the temperature dependence of the CO_2 transmittances and the additional opacity within the CO_2 15 μm band due to atmospheric dust. Taken together, these factors significantly improve the accuracy of the temperature retrievals, and permit the simultaneous estimation of airborne dust abundances.

In this paper we present the first self-consistent, global description of the thermal structure and dust loading of the Martian atmosphere, from the surface to approximately 60 km. These results reinforce and expand upon the conclusions reached by earlier studies of the Martian environment using both Mariner 9 IRIS data (*e.g.*, *Hanel et al.*, 1972a; *Conrath et al.*, 1973; *Conrath*, 1975; 1981) and Viking data (*e.g.*, *Martin*, 1981; 1986; *Martin and Kieffer*, 1979). The new retrieval algorithm was implemented on a set of IRIS observations taken near the end of the Mariner 9 nominal mission, after the global dust storm had abated and airborne dust amounts had subsided to background values. We concentrated on this period because dust

storms of the magnitude of the 1971 event are rare [*Zurek*, 1982], and IRIS measurements recorded under clearer conditions are more representative of the typical Martian climate. In addition, under relatively clear conditions the temperature and dust retrievals are only weakly coupled and the retrieval process is simplified.

2. Mariner 9 IRIS Data Set

The Mariner 9 spacecraft began its mission at Mars in November 1971. Its orbit had a period of 12 hours, an inclination of 64°, an eccentricity of 0.62, and a periapsis altitude of 1400 km [*Lorell et al.*, 1972]. The subspacecraft longitude drifted eastward at a rate of $\sim$ 9°/day. The Mariner 9 IRIS instrument was a Michelson interferometer designed to record thermal emission spectra in the range 200 cm^{-1} to 2000 cm^{-1} (5 μm to 50 μm). The spectra are sampled at a resolution of 1.2 cm^{-1}, but they have an apodized spectral resolution of 2.4 cm^{-1} [*Hanel et al.*, 1972b]. The field of view was $\sim$ 4.5°, corresponding to a spatial resolution for nadir viewing of approximately 110 km diameter at periapsis.

During its almost one–year operational lifetime the IRIS instrument recorded over 21,000 thermal emission spectra, although it did not observe Mars through a complete seasonal cycle. The measurements obtained during the primary mission (November 1971 through March 1972) describe northern winter/southern summer; the sporadic data taken during the extended mission (the last spectrum was recorded in October 1972) provide constraints on the atmospheric behavior during later seasons. The dust storm which began three months before the arrival of Mariner 9 was probably the most severe global dust event ever observed [*Zurek*, 1982]. The atmosphere was extremely dust–laden during much of the Mariner 9 primary mission, but *Hanel et al.* [1972a] report that the dust was dissipating by Orbit 92 (December 1971, $L_S = 319°$), and clearing was well advanced by Orbit 174 (February 1972, $L_S = 341°$).

We have examined a subset of the IRIS data consisting of approximately 2400

spectra in a 12–day period extending from $L_S = 343°$ to $L_S = 348°$ (Orbits 180–200), corresponding to late southern summer on Mars. During this period the subsolar latitude was $\sim 6°$ S. Coverage of the subset of data is displayed as a function of Mars local time of day and latitude in Figure 1a. The sparse temporal sampling at most latitudes, especially in the equatorial regions, precludes examination of complete diurnal cycles. Coverage is most extensive at the high northern latitudes, whereas coverage in the southernmost latitudes is restricted to the morning hours. The incomplete sampling complicates the interpretation of global temperature maps by superimposing a time–of–day bias on meridional temperature variations. Similarly, Figure 1b shows the coverage of the data set with time of day and longitude. Only a narrow range of longitudes is represented for any given hour of local time. The diversity of surface characteristics (thermal inertia, albedo, topography) at different longitudes hinders comparisons of low–altitude temperatures retrieved from spectra taken at the same latitude but different times of day. This point is reinforced in Figure 1c, which shows the spatial (latitude/longitude) distribution of the spectra in the data subset. Figure 1d shows the distribution of viewing (or zenith) angle with time of day. Observations made under conditions of vertical viewing were obtained only during late morning and afternoon hours. This situation, combined with the fact that periapsis was achieved in the early afternoon, resulted in low spatial resolution for late night and early morning spectra.

The relationship between the vertical profile of atmospheric temperature and the emergent radiance can be seen qualitatively by examining the equivalent brightness temperatures calculated from observed radiances using Planck's law. Brightness temperatures from four sample IRIS spectra in the data subset are displayed in Figure 2 to illustrate the variation in thermal emission with geographic location, local time, and atmospheric dust loading. The first example is a tropical, mid–day spec-

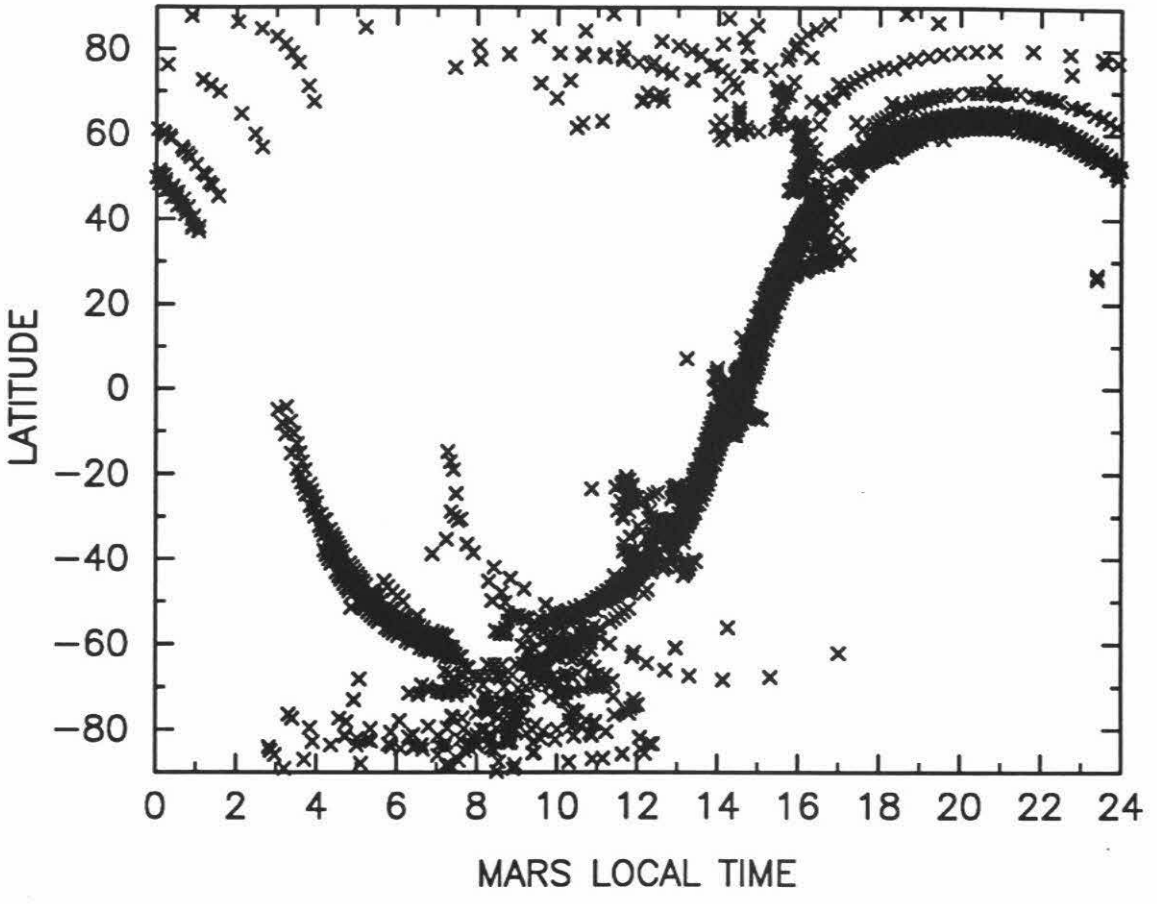

Figure 1a. Coverage of the subset of Mariner 9 IRIS data as a function of Mars local time of day and latitude. This subset of data consists of approximately 2400 spectra spanning $L_S = 343° - 348°$, corresponding to late southern summer on Mars. Spectra in the data set for which the proportion of the field–of–view filled by Mars was less than one or the viewing angle was greater than 80° were discarded.

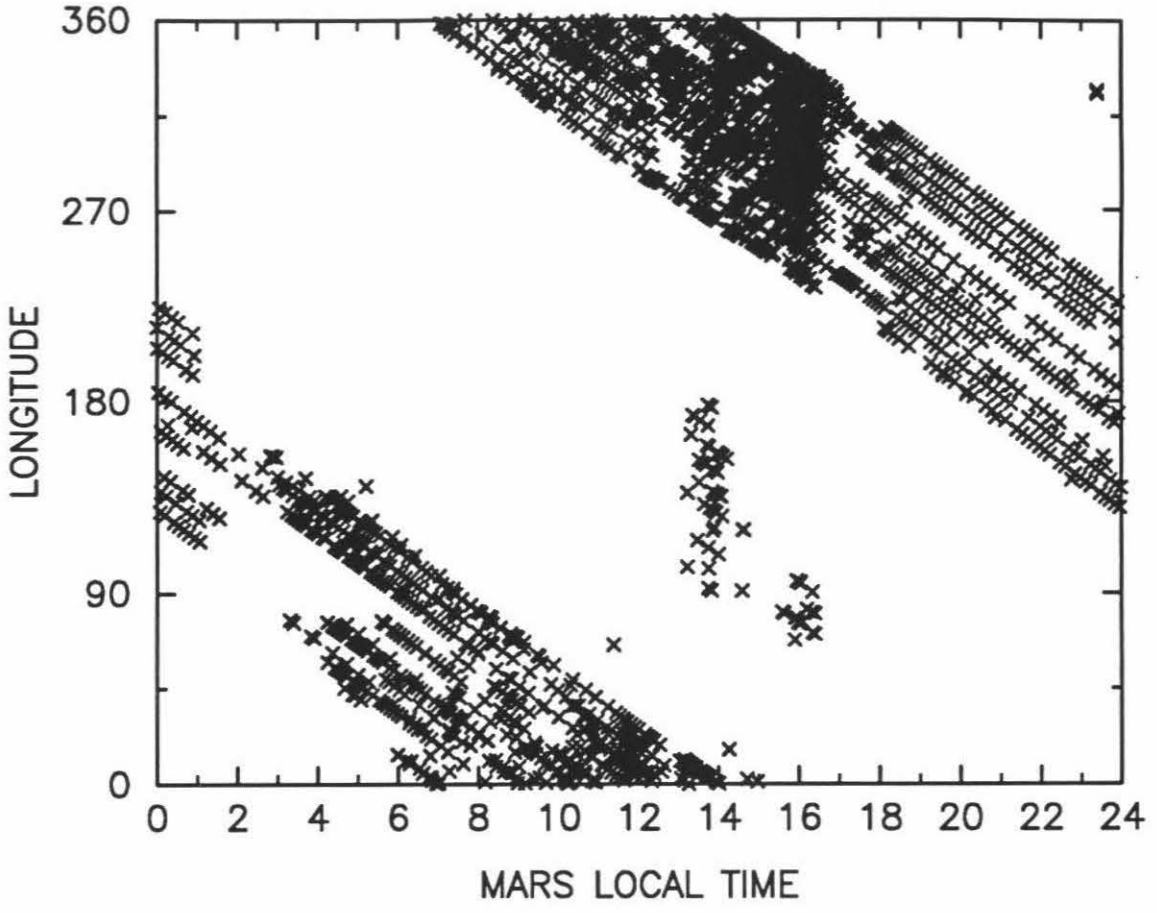

Figure 1b. Same as Figure 1a, for longitude.

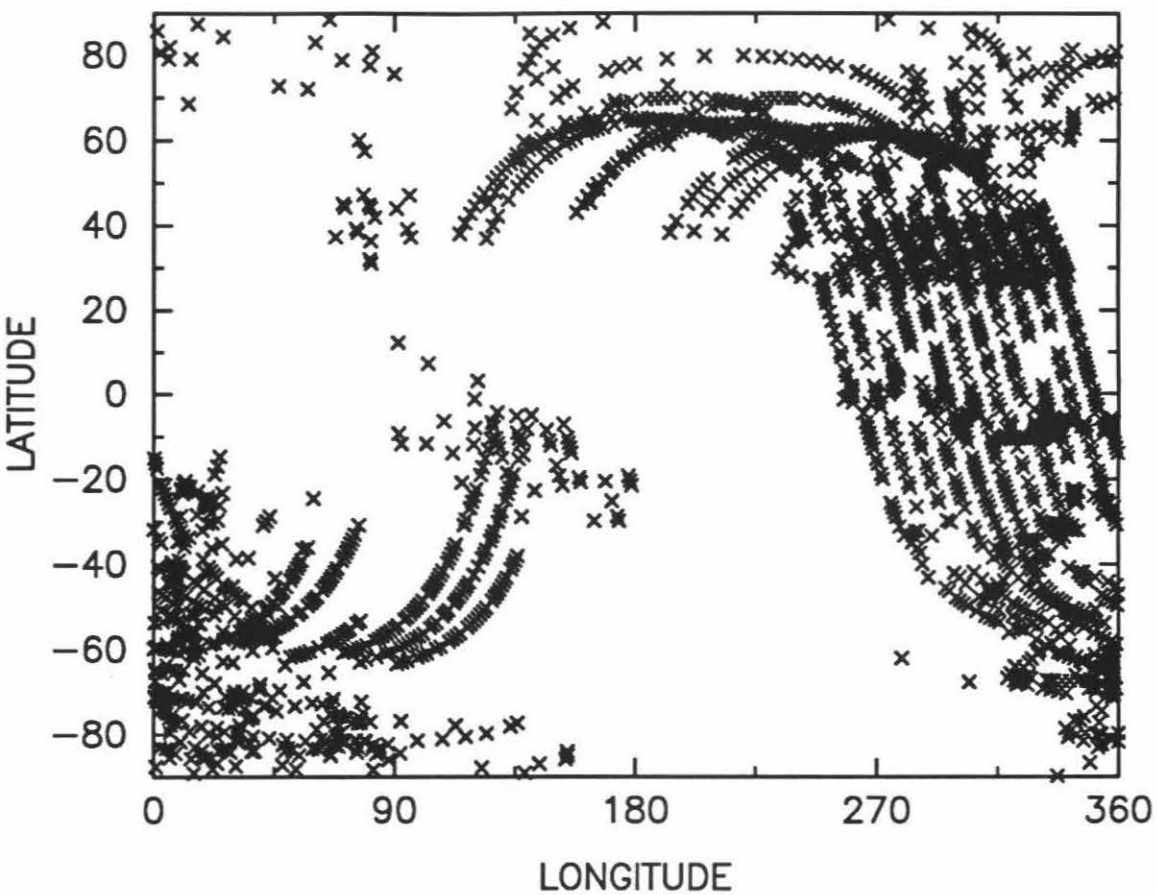

Figure 1c. Coverage of the subset of Mariner 9 IRIS data as a function of longitude and latitude.

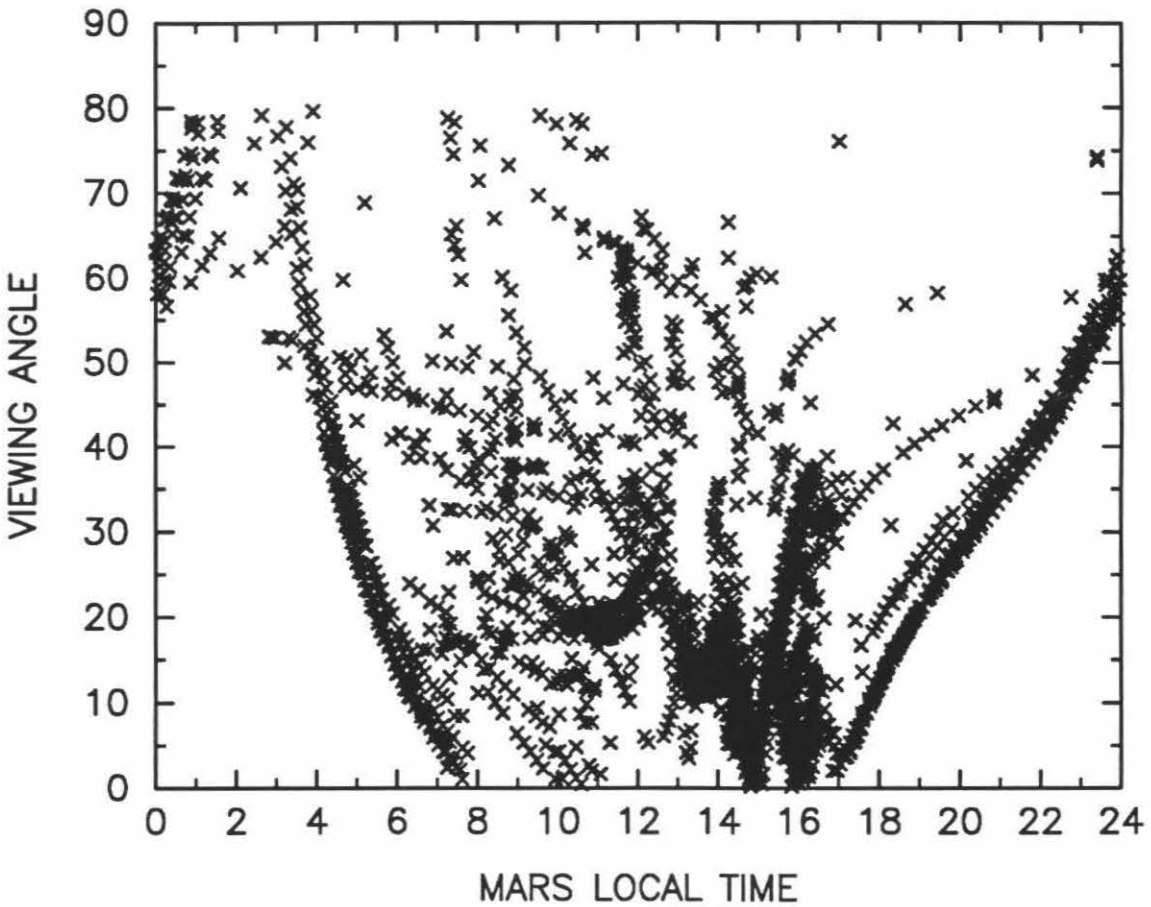

Figure 1d. Same as Figure 1a, for viewing angle.

trum (Figure 2a). The prominent feature which extends from about 600 to 800 cm^{-1} is due to absorption by atmospheric CO_2. This feature includes the strong ν_2 bending fundamental of the principal isotope ($^{12}C^{16}O_2$), centered at 667 cm^{-1} (15 μm), and a number of weaker hot and isotopic bands. Outside of this band, the background continuum provides an estimate of the surface temperature, although the absorption by airborne dust must be taken into account. The shape of this spectrum indicates that the surface is warmer than the bulk of the atmosphere. A second, very shallow, absorption feature near 1100 cm^{-1} (9 μm) is more obvious in the dusty spectrum (Figure 2b). This feature has been attributed to absorption by silicate minerals in the airborne dust [*Hanel et al.*, 1972a; *Conrath et al.*, 1973; *Toon et al.*, 1977]. Although this spectrum was recorded at roughly the same latitude and time of day as the first spectrum, the increased abundance of airborne dust resulted in slightly lower surface brightness temperatures. Two different mechanisms contribute to the lower daytime surface brightness temperatures measured under dustier conditions: (1) the solar radiation reaching the surface is reduced, resulting in lower actual temperatures, and (2) the thermal radiation emitted by the surface is attenuated, resulting in recorded temperatures which are lower than the actual temperatures.

The CO_2 band appears in emission in the evening polar spectrum (Figure 2c), indicating that the atmosphere was warmer than the underlying surface when this spectrum was taken. The small amplitude of the spike at 667 cm^{-1}, which corresponds to the Q–branch of the ν_2 fundamental, implies that the upper and lower regions of the atmosphere are at about the same temperature. The last example is a late–night polar spectrum (Figure 2d). The higher brightness temperatures on either side of 667 cm^{-1} are indicative of a low–level temperature inversion, and the apparent absence of the Q–branch signifies that the upper atmosphere is at about the same temperature as the surface. The relationship between the vertical temperature profile

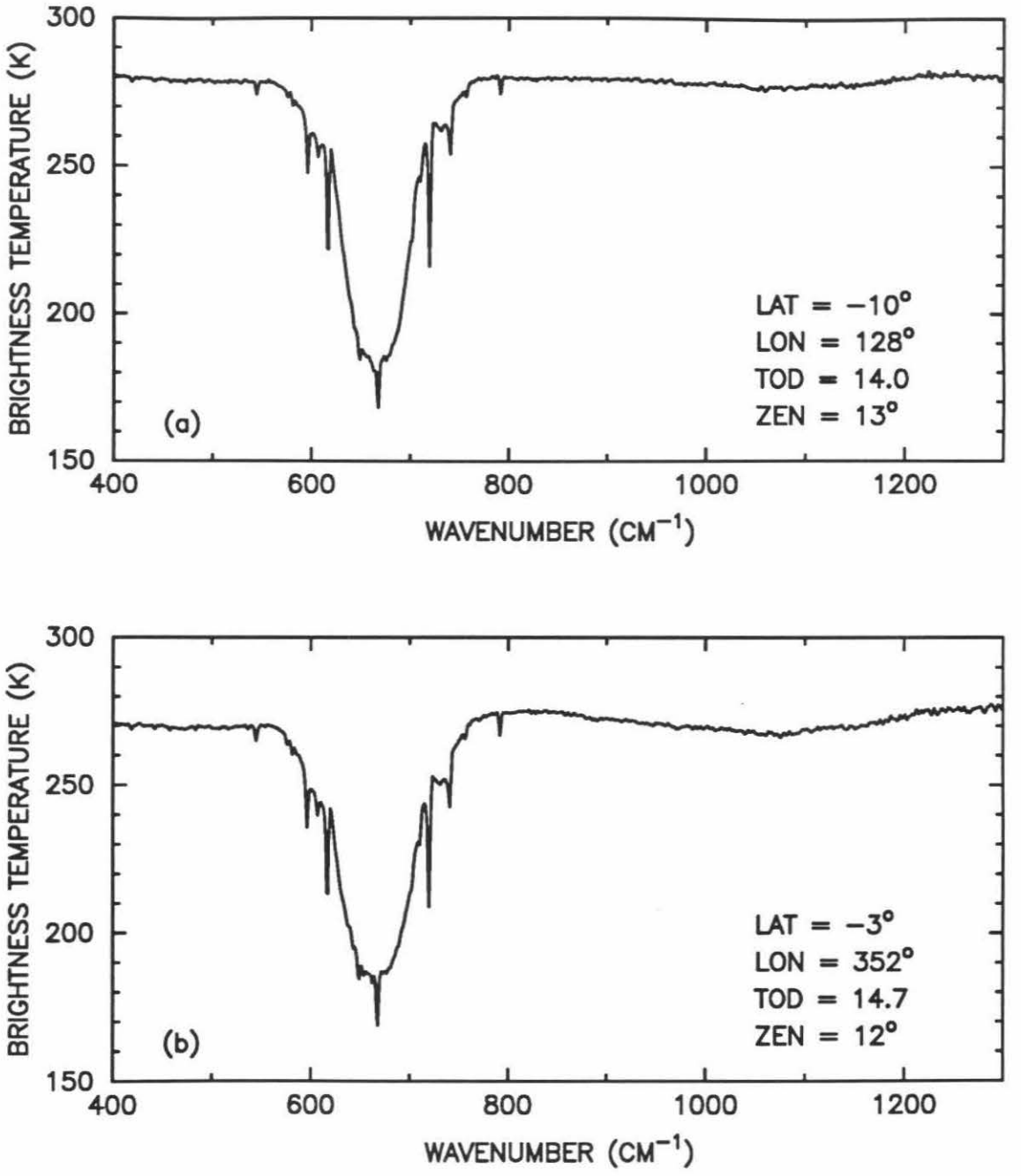

Figure 2a,b. Brightness temperatures calculated from four observed IRIS radiance spectra, representing different geographic locations, local times, and atmospheric dust abundances. All plots have the same horizontal and vertical scales. (a) tropical, mid–day spectrum. The strong absorption feature centered at 667 cm^{-1} (15 μm) is due to atmospheric CO_2. (b) dusty spectrum. The shallow absorption feature near 1100 cm^{-1} (9 μm) is due to silicate minerals in the airborne dust.

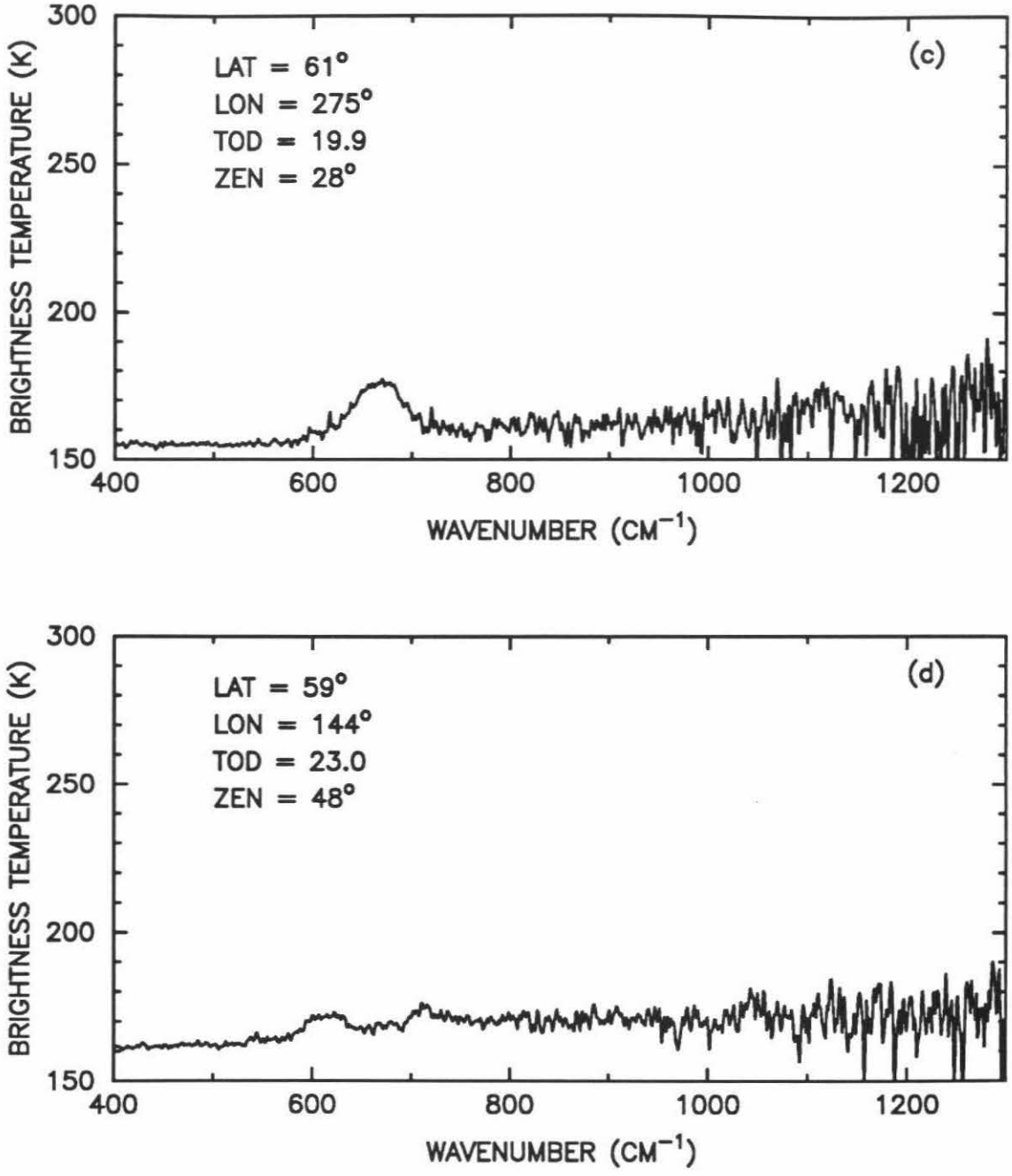

Figure 2c,d. (c) evening polar spectrum. (d) late–night polar spectrum. The high–wavenumber structure in the polar spectra indicates that they are much noisier than the warmer low–latitude spectra.

and the thermal emission spectrum is examined more quantitatively in the following section.

3. Methods of Data Analysis

3.1 Radiative Transfer Equation

Retrieval of atmospheric properties from thermal emission spectra is possible because the upwelling thermal radiance measured at the top of the atmosphere depends on the distribution of both the constituents (emitting and absorbing) and the temperatures throughout the atmosphere and at the surface. The region of the spectrum observed by the Mariner 9 IRIS instrument includes the strong CO_2 absorption band centered at 15 μm (667 cm^{-1}) and a silicate absorption feature centered at 9 μm (1100 cm^{-1}). In the 15 μm region, the atmosphere produces virtually all of the emitted radiance, and there is relatively little emission by atmospheric constituents other than CO_2 [*Crisp*, 1990]. Because the CO_2 mixing ratio is constant and well known, the observed radiances in the 15 μm band can be used to derive the vertical distribution of atmospheric temperatures. Alternatively, if the temperature distribution of the atmosphere is known, and if the wavelength–dependent dust optical properties have been determined, then the 9 μm silicate feature can be used to estimate the atmospheric dust abundance.

The monochromatic radiance, $I(\nu)$, measured at a spacecraft is described by the equation of radiative transfer (*cf.*, *Liou*, 1980, *p.* 25; *Goody and Yung*, 1989, *p.* 47). The following simplifying assumptions are made to solve this equation: (1) atmospheric scattering processes are ignored, because our calculations indicate that the single scattering albedo is less than 0.1 over most of the wavelength range studied here, (2) the planetary surface is modeled as a grey body with an emissivity near unity [*Kieffer*, 1976], so that the small amount of atmospheric thermal radiation

reflected from the surface can be neglected, and (3) local thermodynamic equilibrium is assumed to hold for the 15 μm band of CO_2 at all altitudes. This last assumption may not be valid at altitudes above 70 km [*Zurek et al., in press*], but this does not introduce significant error because emission from these altitudes contributes little to the IRIS spectra. The radiative transfer equation can then be written in the form:

$$I(\nu) = \epsilon B[\nu, T_s]\, \mathcal{T}(\nu, p_s) + \int_{\ln p_s}^{\ln p_t} B[\nu, T(p)] \frac{\partial \mathcal{T}(\nu, p)}{\partial(\ln p)}\, d(\ln p)\,, \qquad (1)$$

where $\mathcal{T}(\nu, p)$ is the monochromatic transmittance between any pressure level, p, and the top of the atmosphere. Calculation of the transmittances is discussed in more detail in the next section. The subscripts "s" and "t" denote values at the surface and at the top of the atmosphere, respectively, ϵ is the grey–body surface emissivity, and $B[\nu, T]$ is the Planck function at wavenumber ν and temperature T, given by:

$$B[\nu, T(p)] = \frac{2\, h\, c^2\, \nu^3}{\left\{\exp\left(\frac{h c \nu}{k T(p)}\right) - 1\right\}}\,. \qquad (2)$$

The first term on the right hand side of equation (1) represents the attenuation of the radiation emitted by the surface as it traverses a path through the atmosphere. The second term accounts for the atmospheric contribution to the total thermal emission. This atmospheric component is the weighted integral of the Planck function, where the weighting functions are the derivatives of the atmospheric transmittances.

3.2 Atmospheric Transmittances

The atmospheric transmittance along an optical path extending from pressure level p to space represents the probability that a photon emitted at that pressure will reach space before being absorbed. If the atmosphere is assumed to be plane–parallel and hydrostatic, the gas transmittance, $\mathcal{T}_g(\nu, p)$, within a finite spectral interval of width $\Delta\nu$ can be expressed as:

$$\mathcal{T}_g(\nu, p) = \frac{1}{\Delta\nu} \int_{-\Delta\nu/2}^{\Delta\nu/2} \prod_{i=1}^{N} \exp\left\{ \int_{p}^{0} k_i(\nu, p', T) \frac{r(p')}{g \cos\theta}\, dp' \right\} d\nu\,, \qquad (3)$$

where T is the temperature, g is the gravitational acceleration, $r(p)$ is the absorbing gas mass mixing ratio, θ is the zenith angle of the radiation, N is the total number of lines contributing to absorption at this wavenumber, and $k_i(\nu, p, T)$ is the monochromatic absorption coefficient of the i^{th} absorption line at wavenumber ν.

The single absorbing gas considered in this study is CO_2. The only other important absorbing gas in the Martian atmosphere is H_2O, but it causes very little extinction at these wavelengths [*Crisp*, 1990]. Since the original analyses of the IRIS spectra were conducted in the mid–1970's, the HITRAN database of atmospheric absorption line parameters has been refined several times. Each revision has incorporated improved spectroscopic constants for calculating line positions and strengths, and has corrected errors and discrepancies discovered in the previous versions. We use the 1986 edition of HITRAN [*Rothman et al.*, 1987].

The temperature and dust optical depth retrieval algorithms require the calculation of atmospheric transmittances in the spectral ranges 450 cm^{-1} to 900 cm^{-1} (covering the entire 15 μm CO_2 band) and 950 cm^{-1} to 1250 cm^{-1} (covering the entire 9 μm silicate band, and two weak CO_2 hot bands). The most versatile and accurate approach to solving equation (3), called a line–by–line model, involves a straightforward numerical integration over the spectrum. However, because the CO_2 15 μm band encompasses nearly 20,000 spectral lines, some of which require intervals less than 10^{-4} cm^{-1} to be resolved [*Crisp et al.*, 1986], the line–by–line model is extremely computationally expensive. It is therefore impractical to use a line–by–line model in this application, where the transmittances must be recomputed several times for each spectrum and the data subset includes almost 2400 spectra.

There are several more efficient approximate methods, employing a variety of simplifying assumptions about the structure of the CO_2 15 μm band, which can be used to calculate atmospheric transmittances. In this study we use a quasi–random

model, which is described in detail by *Crisp* [1990] and the Appendix. The basic premise behind the quasi–random model is that the effects of line overlap can be accounted for by assuming that the line centers are distributed randomly within each narrow spectral interval $\Delta\nu$. For this application, we adopt $\Delta\nu = 0.39$ cm^{-1}. Because the line positions are assumed to be uncorrelated in wavenumber within this interval, the order of the product and the integral over ν in equation (3) can be reversed, yielding:

$$\mathcal{T}_g(\nu,p) = \prod_{i=1}^{N} \frac{1}{\Delta\nu} \int_{-\Delta\nu/2}^{\Delta\nu/2} \exp\left\{ \int_{p}^{0} k_i(\nu,p',T)\, \frac{r(p')}{g\,\cos\theta}\, dp' \right\} d\nu\,. \qquad (4)$$

Thus the transmittance is evaluated separately for each line, and the overlap between lines is accounted for by taking the product of the contributions from the individual lines. Because the quasi–random model divides the band into many small intervals, it accurately represents both the spacing of the spectral lines within a band, and the intensity distribution of the lines. It utilizes a Voigt line shape function, and it accounts for variations in line strength and width along inhomogeneous atmospheric optical paths through the explicit numerical integration of equation (4).

Crisp [1990] compared results from the quasi–random model to those from a line–by–line model and showed that the quasi–random model rarely introduced transmittance or radiance errors larger than one percent outside of the narrow Q–branches of the 15 μm band. Because the quasi–random model is 100 to 1000 times more efficient than line–by–line models (which were used in previous studies), the transmittances can be recomputed often to account for variations in atmospheric temperatures, which produce large variations in the strength of lines in the far wings of the 15 μm band. Accurate estimates of the transmittances at these wavelengths are needed to derive temperatures near the surface of Mars. The transmittances are calculated on a high–resolution (0.39 cm^{-1}) spectral grid and then smoothed to

the resolution of the Mariner 9 data using the IRIS hamming window apodization function of full–width 2.4 cm^{-1} [*Hanel et al.*, 1980].

For a mixture of gas and dust, the atmospheric transmittance is the product of $\mathcal{T}_g(\nu,p)$ and $\mathcal{T}_d(\nu,p)$, the dust transmittance. Assuming Beer's Law (*cf.*, *Liou* 1980, *p.* 21) for absorbing dust, the atmospheric transmittance is defined:

$$\mathcal{T}(\nu,p) \;=\; \mathcal{T}_g(\nu,p)\,\mathcal{T}_d(\nu,p) \;=\; \mathcal{T}_g(\nu,p)\,e^{\frac{-\tau(\nu,p)}{\cos\theta}}\,. \tag{5}$$

$\tau(\nu,p)$, the dust absorption optical depth above any pressure level p, is given by:

$$\tau(\nu,p) \;=\; \int_{z(p)}^{\infty} k(\nu,z')\,dz' \tag{6}$$

where

$$k(\nu,z) \;=\sigma_a(\nu)\,N(z)\,.$$

$k(\nu,z)$ is the dust absorption coefficient, $\sigma_a(\nu)$ is the dust absorption cross section per particle, $N(z)$ is the dust particle number density, and $z(p)$ is the (hydrostatic) altitude at pressure p.

The divergence of the transmittance along the optical path is the weighting function, which indicates the contribution of different atmospheric levels to the upwelling radiance. A weighting function profile is calculated for each apodized channel of the IRIS instrument. Weighting functions for selected channels in the CO_2 15 μm band are shown in Figure 3a for a typical spectrum. In the center of the absorption band, where the gas absorption coefficients are largest, the emitted radiation comes mainly from high altitudes; in the more transparent band wings the emitted radiation comes principally from the surface and near–surface atmospheric layers. Thus, measurement of the thermal emission in different channels across a spectral band yields information about the vertical temperature structure of the atmosphere. The highest IRIS weighting function peaks at $\sim$ 0.03 mbar, or approximately 55 km. Very little

information can be deduced about the thermal structure above that level from this data set. The vertical resolution of the retrieved temperature profiles is limited by the width of the weighting functions, which varies from about 15 km near the surface to about 40 km at the top of the domain. The pressures at which the weighting functions peak are plotted as a function of wavenumber in Figure 3b. For the majority of the channels, the weighting functions peak in the lower atmosphere.

3.3 Retrieval Techniques

3.3.1 General Methodology

If the temperatures and the absorber amounts along the path are known, then equation (1) can be integrated numerically for the intensity at any frequency. This is the forward model. The inverse problem – estimation of the state of the atmosphere from measurements of its thermal emission – is much more complicated. The integrand in equation (1) is a product of the Planck function (which depends strongly on temperature) and the derivative of the transmittance (which depends primarily on the distribution of absorbers). Therefore, if the absorber distribution is known, the observed radiances are functions only of the temperature. Similarly, if the atmospheric temperatures are known, the observed radiances are functions only of the distribution of absorbers. In both cases the quantity to be recovered resides under the integral operator. Various combinations of temperatures and absorber amounts may produce the same radiance signature. The problem is underdetermined, and no mathematically unique solution exists [*Rodgers*, 1976].

In order to retrieve the temperature or absorber amount distributions from the observed radiances, some sort of *a priori* constraints must be imposed. Statistical methods, which linearize the Planck function with respect to a climatological temperature distribution, are not convenient for the remote sounding of the Martian atmosphere, for which climatological data are sparse. Alternatively, solutions to the

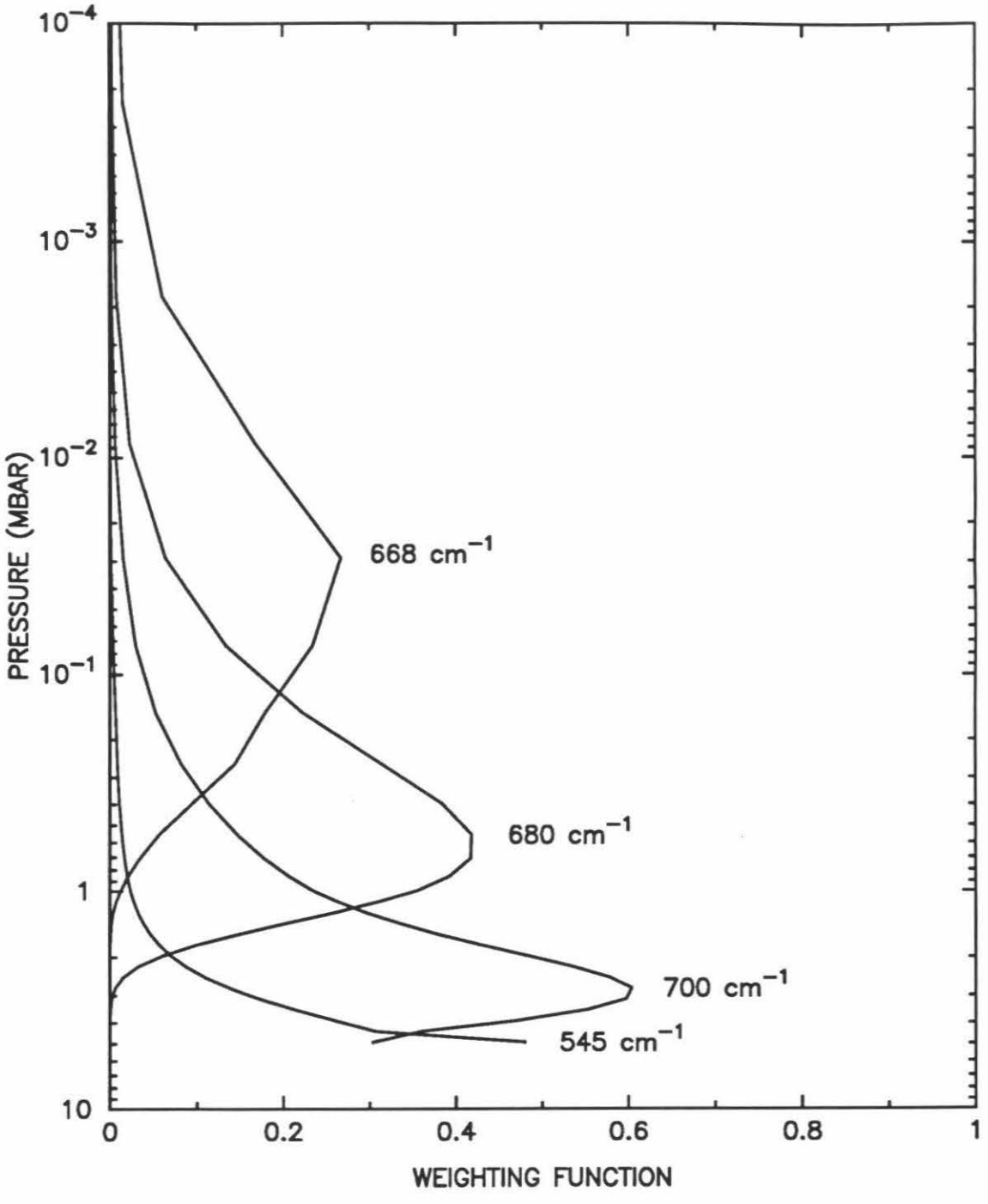

Figure 3a. Weighting functions of selected channels in the 15 μm CO_2 absorption band. The highest weighting function, which occurs in the core of the band, peaks at $\sim$ 0.03 mbar ($\sim$ 55 km). The vertical resolution of the retrieved temperature profiles is limited by the width of the weighting functions, which varies from about 15 km near the surface to about 40 km at the top of the domain.

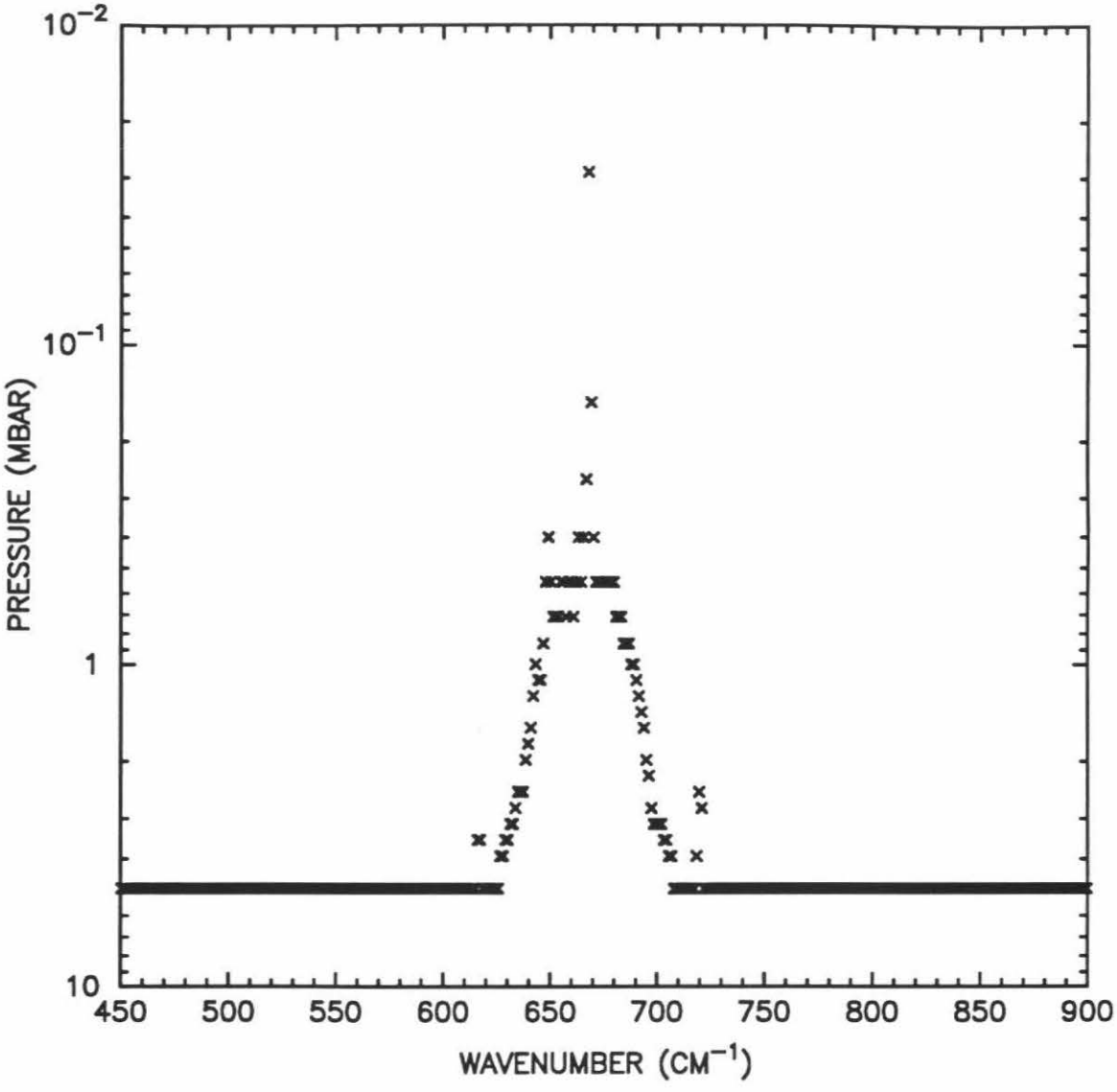

Figure 3b. The pressures at which the weighting functions peak, as a function of wavenumber. For most channels the weighting functions peak in the lower atmosphere.

inverse problem can be found through the use of *ad hoc* assumptions about the radiative transfer equation. Although these methods still employ *a priori* constraints, they exploit the physics of the problem rather than relying on previously–obtained climatological information. Two of the most widely used of these are the *Chahine* [1968, 1970, 1972] and *Smith* [1970] methods. Both of these techniques were implemented to retrieve atmospheric temperature profiles from the IRIS thermal emission spectra, but Chahine's method was found to be extremely sensitive to data noise and produced large oscillations in the derived temperature profiles. Therefore, the procedures we use to obtain the atmospheric temperatures and dust amounts are based on Smith's method.

Vertical distributions of both atmospheric temperature and dust optical depth are retrieved simultaneously through an iterative procedure which is performed on each spectrum. Initially, atmospheric temperatures are obtained from radiances in the 15 μm CO_2 absorption band assuming a small amount of airborne dust. These temperatures are used to derive dust optical depths from radiances in the 9 μm region. The atmospheric transmittances are then recomputed from the revised temperature and dust profiles, and the entire procedure is repeated until it converges to yield consistent vertical temperature and dust optical depth profiles.

3.3.2 Temperature Retrieval

Smith [1970] developed a numerical iteration method to estimate the atmospheric temperature profile, starting from an initial guess. The principal assumption is that, for each sounding frequency, the difference in the Planck function from one iteration to the next is constant throughout the atmospheric column. Applying this assumption to the radiative transfer equation (equation (1)) leads to a relation between the Planck functions at two successive iterations:

$$B^{n+1}(\nu_i, T(p)) = B^n(\nu_i, T(p)) + \left[\tilde{I}(\nu_i) - I^n(\nu_i)\right] \qquad (7)$$

where ν_i is the wavenumber of the i^{th} observation channel, $\tilde{I}(\nu_i)$ is the measured radiance, $I^n(\nu_i)$ is the computed radiance at the n^{th} iteration, and $I^{n+1}(\nu_i)$ is set to $\tilde{I}(\nu_i)$. The principal assumption of the Smith method is applied to the radiative transfer equation only to generate the $(n+1)^{st}$ guess for $T(p)$; it is not used in the integration of the computed radiance, I^n. A relationship for updating the temperature profile between iterations is obtained by inverting equation (2):

$$T^{n+1}(\nu_i, p) = \frac{(hc/k)\,\nu_i}{\ln\left\{\frac{2hc^2\nu_i^3}{B^{n+1}(\nu_i,p)} + 1\right\}}. \tag{8}$$

Equation (8) gives an independent estimate of the temperature at each atmospheric pressure level for each spectral channel. The best approximation of the true temperature at each pressure level is found through a weighted average of these independent estimates, with weights for the average taken to be the weighting functions:

$$T^{n+1}(p) = \frac{\sum_{i=1}^{M} T^{n+1}(\nu_i, p)\frac{\partial \mathcal{T}(\nu_i,p)}{\partial(\ln p)}}{\sum_{i=1}^{M} \frac{\partial \mathcal{T}(\nu_i,p)}{\partial(\ln p)}} \tag{9}$$

where M is the number of channels. At the wavenumber spacing of the IRIS spectra, there are about 380 channels in the interval 450–900 cm^{-1}. Smith's weighted–average scheme is advantageous for inverting real radiance data because it suppresses random errors introduced by instrument noise. However, it may also smooth out real oscillations with vertical scales that are small compared to the width of the weighting functions.

The temperatures of the surface and of the atmosphere just above the surface are not explicitly constrained by Smith's method. We calculate the temperature of the surface, T_s, from equation (1) using the observed radiances in channels from the "window" regions, where the surface provides the major contribution to the radiances. The presence of airborne dust complicates the definition of the "window" regions. Because dust is not completely transparent at any wavenumber, no point in the

spectrum will allow a perfect measure of the surface temperature. To account for the effects of dust opacity, we define the "window" channels to be those spectral intervals for which the total transmittance (see equation (5)) from the surface to space has a value among the largest ten percent of the values from all channels, or exceeds 0.99 (a value this high is only achieved under the clearest conditions). For a typical spectrum in this data subset, there are about 5 channels in the far wing of the short–wavenumber side of the band (450–455 cm^{-1}) and about 35 channels in the wing of the long–wavenumber side of the band (820–865 cm^{-1}) which satisfy these criteria. An independent estimate of the surface temperature is derived from each window channel. These values are then averaged to give a best estimate of T_s.

Our implementation of the Smith algorithm produces temperature estimates at the midpoint of each model atmosphere layer. The boundaries of these layers correspond to the pressure levels in the model atmosphere; that is, J pressure levels define $(J-1)$ atmospheric layers. Linear interpolation is used to estimate the temperatures at the layer boundaries from the midpoint values, leaving the temperature at the base of the atmosphere, $T(p_s)$, undetermined. For J atmospheric pressure levels, $T(p_s) = T(J)$ is obtained by extrapolating the layer midpoint temperature down along the adiabat. Labelling the extrapolated temperature as T^*, the atmospheric temperature at the surface is then found according to the following scheme:

$$T(p_s) \;=\; T(J) \;=\; \begin{cases} T^* & \text{if} \quad T_s > T^* \\ T_s & \text{if} \quad T(J-1) < T_s < T^* \\ \frac{1}{2}\left(T_s + T(J-1)\right) & \text{if} \quad T_s < T(J-1)\ . \end{cases} \tag{10}$$

Several additional modifications to the Smith procedure are necessary to produce atmospheric temperatures at the top of the domain. First, radiances in all channels defined to be in the window regions are excluded from the atmospheric temperature calculation, thus decoupling the estimation of the atmospheric temperature profile from the surface temperature. This reduces the value of M in equation (9) to about 340 channels for a typical spectrum. Second, in applying equation (9), tem-

perature estimates from atmospheric layers in which the magnitudes of the weighting functions are less than five percent of maximum are ignored. This step prevents contributions from a large number of weighting functions peaked at or near the surface from dominating the temperature estimate at high altitudes where very few weighting functions are peaked (*cf.* Figure 3b). Third, the atmospheric temperatures at pressures lower than that of the peak of the topmost weighting function, p_{peak} (typically about 0.03 mbar, or 55 km), are relaxed to an isothermal profile at temperature $T(p_{peak})$ through the following relationship:

$$T(p) = T(p_{peak}) + \sqrt{\alpha(p)}\left[T_{est}(p) - T(p_{peak})\right] \tag{11}$$

where T_{est} is the temperature value estimated by the retrieval algorithm, and $\alpha(p)$ is given by:

$$\alpha(p) = \begin{cases} 1.0 & \text{at} \quad p \geq p_{peak} \\ W_{peak}(p) & \text{at} \quad p < p_{peak} \end{cases}, \tag{12}$$

where W_{peak} is the topmost weighting function. The square root of the weighting function value was chosen through trial and error to slow the rate at which the temperature profile approaches $T(p_{peak})$. This constraint prevents the algorithm from producing spurious large–amplitude temperature oscillations at altitudes above the domain sampled by IRIS. Fourth, the retrieved atmospheric temperature is prohibited from falling below the CO_2 frost point at any level.

3.3.3 Dust Optical Depth Retrieval

Because scattering processes are ignored in this study, only the dust absorption optical depth is calculated. The dust absorption optical depth at any wavenumber ν_i can be obtained from its value at the reference wavenumber, ν_0, through the relation:

$$\tau(\nu_i, p) = \frac{Q_{abs}(\nu_i)}{Q_{abs}(\nu_0)}\tau(\nu_0, p) = q(\nu_i)\tau(p) \tag{13}$$

where Q_{abs} is the absorption efficiency factor derived from a Mie–scattering calculation. We have taken the reference wavenumber to be 1100 cm^{-1} (9 μm), so that $\tau(p)$

is the optical depth at 9 μm. In this way the dust optical depth can be written in terms of separate p–dependent and ν–dependent components.

Smith [1970] describes an iterative algorithm for obtaining the mixing ratio profile of an absorbing gas. We modified Smith's method to solve for the dust amount in each atmospheric layer. Integrating the radiative transfer equation by parts casts equation (1) into the form:

$$I(\nu) = \epsilon\, B[\nu, T_s]\, \mathcal{T}(\nu, p_s) - B[\nu, T(p_s)]\, \mathcal{T}(\nu, p_s) + B[\nu, T(p_t)]\, \mathcal{T}(\nu, p_t) - \int_{\ln p_s}^{\ln p_t} \mathcal{T}(\nu, p)\, \frac{\partial B[\nu, T(p)]}{\partial(\ln p)}\, d(\ln p)\,. \qquad (14)$$

Note that T_s is the surface temperature, whereas $T(p_s)$ is the temperature of the atmospheric layer just above the surface. The iterative equations for dust optical depth are derived by defining $I^n(\nu_i)$ and $I^{n+1}(\nu_i)$ as the radiances computed from equation (14) for two successive iterations with dust optical depths $\tau^n(p)$ and $\tau^{n+1}(p)$, respectively. The equations for $I^{n+1}(\nu_i)$ and $I^n(\nu_i)$ are then differenced, and $I^{n+1}(\nu_i)$ is set equal to the observed radiance, $\tilde{I}(\nu_i)$. Using equation (5) for the transmittance of an atmosphere with both gas and dust absorption, and defining the derivative of the dust transmittance with respect to the dust optical depth, yields:

$$\begin{aligned}\tilde{I}(\nu_i) - I^n(\nu_i) = &-\frac{1}{\cos\theta}\, \mathcal{T}(\nu_i, p_s) \left[\epsilon\, B[\nu_i, T_s] - B[\nu_i, T(p_s)]\right] q(\nu_i) \left[\tau^{n+1}(p_s) - \tau^n(p_s)\right] \\ &- \frac{1}{\cos\theta}\, \mathcal{T}(\nu_i, p_t)\, B[\nu_i, T(p_t)]\, q(\nu_i) \left[\tau^{n+1}(p_t) - \tau^n(p_t)\right] \\ &+ \int_{\ln p_s}^{\ln p_t} \frac{1}{\cos\theta}\, \mathcal{T}(\nu_i, p)\, q(\nu_i) \left[\tau^{n+1}(p) - \tau^n(p)\right] \frac{\partial B[\nu_i, T(p)]}{\partial(\ln p)}\, d(\ln p)\,. \qquad (15)\end{aligned}$$

An approximation must now be introduced to solve this equation for $\tau^{n+1}(p)$. Following *Smith* [1970], we assume that the ratio $[\tau^{n+1}(p) - \tau^n(p)]/\tau^n(p)$ remains constant

throughout the atmospheric column. Multiplying and dividing by the factor $\tau^n(p)$ allows us to solve for this quantity:

$$\frac{\tau^{n+1}(p) - \tau^n(p)}{\tau^n(p)} = C^{n+1}(\nu_i) = \frac{\tilde{I}(\nu_i) - I^n(\nu_i)}{S_0 + T_0 - A_0} \tag{16}$$

where

$$S_0 = -\frac{1}{\cos\theta}\,\mathcal{T}(\nu_i, p_s)\,q(\nu_i)\,\tau^n(p_s)\left[\epsilon\,B[\nu_i, T_s] - B[\nu_i, T(p_s)]\right],$$

$$T_0 = -\frac{1}{\cos\theta}\,\mathcal{T}(\nu_i, p_t)\,q(\nu_i)\,\tau^n(p_t)\,B[\nu_i, T(p_t)],$$

$$A_0 = -\int_{\ln p_s}^{\ln p_t} \frac{1}{\cos\theta}\,\mathcal{T}(\nu_i, p)\,q(\nu_i)\,\tau^n(p)\,\frac{\partial B[\nu_i, T(p)]}{\partial(\ln p)}\,d(\ln p).$$

Equation (16) gives an independent estimate of the ratio $C^{n+1}(\nu_i)$ for each observation ν_i. To find the actual value these estimates must first be converted to the reference wavenumber by dividing by the parameter q. Then the best approximation is found through a weighted average of these independent estimates (*cf.* equation (9)), where the weights are given by:

$$W^{n+1}(\nu_i, p) = -\frac{1}{\cos\theta}\,\mathcal{T}(\nu_i, p)\,\tau^n(p)\,\frac{\partial B[\nu_i, T(p)]}{\partial(\ln p)}. \tag{17}$$

In this case, there are 250 channels in the interval 950–1250 cm^{-1}. Once the best estimate for the ratio in equation (16) has been obtained, the $\tau^{n+1}(p)$ values can be calculated.

To prevent divergence, which can occur if the initial guess for the dust distribution is poor, the size of the steps taken between iterations must be reduced. This is accomplished through the use of a relaxation parameter, R:

$$\tau^{n+1}(p) = \tau^n(p) + R\left[\tau_{est}(p) - \tau^n(p)\right] \tag{18}$$

where $\tau_{est}(p)$ is the dust optical depth value estimated by the retrieval algorithm at iteration $n+1$. The value of R is initially set to 0.1, but if the optical depths start to diverge the value of R is halved and the iteration is repeated.

One inherent limitation of any thermal infrared constituent retrieval technique is that there must be sufficient thermal contrast between the atmosphere and the surface. In an atmosphere that is nearly isothermal, the airborne dust emits as much radiation as it absorbs from the surface, and consequently it cannot be distinguished spectrally from the surface. Therefore, the dust retrieval is bypassed for any spectrum with a small surface/atmosphere temperature difference (see Section 5.3).

3.3.4 Iteration of Retrieval Procedure

The iterative retrieval scheme includes both major and minor iterations. A single major iteration consists of four steps: (1) calculation of atmospheric transmittances in the 15 μm region using current estimates of the temperature and dust optical depth profiles, (2) retrieval of revised temperature profiles from radiances in the 15 μm region, using the algorithm described in equations (7)–(12), with gas and dust transmittances held constant, (3) calculation of atmospheric transmittances in the 9 μm region, and (4) retrieval of revised dust optical depths from radiances in the 9 μm region, using the algorithm described in equations (13)–(18), with temperatures and gas transmittances held constant. The temperature and dust optical depth retrieval algorithms are themselves iterative procedures, and the repetitions of these algorithms during a single major iteration are referred to as minor iterations.

The maximum number of minor iterations in the temperature retrieval algorithm is set to twenty, although the iterations are usually discontinued before that cut–off for one of the following reasons: (1) the difference, $T^{n+1}(p) - T^{n}(p)$, between temperatures on successive minor iterations exceeds 30 K, in which case a new major iteration is performed to recompute the atmospheric transmittances, (2) the change in computed brightness temperature from one minor iteration to the next falls below 0.1 K in every channel, in which case convergence is proceeding too slowly for further iterations to be of value, or (3) the difference between the observed and computed

brightness temperature in every channel is less than 1.0 K, in which case we consider convergence to have been achieved.

A different convergence criterion is defined for the dust retrieval. After every minor iteration of the dust retrieval algorithm, the dust transmittances are recalculated from the new dust optical depths using equation (5), and the radiative transfer equation is integrated to produce computed radiances. The residuals between the observed and computed radiances are evaluated to determine if convergence has been achieved. Typically, the residuals continue to decrease between minor iterations, but they do so at such a slow rate that the minor iterations must be terminated even though the convergence criterion has not been met.

Once the updated profiles of temperature and dust optical depth have been derived, the atmospheric transmittances in the 15 μm region are recalculated and another major iteration is performed. The maximum number of major iterations is set to eight for each spectrum. After each major iteration, the newly–derived temperature profile is compared to the previous one. If the difference between the two temperature profiles is less than 0.5 K at every level, then further recalculation of the transmittances is unnecessary and the process is stopped before the maximum number of major iterations is reached. An overall radiance residual is defined from the temperature and dust retrieval radiance residuals, and the results from the major iteration which produces the smallest overall residual are retained as the final values. This step is taken because the simultaneous retrieval of atmospheric temperature and dust optical depth is not always an absolutely convergent process.

In general, the retrieval process converges and produces a good fit to the observed spectra. For warm daytime spectra, the retrievals are usually terminated because convergence is proceeding too slowly. In these cases, further convergence is hindered by limitations in the radiative transfer model, the retrieval methods, or

the assumed dust or surface optical properties. For cold nighttime or polar spectra, the retrievals are often terminated when the radiance residuals approach the noise equivalent radiance of the measurements. A few spectra ($\sim$ 10) with very poor convergence were rejected from this analysis.

3.4 Creation of Data Maps

As demonstrated in Figure 1, the spatial and temporal coverage of the IRIS data set is not uniform. To display contour maps of the results obtained from all 2400 spectra, it was necessary to interpolate the irregularly–spaced data points onto an equispaced grid. *Eckstein* [1989] tested polynomial and weighted average interpolation algorithms on geophysical data sets and found that weighted averages of the input data produced the most reliable interpolated values. We generated cross–sections of temperature in various combinations of pressure, latitude, time of day, or Martian solar day on a Cartesian output grid by taking a weighted average of all nearby points. Our algorithm utilized Gaussian weighting, with the interpolated values, $f(x,y,z)$, calculated from the unevenly–distributed values, $f(x_i,y_j,z_k)$, according to:

$$f(x,y,z) = \frac{\sum_{k=1}^{H}\sum_{j=1}^{N}\sum_{i=1}^{M} w_{ijk}\, f(x_i,y_j,z_k)}{\sum_{k=1}^{H}\sum_{j=1}^{N}\sum_{i=1}^{M} w_{ijk}} \tag{19}$$

where

$$w_{ijk} = \begin{cases} \exp(-\ln 2 * r_{ijk}) & \text{if} \quad r_{ijk} < R_{max} \\ 0.0 & \text{if} \quad r_{ijk} \geq R_{max} \end{cases}$$

and

$$r_{ijk} = \frac{(x - x_i)^2}{R_x^2} + \frac{(y - y_j)^2}{R_y^2} + \frac{(z - z_k)^2}{R_z^2}.$$

M, N, and H designate the dimensions of the data set in the x, y, and z directions. The values of R, the half–width at half–maximum of the weights, were taken to be 10° in latitude, 1 hour in Mars local time of day, 0.25 in Martian solar day, and 0.3

in the natural logarithm of the pressure. The parameter R_{max} was typically set to 5, so that all data points within five halfwidths of a given grid location contributed to the value there. The final data products do not explicitly account for any longitude–dependent variations in temperature which may exist. This interpolation technique causes some data smoothing, and it will create results in regions which are poorly constrained by existing data. To avoid presenting fictitious results, we retain only those results produced near existing data. Contours in the data maps are interrupted in places where data are sparse or absent.

4. Model Parameters and Initial Conditions

The solution to equation (1) depends on the values of several atmospheric and surface parameters. Calculation of the upwelling radiances on the first iteration requires initial guesses for the surface temperature, the atmospheric temperature distribution, and the dust optical depth profile, all of which are updated during the retrieval. Other required parameters, such as surface emissivity, wavelength–dependent dust optical properties, and absorbing gas concentration, are estimated from *a priori* information and remain constant.

4.1 Surface Properties

For each spectrum, a first guess for the surface temperature, T_s, is made by averaging brightness temperature values from radiances in a spectral interval extending from 320 cm^{-1} to 370 cm^{-1}, where the atmosphere absorbs and emits very little radiation. The value of the local surface pressure must be known in order to integrate the radiative transfer equation. To estimate the surface pressure, p_s, we assume that the layer of the atmosphere between the altitude of the geoid, z_{geoid}, and the actual surface, z_s, is isothermal at temperature T_s. Defining the variable z_{topo} to represent the surface elevation relative to the geoid, $z_{\text{topo}} = z_s - z_{\text{geoid}}$, we integrate

the hydrostatic equation to solve for p_s:

$$p_s = p_{\text{geoid}} \exp\left\{-\frac{g\, z_{\text{topo}}}{R T_s}\right\} \tag{20}$$

where R is the mean gas constant. The surface elevation relative to a geoid at $p_{\text{geoid}} =$ 6.1 mbar is obtained for the latitude and longitude of each spectrum from topography data in the Atmospheres Node of the Planetary Data System (PDS) archive (based on photogrammetry of Viking Orbiter images and earth–based radar altimetry [*Wu*, 1979]). Because the PDS topography file contains data only for latitudes between 56° S and 56° N, a surface pressure equal to the geoid value is assumed for all spectra taken at higher latitudes. Tests on sample spectra indicated that the retrieved lower–atmosphere temperatures and total dust amounts are very sensitive to the value of the surface pressure. Using a value of the surface pressure which was too high resulted in a corresponding overestimation of the total dust optical depth, but generally produced much better fits than did using a value that was too low.

Results from the Viking IRTM experiment indicated that the surface emissivity is near unity [*Kieffer*, 1976]. No attempt was made to include the wavelength–dependence of the surface emissivity for this study. We adopted $\epsilon = 0.95$ as a reasonable value for basalt and its weathering products (after *Crisp* [1990]), and preliminary inversions confirmed that this value yielded the lowest overall residuals for most of the spectra in the data subset. Experiments in which different values of the surface emissivity were specified indicated that the retrieved surface and lower–atmosphere temperatures are most sensitive to this parameter.

4.2 Model Atmosphere

Quantities are defined at discrete pressure levels in order to numerically integrate equations (1) and (4). The number of levels was chosen empirically to balance the error introduced in trapezoid rule integration (which decreases with increasing

vertical resolution) against the sensitivity of the retrieved profiles to random noise (which increases with increasing vertical resolution) [*Conrath*, 1972]. A further consideration is that the computational expense of the atmospheric transmittance calculation is directly related to the number of levels in the model. We use a 30–level model atmosphere with 15 of these levels equally spaced in the logarithm of pressure between the lowest atmospheric level and the 1 mbar level. The lowest level of the model atmosphere is positioned a few meters above the surface by specifying its pressure to be 99.5% of the surface pressure. This high resolution pressure grid in the lower atmosphere accommodates the distribution of the weighting functions in the 15 μm band (*cf.* Figure 3b). The remaining 15 levels of the model atmosphere are distributed between 1 mbar and 10^{-8} mbar such that the spacing between successive levels increases by a constant factor.

An initial atmospheric temperature profile is defined from the initial estimate of the surface temperature (see Section 4.1) and a single high–altitude temperature, which is found by averaging brightness temperature values in a spectral interval extending from 650 cm^{-1} to 680 cm^{-1} (encompassing the peak of the CO_2 15 μm band). We construct an initial guess for the temperature profile by assigning this representative atmospheric temperature to the 0.5 mbar pressure level and interpolating the temperature linearly with $\ln p$ between this level and the surface. Above this level the initial temperature profile is assumed to be isothermal. The retrieved temperature profile is sensitive to the initial guess only if the difference between them is large. The mixing ratio of CO_2, the only absorbing gas considered in this study, is assumed to be 0.953 at all levels [*Owen*, 1982], and terrestrial isotopic abundances are assumed.

4.3 Initial Dust Distribution

The initial vertical variation of the dust absorption coefficient (per unit pres-

sure) is described by:

$$k(p) = k_s \exp\left\{\psi\left[1 - \frac{p_s}{p}\right]\right\} \tag{21}$$

where the parameter ψ fixes the level above which the number density of the dust declines rapidly. This expression was derived by *Conrath* [1975] based on Mariner 9 IRIS observations taken during the dissipation of the global dust storm. Small values of ψ, characteristic of dust storm conditions, produce distributions with dust extending to high altitudes. We used a value of $\psi = 0.01$ after *Conrath* [1975], for which the dust is uniformly mixed up to a height of $\sim$ 35 km. Above this level the mixing ratio falls off rapidly, with the effective top of the dust layer at $\sim$ 50 km. The parameter k_s in equation (21) is the value of k at $p = p_s$. k_s can be calculated from the column–integrated dust optical depth (*cf.* equation (6)):

$$\tau_{\rm col} = \int_0^{p_s} k_s \exp\left\{\psi\left[1 - \frac{p_s}{p}\right]\right\} dp\,. \tag{22}$$

This integral can be solved for k_s:

$$k_s = \frac{\tau_{\rm col}}{p_s\left[1 - \psi\, E_1(\psi)\, \exp(\psi)\right]} \tag{23}$$

where E_1 is the first exponential integral. An initial value for the column–integrated 9 μm dust optical depth of 0.3 is used for all spectra. This value of initial dust optical depth was chosen on the basis of typical conditions reported in *Martin and Kieffer* [1979] and *Martin* [1986]; in addition, our preliminary inversions of the Mariner 9 spectra identified 0.3 as the median $\tau_{\rm col}$ value. Both the retrieved temperature profile and the dust amounts are relatively insensitive to the initial $\tau_{\rm col}$ value, as long as it does not depart appreciably from the actual value.

4.4 Dust Optical Properties

In order to include the effects of dust absorption in calculating the atmospheric transmittances, the wavelength–dependent optical properties of the dust must

be known. *Toon et al.* [1977] extracted information about the particle size distribution and composition of the airborne dust from the Mariner 9 IRIS data. *Toon et al.* averaged together several spectra acquired from similar view angles on the same spacecraft orbit to obtain seven mean spectra with improved signal–to–noise ratios. They attempted to reproduce these mean spectra using different particle size distributions in combination with the optical properties of different materials. The majority of these mean spectra represented early parts of the mission during the dust storm, but the temperature profiles used to calculate their theoretical brightness temperatures were derived without taking dust absorption into account. *Toon et al.* found that the best match to the mean spectra was achieved with dust particles that fit a modified gamma distribution with a mode radius of 0.4 μm and that had the optical properties of a mixture of montmorillonite (a crystalline smectite clay) and basalt. These parameters became the standard model for Mars atmospheric dust.

We initially adopted the dust optical properties given by *Toon et al.* [1977] for our retrievals. However, we found that the dust optical depths needed to produce good fits to the observed radiances in the 9 μm region resulted in far too much absorption in the 20 μm region. This suggested that the dust optical properties may have changed between the very dusty periods studied by *Toon et al.* and the much clearer period represented by our data subset. Therefore, we performed a series of experiments to derive a set of dust optical properties that yields adequate fits at both 9 μm and 20 μm. In these experiments, we replaced montmorillonite with palagonite because comparisons of earth–based telescopic spectra of bright regions on Mars with laboratory reflectance spectra of several terrestrial samples revealed that, at visible and near–infrared wavelengths, the closest spectral analogs known for Martian dust are palagonites — amorphous weathering products of basaltic glass [*Evans and Adams*, 1979; *Singer*, 1982]. We obtained the real and imaginary refractive indices

of a palagonite sample over the range 5 μm to 25 μm [*Roush*, 1991]. These values were used in a Mie–scattering program [*Wiscombe*, 1980] to compute the absorption efficiency factors for the dust particles. A log–normal size distribution [*Hansen and Travis*, 1974] was used, and various values for the mode radius and variance, or width, of the distribution were tested. Improved fits to the observed IRIS spectra were obtained for a mode radius of 0.5 μm and a variance of 0.15. In Figure 4 these brightness temperatures are compared to observed values and those calculated from the *Toon et al.* parameters. Neither set of dust properties reproduces the observed spectrum exactly, but the palagonite dust parameters produce a better match throughout both the 9 μm (Figure 4a) and the 15 μm (Figure 4b) regions. In particular, the fit near 20 μm (500 cm^{-1}) is improved significantly.

The dramatic differences in computed brightness temperatures obtained from the two sets of dust properties may be due in part to the fact that palagonite is a better spectral analog material for Mars dust than is montmorillonite. However, the computed brightness temperatures are strongly influenced by the number of large particles included in the size distribution. Because the spectra in our data subset represent much clearer conditions than those analyzed by *Toon et al.*, we obtain better fits to the observations using a size distribution which encompasses fewer large particles. This particular size distribution provides better fits at both 9 μm and 20 μm, but it is not unique, and it may not be adequate for estimating the optical depths at visible wavelengths which correspond to these 9 μm values. The visible opacity cannot be obtained directly from the IRIS observations because they are not sensitive to the distribution of small particles, which dominate the visible optical depths.

5. Results and Discussion

The principal products of this investigation are global maps of temperature

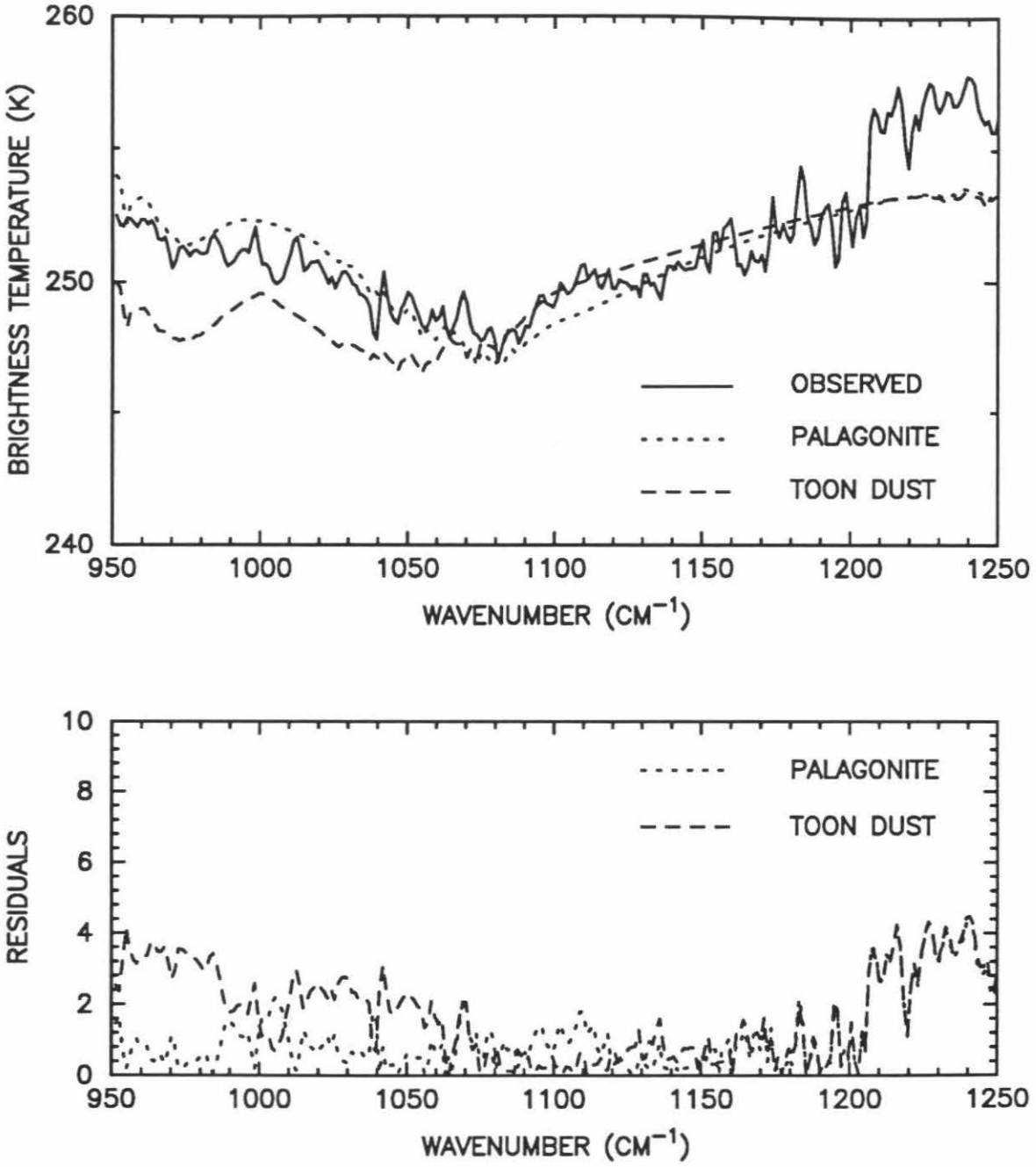

Figure 4a. Comparison of observed brightness temperatures (solid line) and computed brightness temperatures based on the standard *Toon et al.* [1977] (dashed line) and new palagonite (dotted line) dust optical properties, for the 9 μm region. In the *Toon et al.* model the dust particles fit a modified gamma distribution with a mode radius of 0.4 μm and have the optical properties of a mixture of montmorillonite and basalt. Our model employs a log–normal size distribution with a mode radius of 0.5 μm.

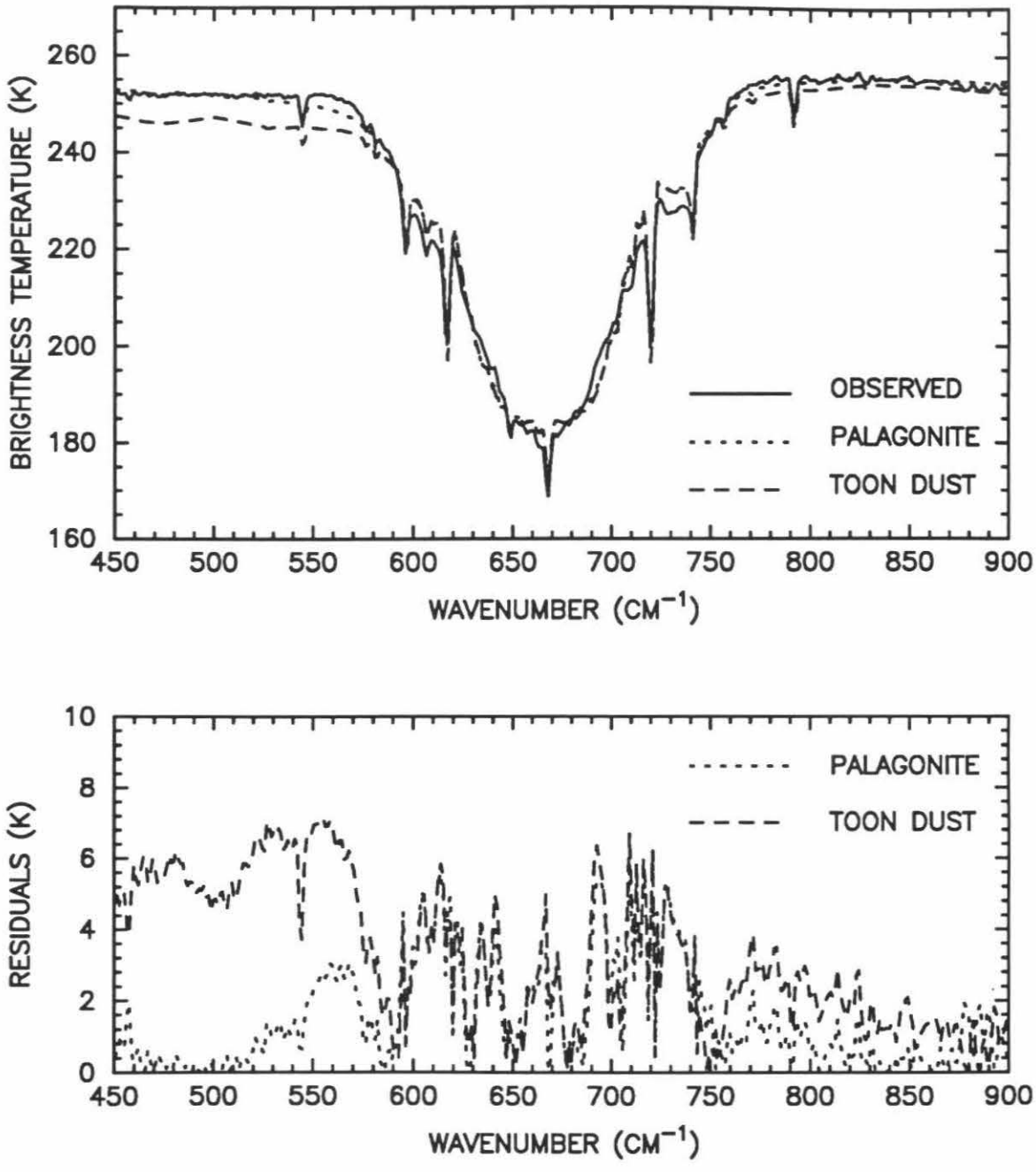

Figure 4b. Same as Figure 4a, for the 15 μm region.

and dust optical depth as functions of latitude ($\pm 90°$), altitude ($\sim$ 0 – 60 km), and Mars local time. In addition, we present temperature and dust retrievals from individual IRIS spectra to validate the retrieval methods, illustrate the impact of dust absorption on the temperature retrieval process, and examine the variation of the retrieved temperatures with geographic location, local time of day, and atmospheric dust abundance. Results from individual spectra are discussed first, followed by the spatial and temporal maps constructed from the entire data subset.

The vertical coordinate in most of the subsequent figures is the atmospheric pressure, p. The altitude corresponding to a given pressure level can be approximated through the definition of the log–pressure altitude, z:

$$z = -H \ln(p/p_s) \tag{24}$$

where H is the atmospheric scale height. z is plotted as a function of p in Figure 5. This correlation of altitude with pressure is based on the following values: p_s = 6.0 mbar, R = 191.0 J/K/kg, and T = 196 K (the globally– and diurnally–averaged value of the atmospheric temperature at the surface), resulting in a mean scale height H = 10 km.

5.1 Effects of Dust Absorption on Temperature Profiles

Previous efforts to retrieve temperature profiles from the IRIS data set neglected the additional opacity due to airborne dust. Our sensitivity tests indicate that the presence of dust absorption in the retrieval algorithm can cause the derived temperatures to change by more than 20 K in some atmospheric layers, for some spectra. Temperature profiles retrieved with and without dust absorption are shown in Figure 6 for two test spectra with similar dust abundances ($\tau \sim 0.2$). For both test spectra, the dust–free case is characterized by a large temperature difference between the surface and the atmospheric layer adjacent to the surface. This temperature difference is reduced for both spectra when dust absorption is included in the retrieval.

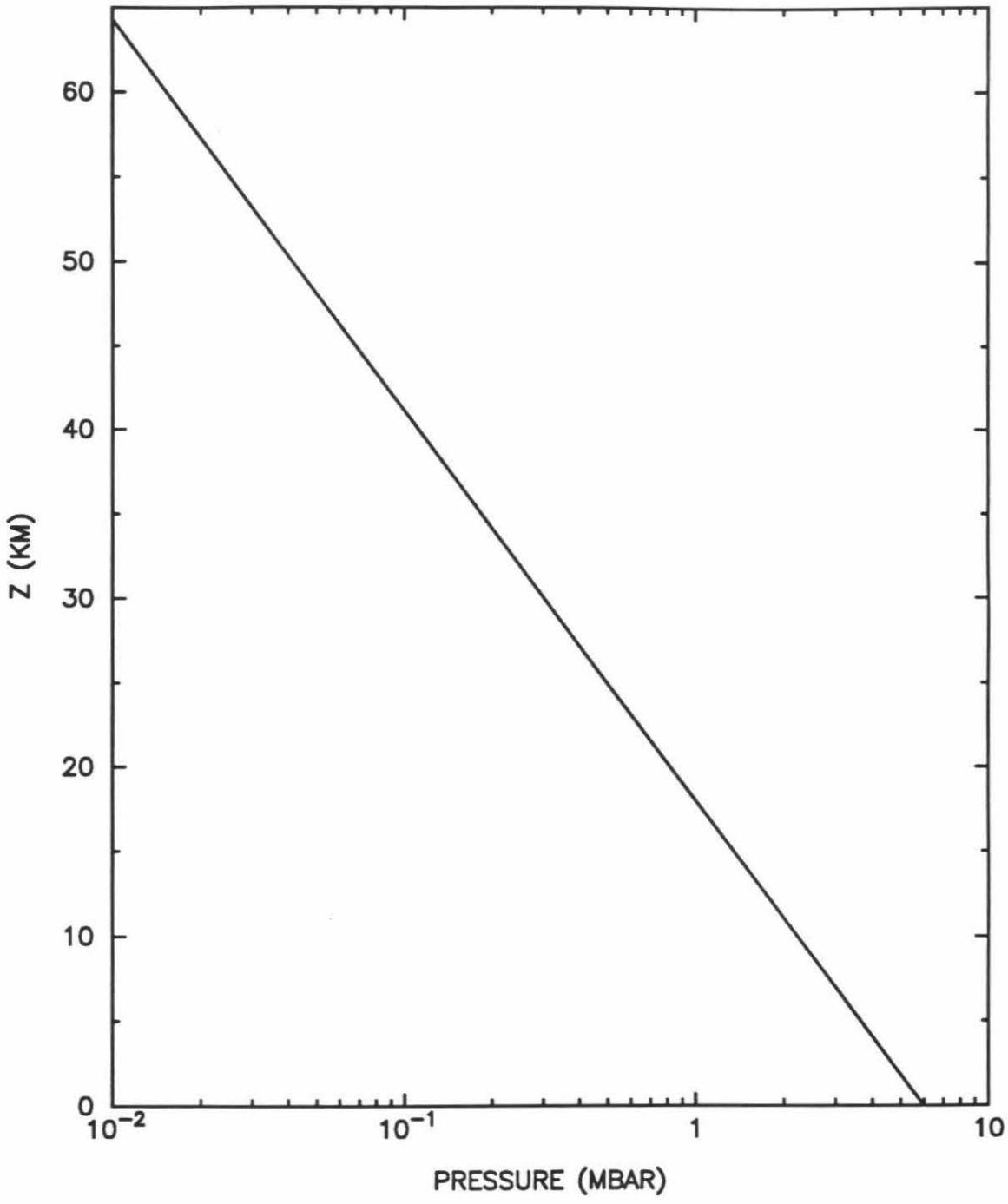

Figure 5. Log–pressure altitude as a function of pressure. Approximate altitudes corresponding to the pressure coordinates of subsequent figures can be found from this plot.

The attenuation of radiation from the near–surface layers by dust absorption forces the retrieved temperatures in these layers to be higher in order to match the observed radiances. The two test spectra exhibit different responses to the presence of dust absorption in the retrieval algorithm, however. For the spectrum shown in Figure 6b, the combined temperature/dust retrieval produces a profile that is substantially cooler at the 1–2 mbar (10–20 km) level. This feature, which is not evident in Figure 6a, may represent real variations in temperature along the atmospheric column. Oscillations of similar magnitudes were observed in both the Viking Lander entry profiles [*Sieff and Kirk*, 1977] and the radio occultation results [*Lindal et al.*, 1979].

5.2 Effects of Location, Local Time, and Dust Abundance

Retrieved temperature profiles from the four sample spectra featured in Figure 2 are shown in Figure 7. The tropical, mid–day spectrum exhibits the high surface temperature, large surface–atmosphere temperature difference, and marginally–stable temperature lapse rate characteristic of profiles acquired near the sub–solar point during the southern summer. Although the width of the weighting functions prohibits the planetary boundary layer from actually being resolved, the large temperature change between the surface and the near–surface atmospheric layer seen in this profile is not unexpected for mid–afternoon conditions. The meteorology instruments on the Viking Landers [*Hess et al.*, 1976] recorded daytime gas temperatures at 1.6 m as much as 25 K colder than the ground temperatures inferred from the IRTM data.

The relatively clear tropical, mid–day spectrum was recorded near Arsia Mons, in a region characterized by high visible albedos and high surface elevations (> 6 km above the geoid). The dusty spectrum was taken at a similar latitude and time of day near Sinus Meridiani, in a region which has lower albedo and lower elevation (~ 1.5 km). Tropospheric temperatures ($p > 1 - 2$ mbar) retrieved from the dusty spectrum appear to be substantially cooler than those obtained from the clear spec-

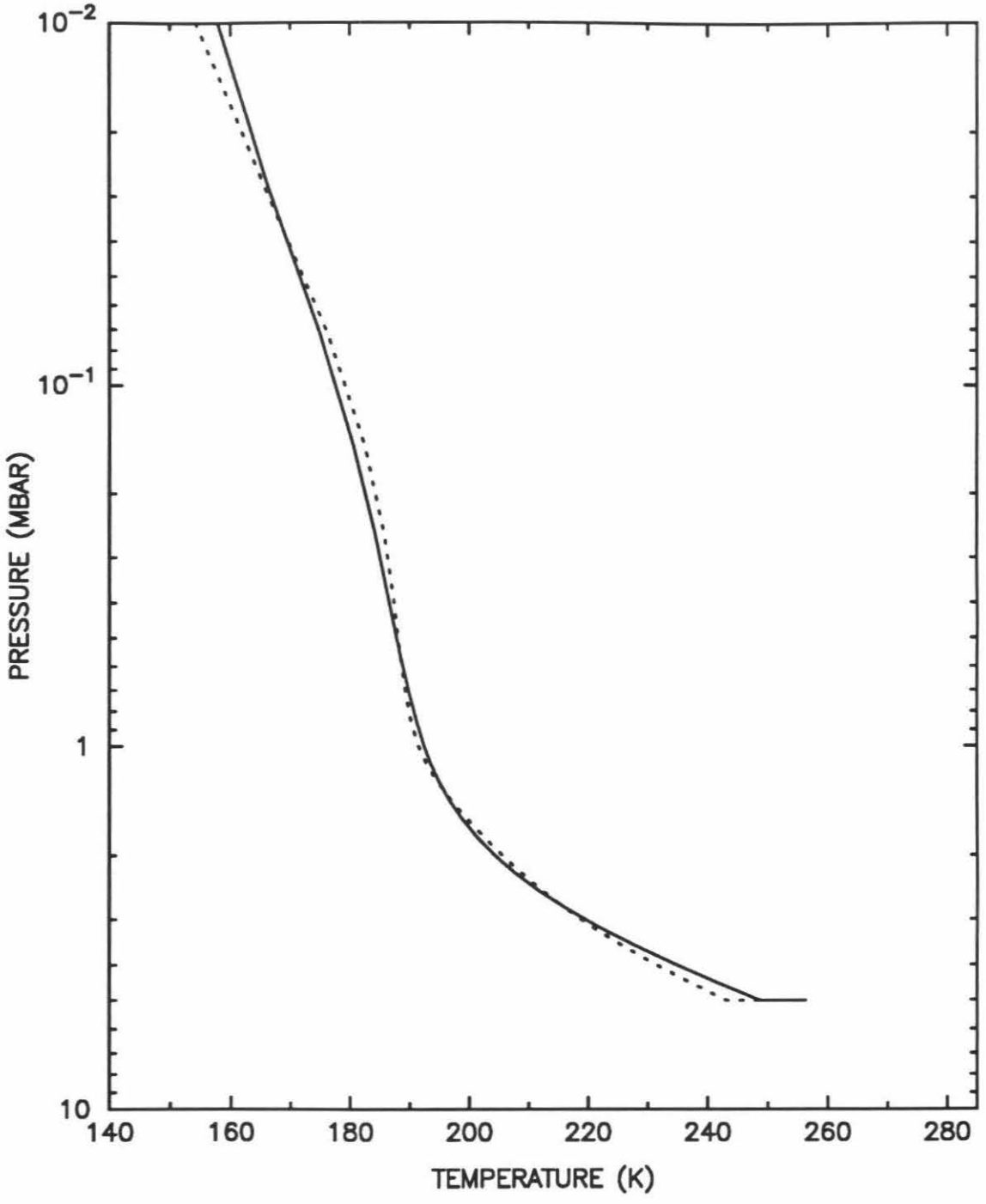

Figure 6a. (a) A simulation in which the atmosphere is assumed to be completely clear and only temperatures are retrieved (dashed lines) is compared to a simulation in which dust absorption is included in the calculation of the atmospheric transmittances, and temperatures and dust optical depths are retrieved simultaneously (solid lines).

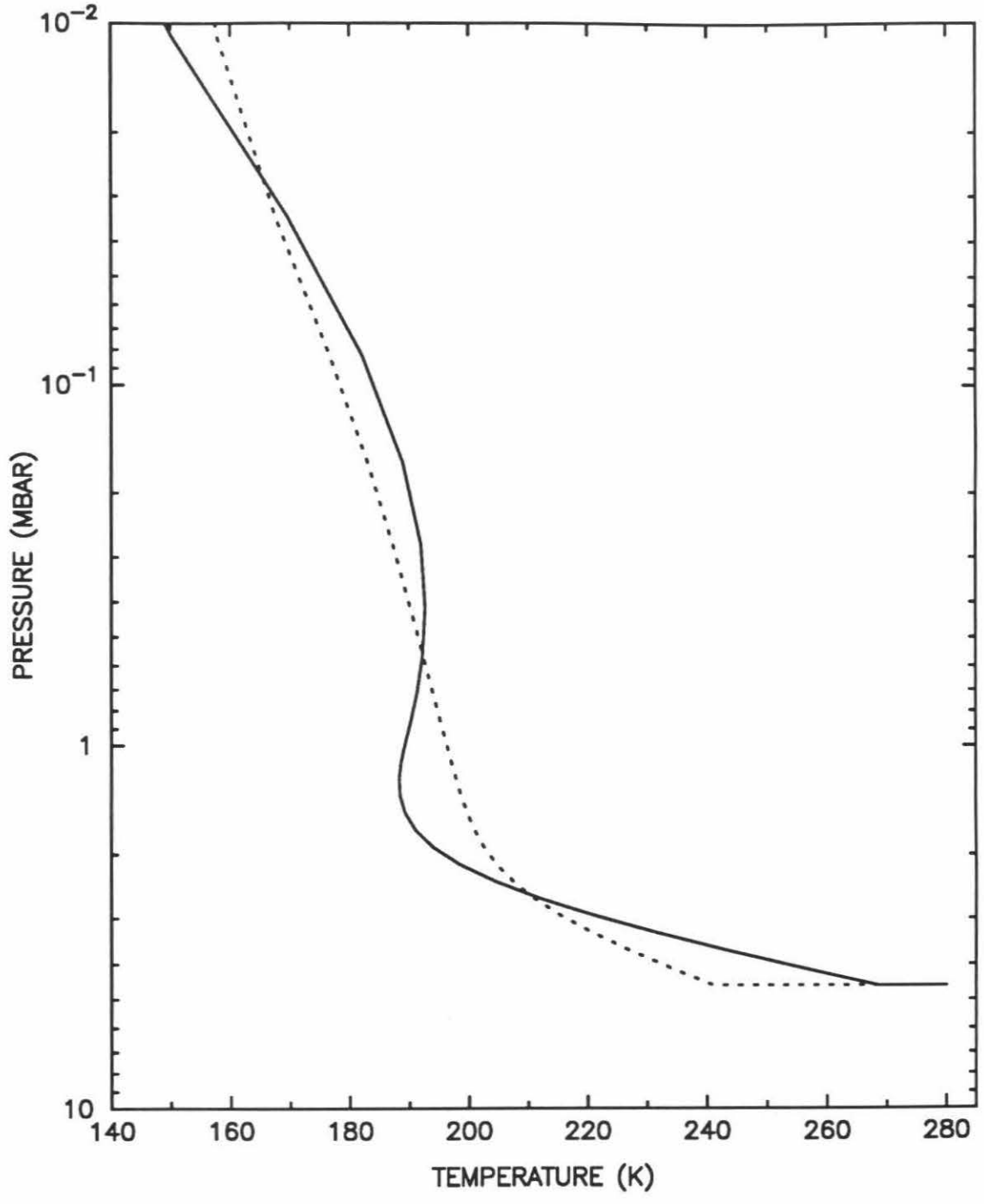

Figure 6b. (b) Same as Figure 6a, for a second test spectrum.

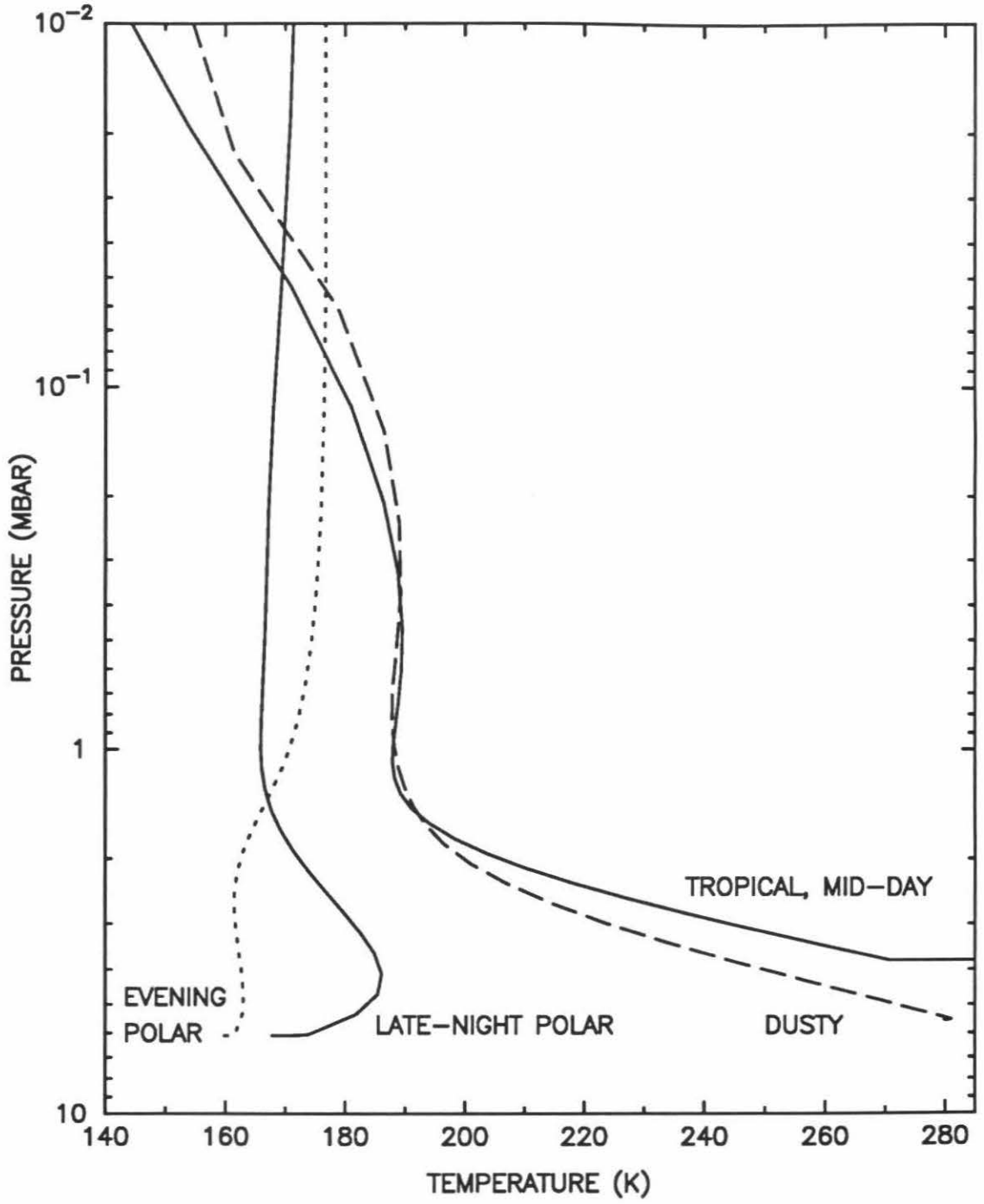

Figure 7a. Retrieved temperature profiles from the four sample spectra shown in Figure 2, plotted as a function of atmospheric pressure. The dusty spectrum is represented by a dashed line, and the evening polar spectrum is represented by a dotted line.

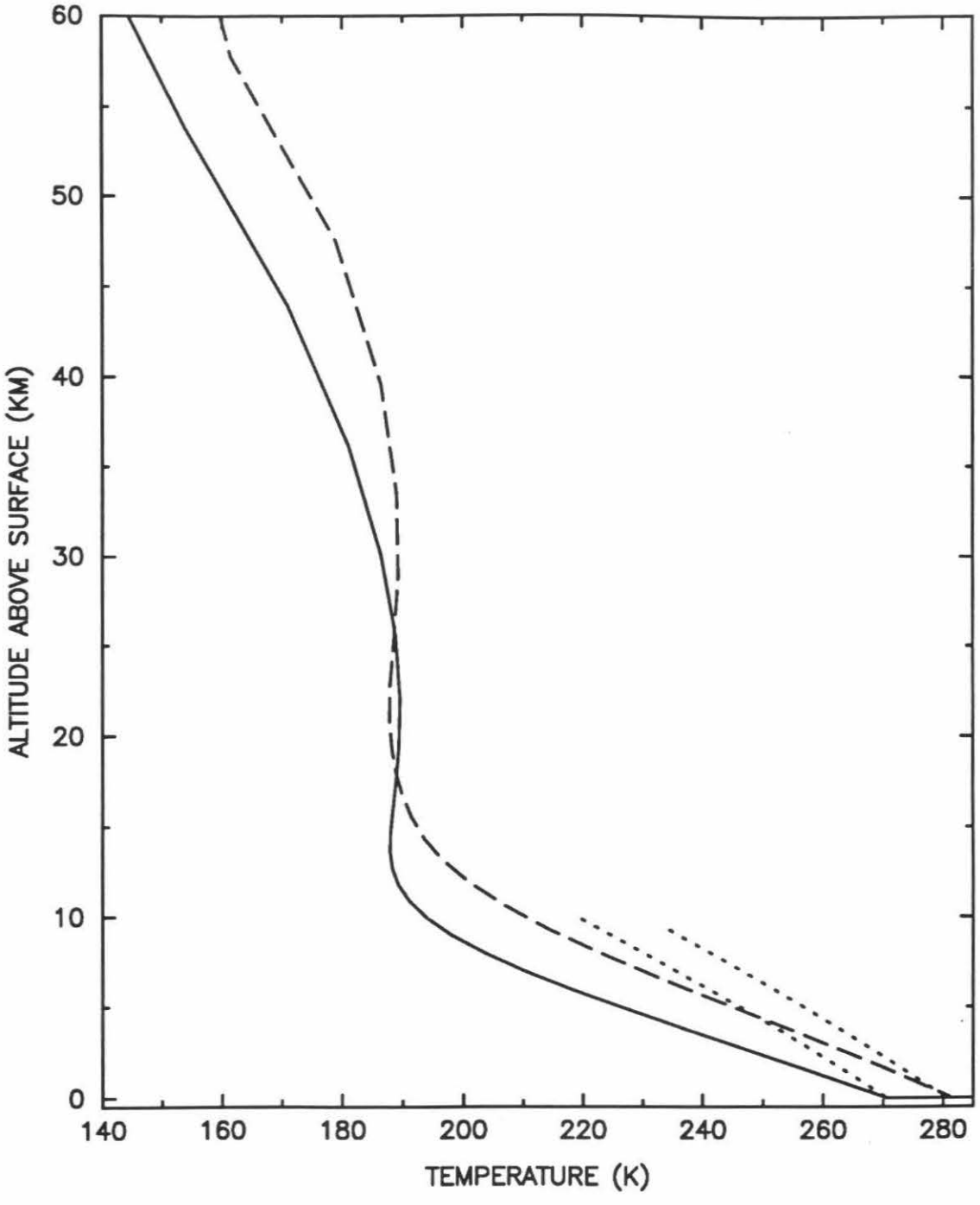

Figure 7b. Retrieved temperature profiles for the tropical, mid-day spectrum (solid line) and the dusty spectrum (dashed line), plotted as a function of altitude above the local surface. The dotted lines are the adiabats associated with each temperature profile.

trum, but this is simply a consequence of the fact that the temperature is plotted as a function of pressure. Plotting these two temperature profiles as a function of altitude above the local surface (Figure 7b) reveals that the temperatures of the dusty spectrum are warmer at most levels. The thin Martian atmosphere does not have enough heat capacity to produce effects like those associated with topography on Earth (*e.g.*, hot Death Valley, cold Mt. Everest). For comparison purposes, the adiabats associated with each temperature profile are also included in this figure. The similarity of the two mid–day profiles in Figure 7b, and their super–adiabatic vertical gradients in the region below 10 km, indicate that the daytime tropospheric thermal structure on Mars is controlled primarily by the temperature of the lowest atmospheric layer and local free convection. Absorption of solar radiation by airborne dust plays a much smaller role at these altitudes for the low–dust conditions represented in our data subset. This interpretation is supported by 1–D radiative–convective–equilibrium experiments [*Crisp et al.*, 1989].

The polar spectra in Figure 7a are both characterized by atmospheric temperatures that are warmer than the surface. These profiles illustrate the much more isothermal conditions that prevail near the polar night terminator. Strong inversions, in which atmospheric temperatures exceed the surface temperature by up to 40 K, occur in both polar regions at all times of day. In addition, strong lower–atmosphere inversions are seen in the equatorial regions in the late night and early morning hours.

Observed and computed brightness temperatures for the four sample spectra are compared in Figure 8. There is a small mismatch in the short–wavenumber wing of the tropical, mid–day spectrum, which is probably due to imperfect dust optical properties or a slight error in the value of the surface emissivity. The fit to the dusty spectrum is not as good in the near–wing regions, where airborne dust exerts the strongest influence on the temperature retrieval. For the polar spectra, the computed

brightness temperatures are too warm on the short–wavenumber side and too cool on the long–wavenumber side. The apparent slope in the observed spectra may indicate either the presence of airborne water ice or a low–emissivity surface, neither of which are currently included in the retrieval algorithm.

5.3 Dust Amounts and Distribution

Retrieved variations in the column–integrated 9 μm dust optical depth with latitude are shown in Figure 9. Not all spectra are represented on this plot because the dust retrieval procedure is not performed on spectra with a surface/atmosphere temperature difference less than 15 K, eliminating most late night and winter polar spectra. The temperature contrast constraint is applied by comparing the initial surface temperature guess described in Section (4.1) to the initial high–altitude atmospheric temperature guess described in Section (4.2). Dust optical depth retrievals are not attempted on spectra that fail this test. The histogram in Figure 9 indicates which regions have sufficient temperature contrasts to allow dust retrievals to be performed.

The median column–integrated dust optical depth is ~ 0.2. The highest opacities ($\sim$ 0.4) occur in the equatorial regions, and the dust amounts south of the equator are slightly higher than they are to the north. Both of these trends were reported by *Martin* [1986] based on an analysis of Viking IRTM 9 μm channel data that encompassed both 1977 global dust storms. These results are also consistent with the findings of *Anderson and Leovy* [1978] from Mariner 9 television reflectance profiles which crossed the limb of Mars. They found that the dust decay rate during the post–storm phase was much faster in the high latitude regions than in the equatorial zone, and they concluded that significant amounts of dust remained in the atmosphere above the equator long after the dust storm had subsided. The low dust values at 60° S in Figure 9 are most likely an artifact of the early–morning sampling.

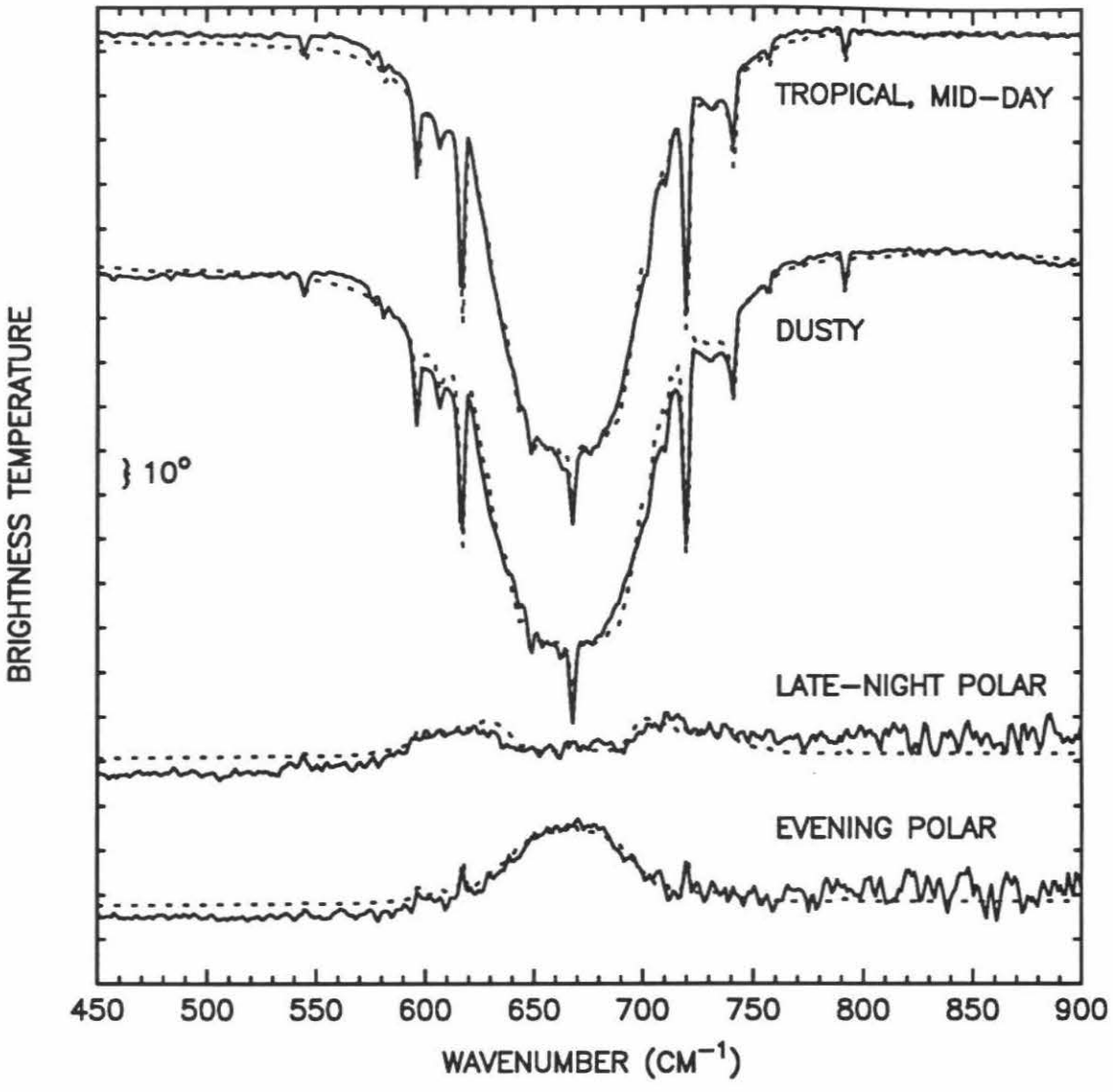

Figure 8. Observed (solid lines) and computed (dotted lines) brightness temperatures from the four sample spectra shown in Figure 2. The spectra were offset from one another by adding constant factors to the brightness temperatures, so the vertical scale was omitted on this plot. The distance between tick marks represents 10 K.

The histogram shows that the dust retrieval algorithm was performed on very few spectra in this region.

The optical depth above each atmospheric level is shown in Figure 10 for the two sample spectra from Figure 2 with sufficient thermal contrast. The column-integrated dust optical depth is 0.18 for the tropical, mid-day spectrum of Figure 2a and 0.43 for the dusty spectrum of Figure 2b. The dashed line in Figure 10 represents the initial dust profile (as defined by equation (21)) for the model atmosphere of the dusty spectrum. Although the magnitudes of the τ values change to reflect the overall dustiness of the atmospheric column for each spectrum, the general shape of the profile is not modified substantially by the dust retrieval algorithm. This implies that the initial vertical dust distribution provides an adequate fit to the observed radiances. However, these profiles are not unique because the dust retrieval algorithm does not strongly constrain the vertical distribution of the dust. Errors in the retrieved vertical dust distribution at altitudes where there are large vertical temperature gradients introduce uncertainties in the total dust column abundance. For example, in the presence of a large negative temperature lapse rate, a small amount of dust at a high altitude produces the same radiance signature as a large amount of dust near the surface.

If the dust particle size distribution and wavelength-dependent optical properties were known precisely, it would be possible to estimate dust optical depths at visible wavelengths from these observations. Unfortunately, these properties are not well constrained by the IRIS observations. Previous studies [*Zurek*, 1982; *Martin*, 1986] have suggested a ratio of visible to infrared optical depth of approximately two.

5.4 Surface Temperatures

Variations of surface temperature with latitude and time of day are shown in Figure 11. Surface temperatures from the irregularly-spaced spectra are mapped

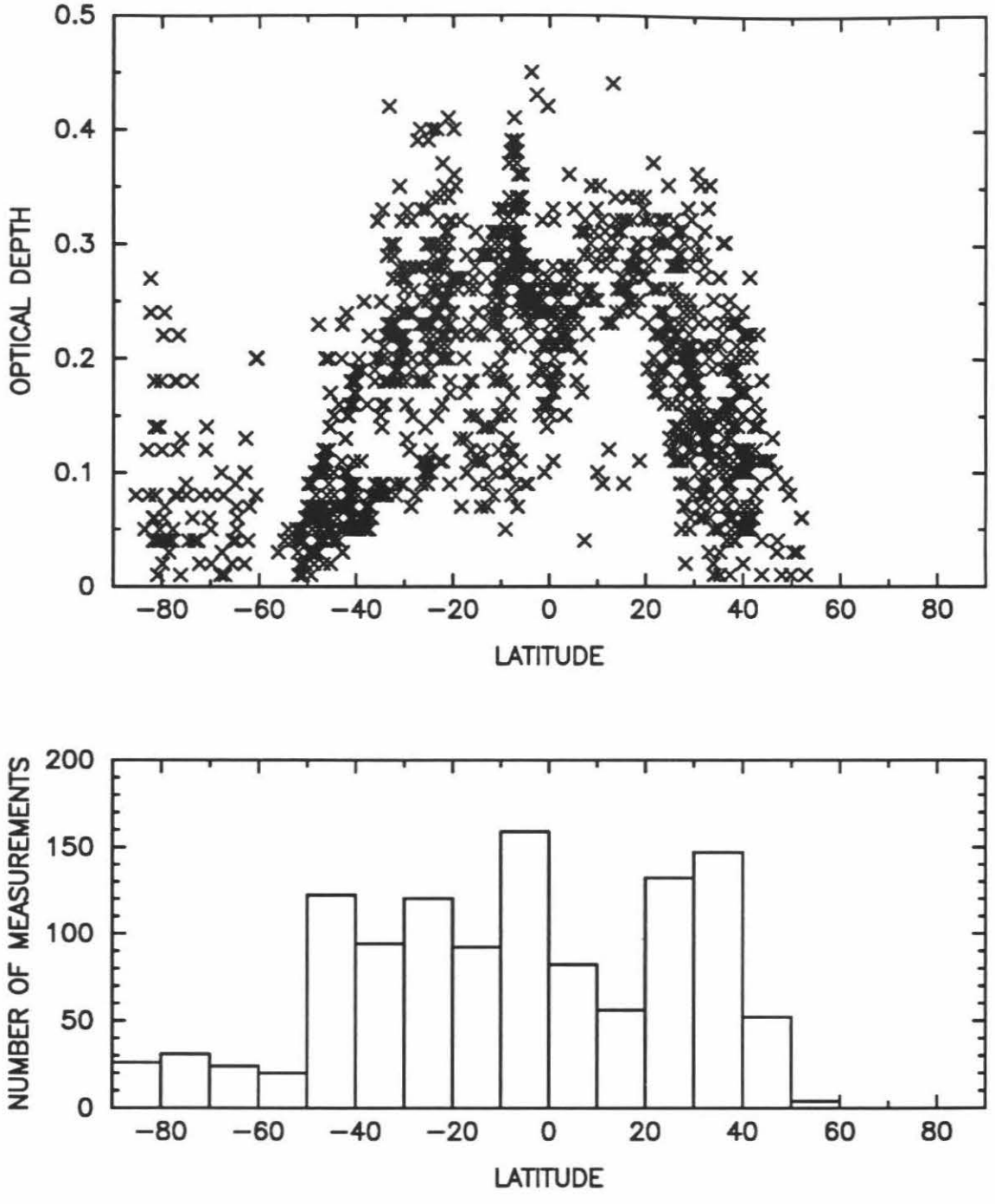

Figure 9. Variations in the column–integrated 9 μm dust optical depth with latitude. The histogram indicates how many spectra in each 10° latitude bin have a surface/atmosphere temperature contrast sufficient to allow dust retrievals to be performed.

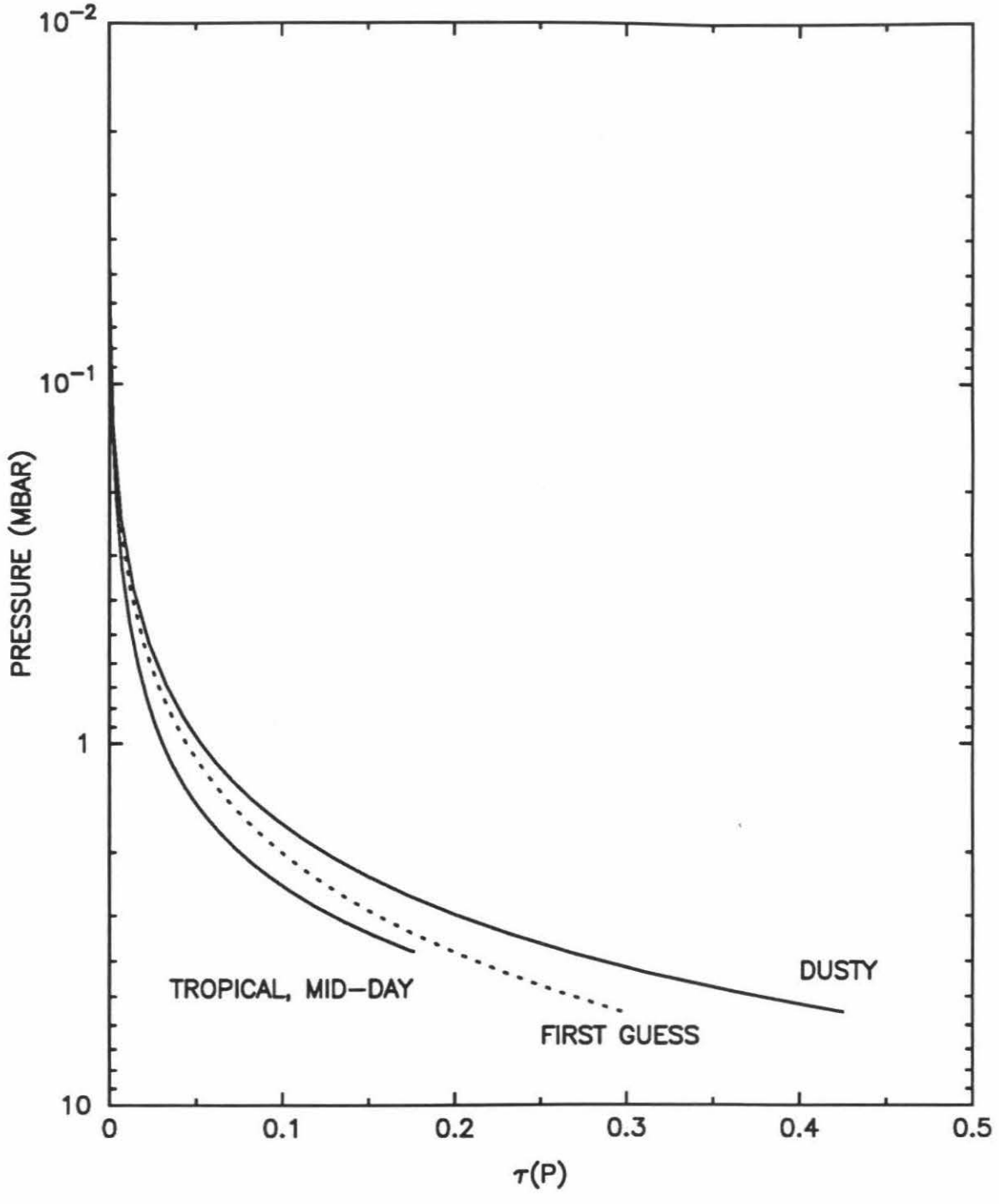

Figure 10. Retrieved dust optical depth profiles for the spectra in Figures 2a and 2b. The dashed line corresponds to the initial vertical dust distribution for the dusty spectrum of Figure 2b.

onto a regular grid using the weighted–average interpolation program discussed in Section 3.4. Results from all twelve measurement days have been averaged together. Temperature contours in the map are interrupted in places where data are sparse or absent. Temperatures near the north pole, which is in perpetual darkness at this season, remain nearly constant at $\sim$ 160 K. The highest surface temperatures ($>$ 280 K) occur at mid–day at the sub–solar latitude ($\sim$ 6° S). The amplitude of the day/night temperature variation at the equator exceeds 100 K. Diurnal variations of this magnitude in the equatorial latitudes were also seen under relatively clear conditions in Viking IRTM 7 μm channel data [*Martin et al.*, 1979] and 20 μm channel data [*Martin*, 1981]. The limited time–of–day coverage in Figure 11 allows post–dawn warming to be seen only in the southern polar regions. At 60° S, the surface temperature increases from $\sim$ 180 K to 220 K between 6 AM and 11 AM; the surface temperature at the south pole increases by 20 K during this interval. This rapid rise in surface temperature after dawn is also consistent with Viking IRTM data [*Martin et al.*, 1979]. These surface temperature results can be explained in the following way. The thin Martian atmosphere is composed mainly of CO_2, which is a poor absorber at visible wavelengths. The bulk of the incoming solar radiation is therefore deposited at the surface, where it is very efficiently absorbed. Because the surface pressure is so low, resulting in a weak greenhouse effect, and because the thermal inertia of the Martian soil is generally low [*Palluconi and Kieffer*, 1981], the diurnal variation in insolation drives a large surface temperature oscillation.

Hanel et al. [1972a] present a plot of surface temperatures similar to, and showing general agreement with, Figure 11. They estimate the surface temperature from the brightness temperature at 1300 cm^{-1} for Orbits 161–186. While the overall behavior of the surface temperature matches very well (typically to within 10 K), we find temperatures in both polar regions 20 K cooler than those reported by *Hanel et*

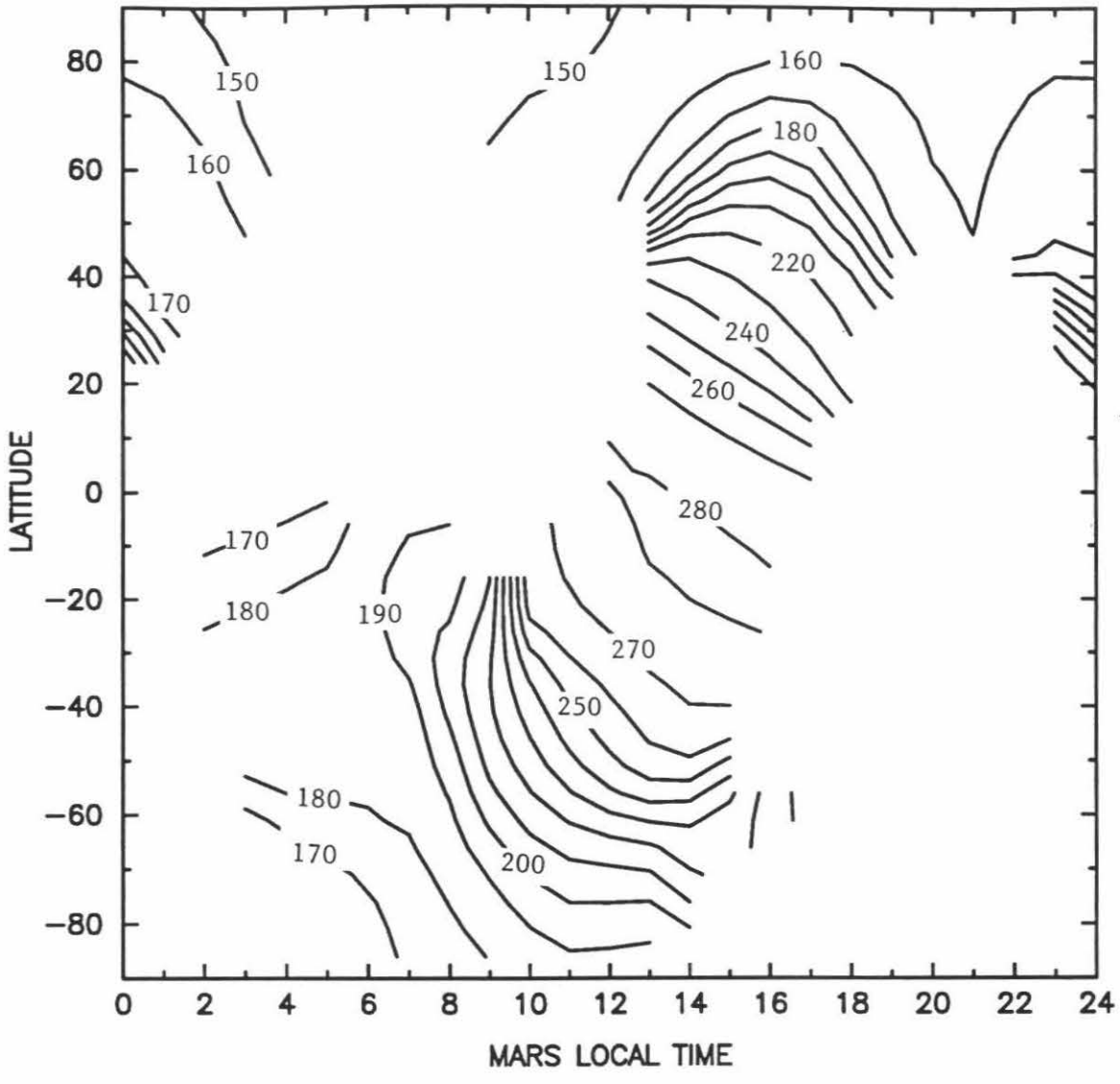

Figure 11. Variations of surface temperature with latitude and time of day. Temperature contours in the map are interrupted in places where data are sparse or absent.

al. [1972a]. It is possible that further clearing of the atmosphere during the timeframe represented in Figure 11 (Orbits 180–200) resulted in greater temperature contrast across the planet. Information about the surface temperature was also provided by another Mariner 9 instrument: the infrared radiometer. *Kieffer et al.* [1973] present a plot of 10 μm brightness temperatures averaged over 60 revolutions centered around February 17, 1972 (Orbit 190). The temperatures depicted there and in Figure 11 differ by 10 K or less for any given latitude and time of day.

5.5 Atmospheric Temperatures

Pole–to–pole descriptions of dayside and nightside atmospheric temperatures are shown in Figures 12a and 12b. They were produced by centering the weighted average interpolation at 2 PM and 2 AM, respectively. In the averaging process, all surface pressure values are interpolated to 6.0 mbar. In the afternoon (Figure 12a), the temperature in the 1.0 mbar region exhibits maxima in the midlatitudes of both hemispheres, and then decreases between the midlatitudes and the equator. Similar trends appeared in Viking IRTM data [*Martin and Kieffer*, 1979] and in a previous study of Mariner 9 IRIS data [*Conrath*, 1981], although the latter reported only a northern–hemisphere mean meridional temperature cross–section constructed by averaging spectra in a 50–day period. A similar thermal structure is also evident in the latitude/pressure temperature cross–sections predicted by general circulation model simulations [*Pollack et al.*, 1990]. In the lower atmosphere, temperatures increase monotonically from the polar regions toward the equator.

The highest daytime atmospheric temperatures (> 260 K) are found at low altitudes near the sub–solar point, while the coldest temperatures (< 150 K) are found at levels near 1.0 mbar over the winter pole. During the day (Figure 12a), solar heating of the surface produces high surface temperatures and a strong negative temperature gradient with altitude in the lower atmosphere, indicating that the thermal structure

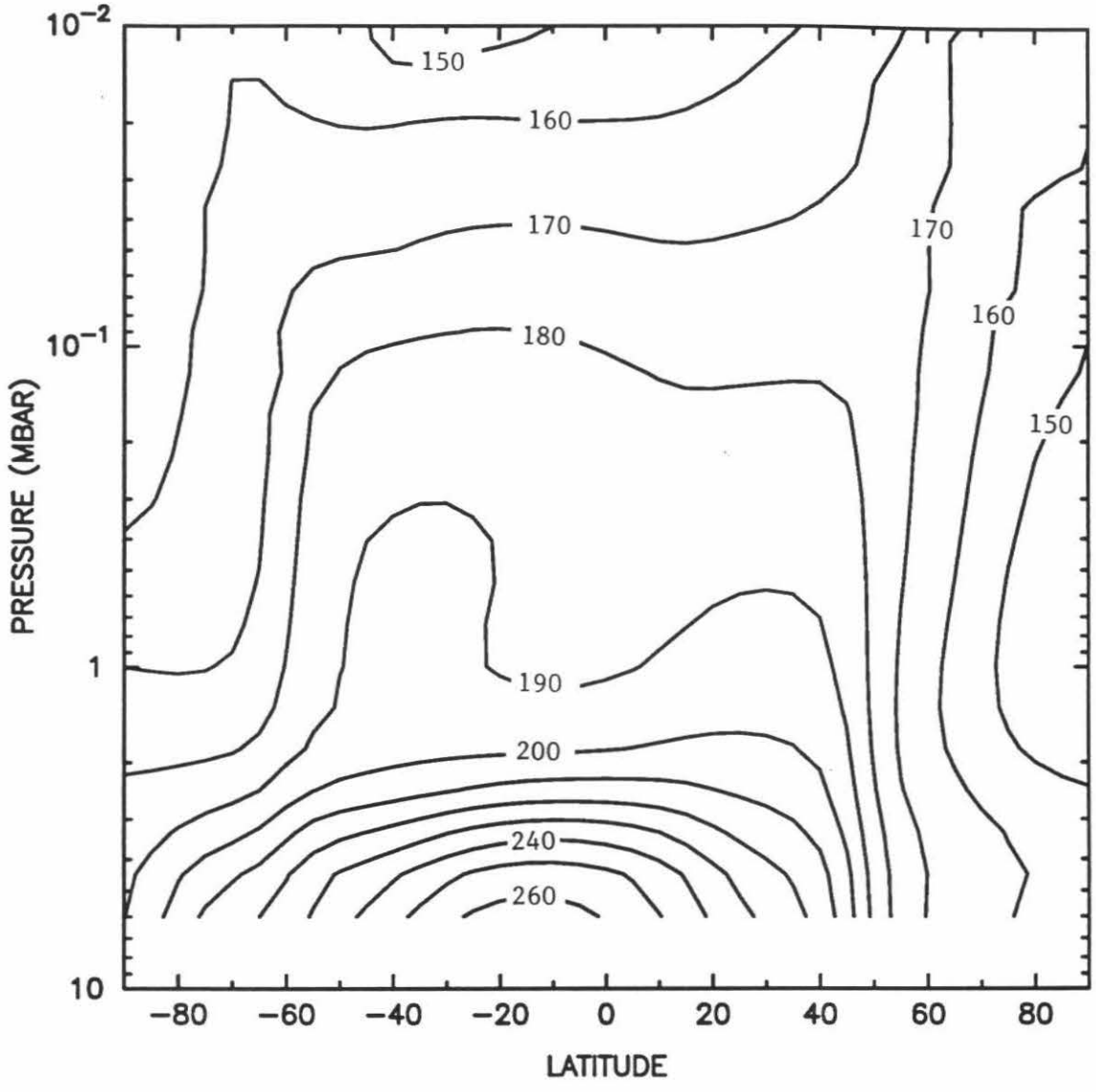

Figure 12a. Pole–to–pole description of dayside atmospheric temperatures, constructed by centering the weighted–average interpolation at 2 PM.

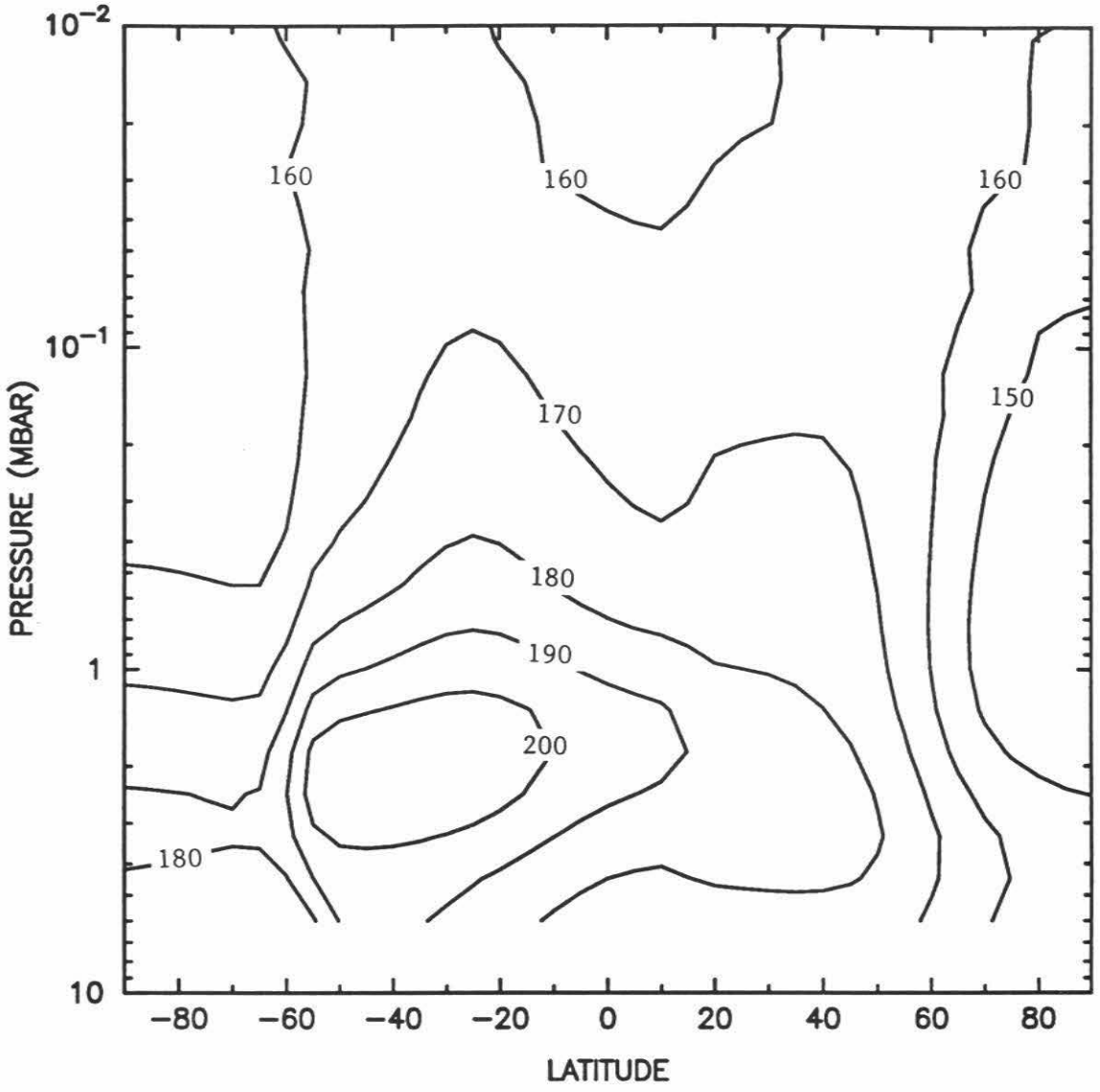

Figure 12b. Pole–to–pole description of nightside atmospheric temperatures, constructed by centering the weighted–average interpolation at 2 AM.

in this region is dominated by convective heat transport. At night (Figure 12b), the surface cools precipitously and a strong temperature inversion arises near the surface, indicating the formation of a much more stable regime. The thin Martian CO_2 atmosphere responds much more quickly to forcing by the diurnal surface temperature oscillation than does the terrestrial atmosphere, whose variations are moderated by its higher thermal inertia and the presence of the oceans. Differencing the temperature maps at 2 PM and 2 AM (Figure 12c) reveals diurnal temperature changes as large as 80 K at low altitudes near the sub–solar latitude. Diurnal temperature changes at pressures less than 1.0 mbar are typically about 10 K.

To facilitate comparisons with Viking IRTM 15 μm channel data, the weighted–average interpolation program was centered about 0.5 mbar ($\sim$ 25 km). The resulting temperatures are plotted as a function of Mars local time of day and latitude in Figure 12d. There are no published descriptions of Viking 15 μm temperatures in the range of L_S covered by our data subset, but our results can be compared to Viking temperatures acquired in relatively clear periods during $L_S = 120° - 125°$ [*Martin and Kieffer*, 1979], and $L_S = 84° - 126°$ and $L_S = 50° - 70°$ [*Martin*, 1981]. These L_S ranges correspond to late northern spring and early summer, when the meridional temperature structure should be nearly reversed from that of our results. The general behavior depicted in Figure 12d agrees well with the Viking results. There is a strong latitudinal gradient in the winter polar region, and a small diurnal variation towards the summer pole. The maximum temperatures appear to occur near midday in the equatorial region, and the minimum temperatures appear to occur near 6 AM. However, the limited data coverage (there are essentially no late afternoon or evening data points in the southern hemisphere) precludes us from conclusively determining the times of the temperature extrema. Specifically, the highest temperatures (> 190 K) in our results occur at 2 PM at 30° S, while the highest temperatures (> 186 K) for

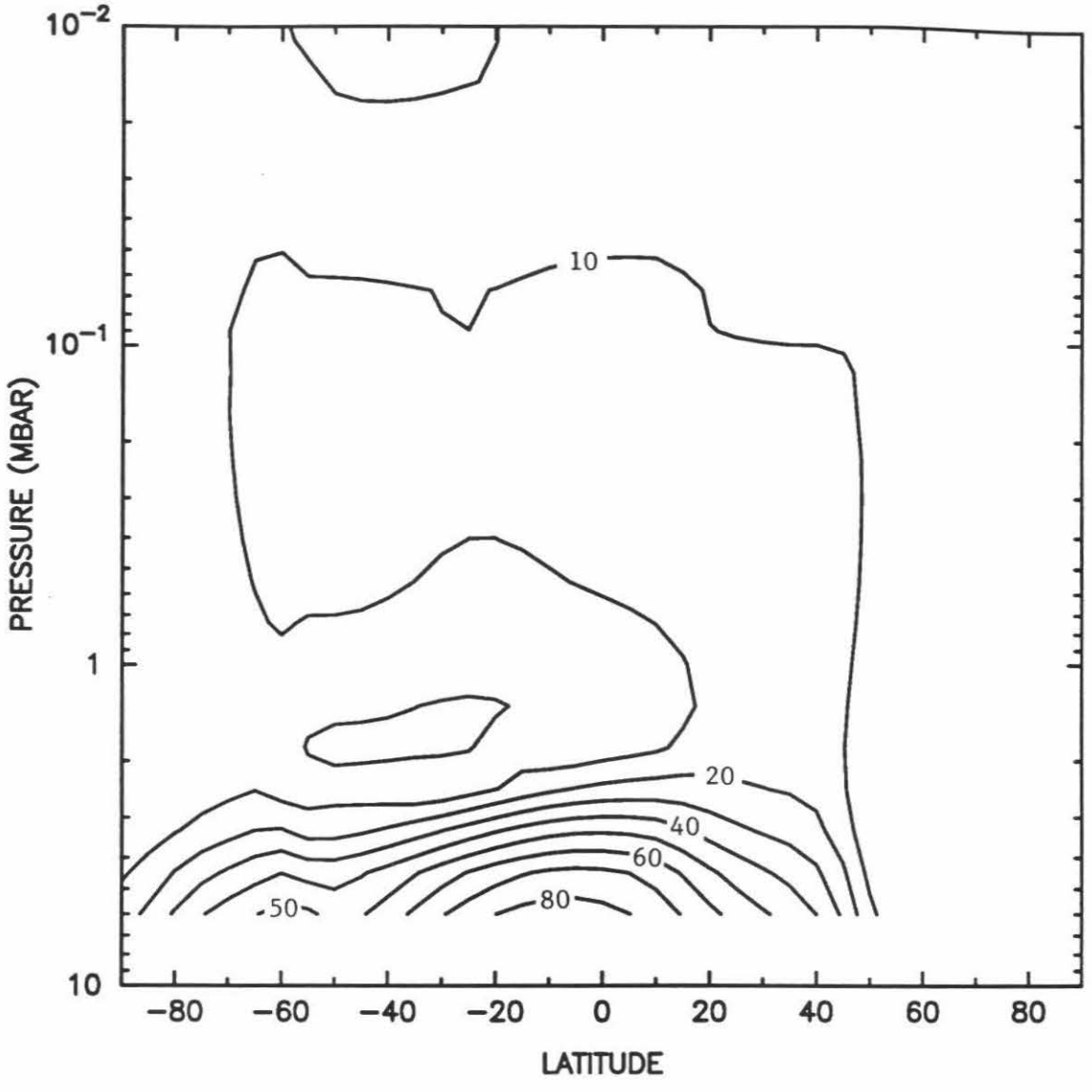

Figure 12c. Difference between the temperature maps at 2 PM and 2 AM, indicating diurnal temperature changes.

the $L_S = 120°$ case [*Martin and Kieffer*, 1979] occur at 2 PM at 30° N. In addition, there is evidence in Figure 12d for a secondary maximum in the early morning and a secondary minimum in the late evening, as reported by *Martin and Kieffer* [1979]. Despite the large separation in L_S between the data sets, the temperatures shown in Figure 12d never differ by more than 20 K from the Viking data at the same latitude and time of day. This implies that, in the absence of dust storms, there is little seasonal or interannual variation in atmospheric temperatures at this altitude.

Day–to–day temperature variations for two 10° latitude bins are shown in Figure 13. To avoid introducing a time–of–day bias, only spectra from similar times of day are included in each latitude bin (*cf.* Figure 1a). The largest atmospheric temperature changes are seen at high northern latitudes. The 60°–70° N latitude bin (Figure 13a) exhibits temperature variations which have amplitudes exceeding 25 K. These temperature fluctuations are not correlated with any known surface topography or albedo variations, indicating that they may be associated with a passing weather system. This conclusion is supported by the fact that the temperature variations extend over a range of altitudes, and it is consistent with *Conrath* [1981], who found strong wave–like perturbations in a similar subset of IRIS data in a latitude band between 45° N and 65° N.

Temperature variations are also evident at low latitudes, but these changes, which are localized near the surface, can be accounted for by the different surface characteristics of the contributing spectra. There is a 30 K variation in near–surface atmospheric temperature between Day 7 and Day 9 in the 0°–10° N latitude bin (Figure 13b). The Day 7 spectra were all recorded over Syrtis Major Planitia — a high–altitude region with low albedo. Due to the $\sim$ 9°/day eastward drift of the subspacecraft longitude, the Day 9 spectra were all recorded over Isidis Planitia — a low–altitude region with high albedo. The near–surface temperature changes appear

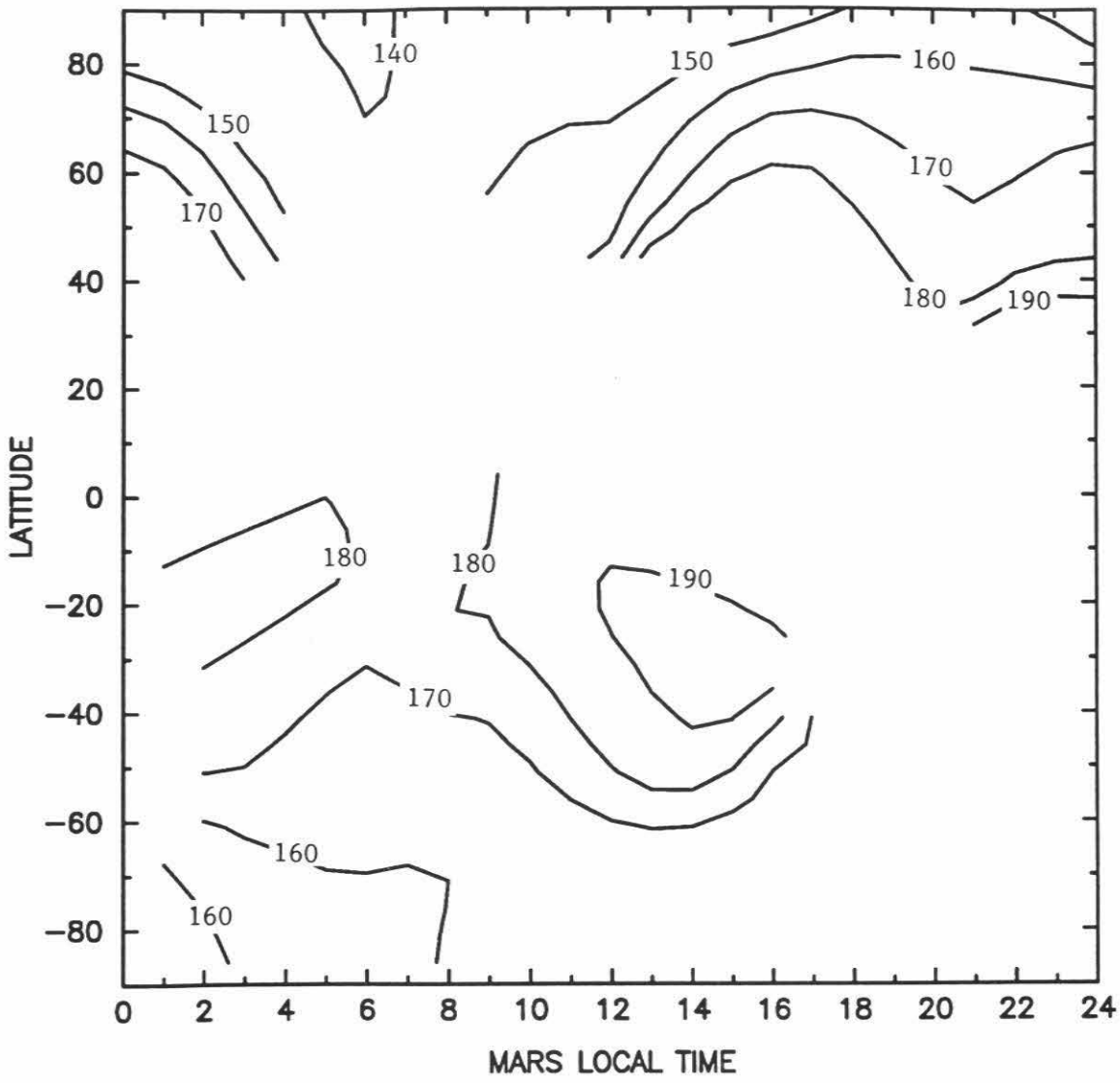

Figure 12d. Mariner 9 IRIS atmospheric temperatures at the 0.5 mbar level as a function of local time and latitude. These temperatures correspond to the temperatures derived from Viking IRTM 15 μm channel data.

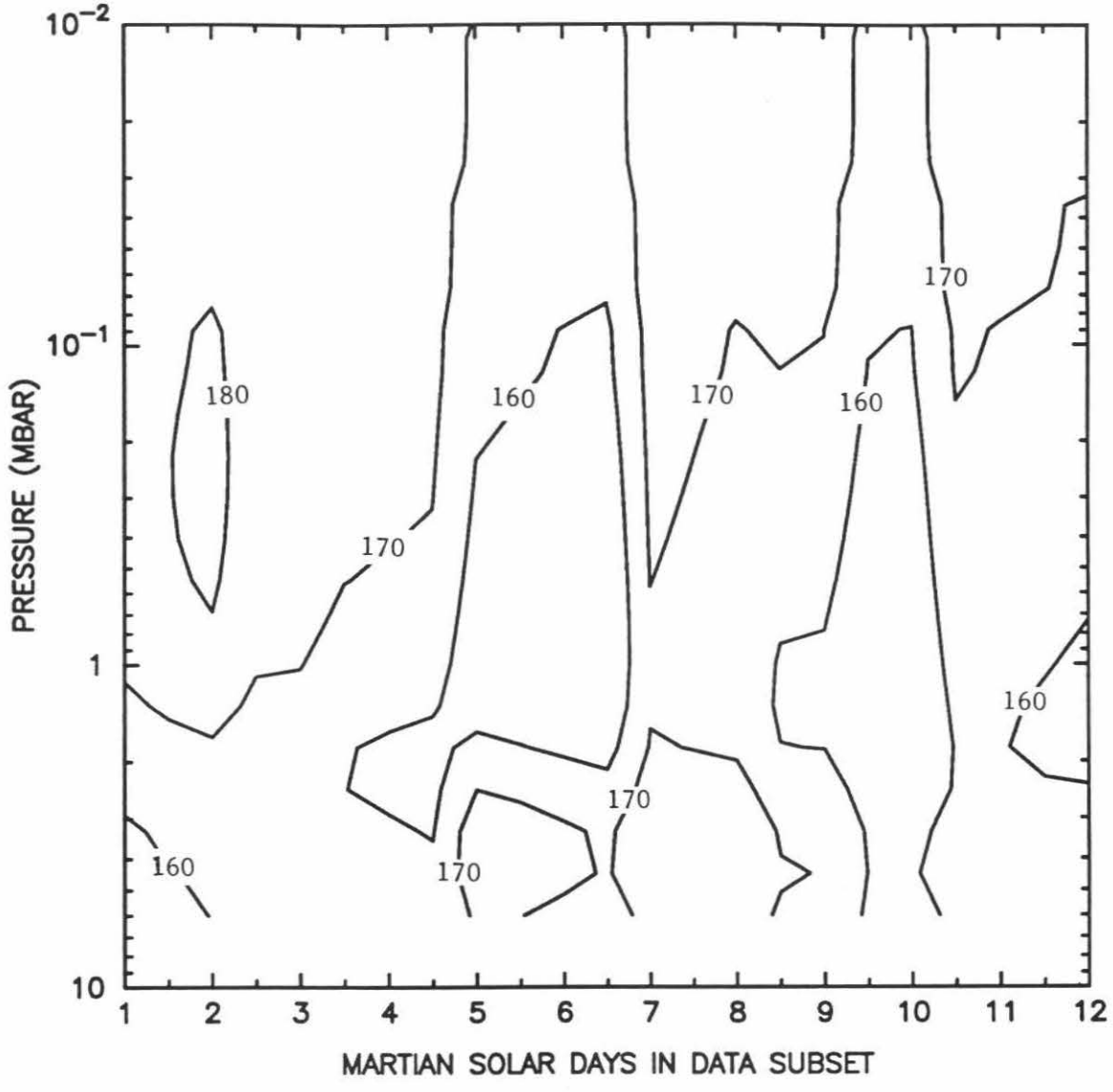

Figure 13a. Day–to–day temperature variations for the 60° – 70° N latitude bin. All spectra represented on this plot were recorded between 18.0 and 22.0 Mars local time.

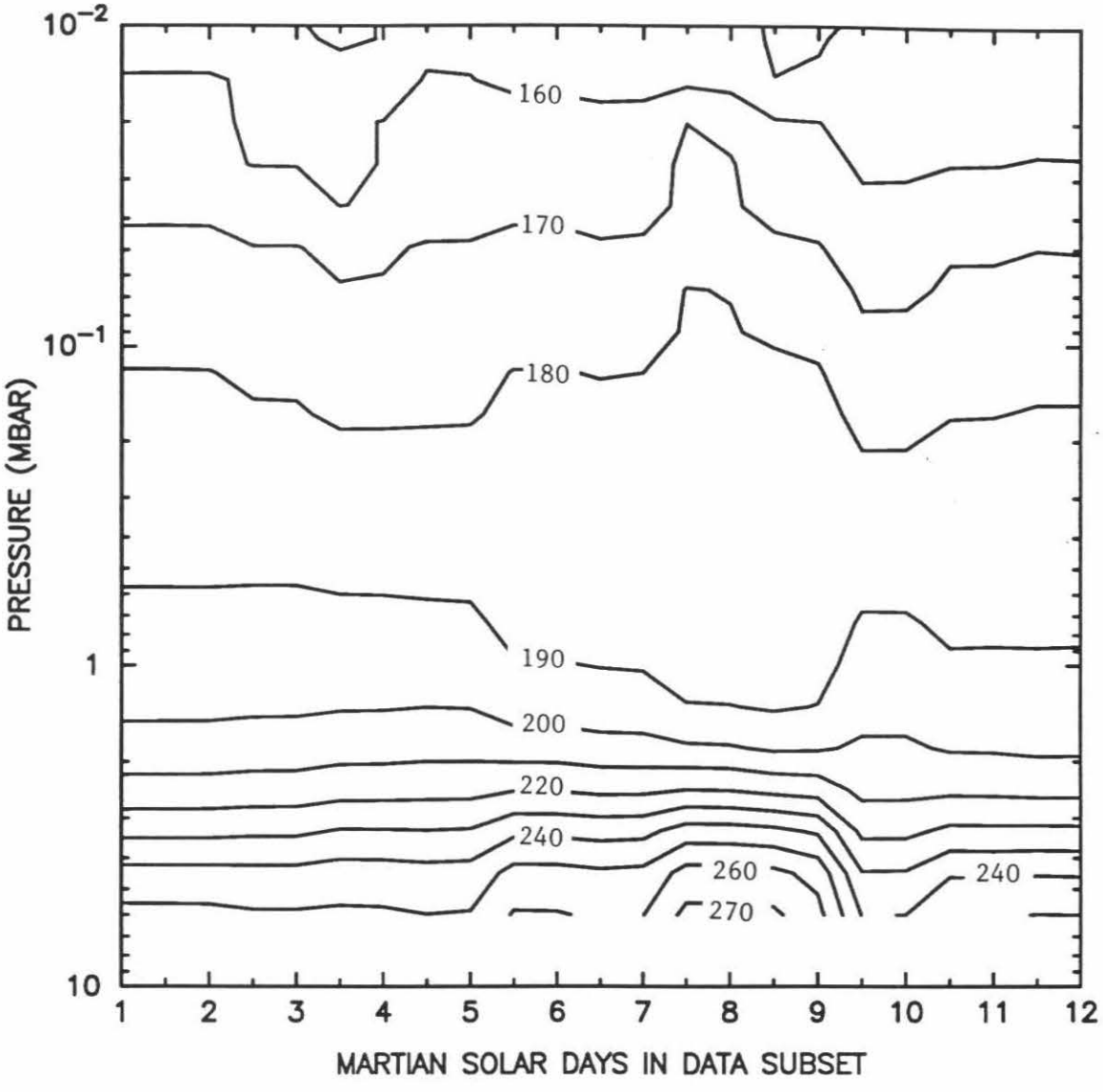

Figure 13b. Day–to–day temperature variations for the 0° – 10° N latitude bin. All spectra represented on this plot were recorded between 13.5 and 15.5 Mars local time.

to be anti–correlated with the variations in the upper atmosphere, a feature that is currently not well understood.

From Figures 12a and 12b (and from Figure 7a) we see that, at altitudes below 40 km ($\sim$ 0.1 mbar), the lowest atmospheric temperatures are found over the winter pole. However, both dayside and nightside atmospheric temperatures above about 40 km are warmer over the winter (north) polar regions than over the equator or the summer (south) polar regions. These anomalously–warm high–altitude temperatures in the northern polar regions are consistent with the ground–based observations of *Deming et al.* [1986] and *Rothermel et al.* [1988], which revealed polar warming in the middle atmosphere (50–85 km). This high–latitude warming, which our results indicate extends down to approximately the 40 km level, must be maintained through a dynamical heating mechanism. Thus the thermal structure derived from the Mariner 9 IRIS data suggests the existence of a net meridional circulation with rising motion at low latitudes, poleward flow at altitudes above 40 km, and subsidence over the poles. Similar circulations have been proposed for the mesospheres of Earth [*Leovy*, 1964] and Venus [*Crisp*, 1989]. Because a meridional circulation transports atmospheric constituents as well as heat, it has significant implications for the role of the atmosphere in the seasonal cycles of dust and water on Mars. For example, this circulation might provide a mechanism for transporting dust and water ice from low latitudes into the polar regions.

6. Summary

We have described a new technique for the simultaneous estimation of atmospheric and surface temperatures and airborne dust abundances from thermal emission spectra. This algorithm was used with Mariner 9 IRIS observations to obtain a comprehensive representation of the temperature structure and dust loading of the Martian atmosphere in a relatively clear period during late southern summer. We have

presented the first pole–to–pole description of atmospheric temperature, from the surface to approximately 60 km, at midday and in the middle of the night. We have also presented the first global picture of dust optical depths derived self–consistently along with the temperature profiles. These results provide a timely baseline for the Pressure Modulator Infrared Radiometer (PMIRR) and Thermal Infrared Spectrometer (TES) instruments currently scheduled to fly on the Mars Observer mission. The main conclusions of this work are summarized below:

- The presence of dust absorption in the retrieval algorithm can cause the derived temperatures to change by more than 20 K in some atmospheric layers, and it also significantly reduces the derived temperature difference between the surface and the atmospheric layer adjacent to the surface.
- For this relatively clear subset of the IRIS data, the median column–integrated 9 μm dust optical depth is ~ 0.2, with the highest opacities (~ 0.4) occurring in the equatorial regions. The dust retrieval algorithm does not strongly constrain the vertical distribution of the dust, and consequently the total column abundances are also uncertain.
- The amplitude of the diurnal surface temperature oscillation exceeds 100 K at the equator, but is virtually zero at the winter pole. The surface temperature increases rapidly after dawn. These results are in good agreement with previous conclusions based on both Mariner 9 data [*Hanel et al.*, 1972a; *Kieffer et al.*, 1973] and Viking data [*Martin*, 1981; *Martin et al.*, 1979].
- The day/night atmospheric temperature difference can reach 80 K at low altitudes near the sub–solar latitude. Daytime tropospheric temperatures are controlled primarily by strong surface heating and local free convection. At night, the surface temperature plummets and a strong near–surface temperature inversion forms.

- Comparison with Viking 15 μm IRTM data reveals little seasonal or interannual variation in atmospheric temperatures at the 0.5 mbar level for similar, low–dust conditions.
- Day–to–day temperature fluctuations which might be associated with a passing weather system are present at high northern latitudes, but do not appear elsewhere on the planet.
- Both dayside and nightside atmospheric temperatures above about 40 km are warmer over the winter polar regions than over the equator or the summer polar regions, suggesting the existence of a net meridional circulation with rising motion at low latitudes, poleward flow at altitudes above 40 km, and subsidence over the poles. This circulation might provide a mechanism for transporting dust and water ice from low latitudes into the polar regions.

References

Anderson, E. and C. Leovy, Mariner 9 television limb observations of dust and ice hazes on Mars, *J. Atmos. Sci.*, *35*, 723–734, 1978.

Chahine, M. T., Determination of the temperature profile in an atmosphere from its outgoing radiance, *J. Opt. Soc. Am.*, *58*, 1634–1637, 1968.

Chahine, M. T., Inverse problems in radiative transfer: Determination of atmospheric parameters, *J. Atmos. Sci.*, *27*, 960–967, 1970.

Chahine, M. T., A general relaxation method for inverse solution of the full radiative transfer equation, *J. Atmos. Sci.*, *29*, 741–747, 1972.

Conrath, B. J., Vertical resolution of temperature profiles obtained from remote radiation measurements, *J. Atmos. Sci.*, *29*, 1262–1271, 1972.

Conrath, B. J., Thermal structure of the Martian atmosphere during the dissipation of the dust storm of 1971, *Icarus*, *24*, 36–46, 1975.

Conrath, B. J., Influence of planetary–scale topography on the diurnal thermal tide during the 1971 Martian dust storm, *J. Atmos. Sci.*, *33*, 2430–2439, 1976.

Conrath, B. J., Planetary–scale wave structure in the Martian atmosphere, *Icarus*, *48*, 246–255, 1981.

Conrath, B., R. Curran, R. Hanel, V. Kunde, W. Maguire, J. Pearl, J. Pirraglia, J. Welker, and T. Burke, Atmospheric and surface properties of Mars obtained by infrared spectroscopy on Mariner 9, *J. Geophys. Res.*, *78*, 4267–4278, 1973.

Crisp, D., Radiative forcing of the Venus mesosphere: II. Thermal fluxes, cooling rates, and radiative equilibrium temperatures, *Icarus*, *77*, 391–413, 1989.

Crisp, D., Infrared radiative transfer in the dust–free Martian atmosphere, *J. Geophys. Res.*, *95*, 14,577–14,588, 1990.

Crisp, D., S. B. Fels, and M. D. Schwarzkopf, Approximate Methods for Finding CO_2 15 μm Band Transmission in Planetary Atmospheres, *J. Geophys. Res.*, *91*, 11,851–11,866, 1986.

Crisp, D., M. L. Santee, D. A. Paige, and R. A. West, Radiative processes in the Martian atmosphere, Paper presented at the *Fourth International Conference on Mars*, NASA, Tucson, AZ, 1989.

Deming, D., M. J. Mumma, F. Espenak, T. Kostiuk, and D. Zipoy, Polar warming in the middle atmosphere of Mars, *Icarus*, *66*, 366–379, 1986.

Eckstein, B. A., Evaluation of spline and weighted average interpolation algorithms, *Computers & Geosciences*, *15*, 79–94, 1989.

Evans, D. L. and J. B. Adams, Comparison of Viking Lander multispectral images and laboratory reflectance spectra of terrestrial samples, *Proc. Lunar Planet. Sci. Conf.*, *10th*, 1829–1834, 1979.

Goody, R. M. and Y. L. Yung, *Atmospheric Radiation: Theoretical Basis*, p. 519, Oxford University Press, 1989.

Hanel, R., B. Conrath, W. Hovis, V. Kunde, P. Lowman, W. Maguire, J. Pearl, J. Pirraglia, C. Prabhakara, and B. Schlachman, Investigation of the Martian environment by infrared spectroscopy on Mariner 9, *Icarus*, *17*, 423–442, 1972a.

Hanel, R., B. Schlachman, E. Breihan, R. Bywaters, F. Chapman, M. Rhodes, D. Rodgers, and D. Vanous, Mariner 9 Michelson interferometer, *Applied Optics*, *11*, 2625–2634, 1972b.

Hanel, R., L. Herath, V. Kunde, and J. Pearl, Voyager infrared interferometer spectrometer and radiometer (IRIS) – Documentation for reduced data records (RDR) for Jupiter, NASA Technical Note X-693-821-8, Goddard Space Flight Center, 1980.

Hansen, J. E. and L. D. Travis, Light scattering in planetary atmospheres, *Space Sci. Rev.*, *16*, 527–610, 1974.

Hess, S. L., R. M. Henry, C. B. Leovy, J. A. Ryan, J. E. Tillman, T. E. Chamberlain, H. L. Cole, R. G. Dutton, G. C. Greene, W. E. Simon, and J. L. Mitchell, Preliminary meteorological results on Mars from the Viking 1 Lander, *Science*, *193*, 788–791, 1976.

Kieffer, H. H., Soil and surface temperatures at the Viking landing sites, *Science*, *194*, 1344–1346, 1976.

Kieffer, H. H., S. C. Chase, E. Miner, G. Münch, and G. Neugebauer, Preliminary report on infrared radiometric measurements from the Mariner 9 spacecraft, *J. Geophys. Res.*, *78*, 4291–4312, 1973.

Kliore, A. J., D. L. Cain, G. Fjeldbo, B. L. Seidel, M. J. Sykes, and S. I. Rasool, The atmosphere of Mars from Mariner 9 radio occultation measurements, *Icarus*, *17*, 484–516, 1972.

Leovy, C., Simple models of thermally driven mesospheric circulation, *J. Atmos. Sci.*, *21*, 327–341, 1964.

Lindal, G. F., H. Hotz, D. N. Sweetnam, Z. Shippony, J. P. Brenkle, G. V. Hartsell, and R. T. Spear, Viking radio occultation measurements of the atmosphere and topography of Mars: Data acquired during 1 Martian year of tracking, *J. Geophys. Res.*, *84*, 8443–8456, 1979.

Liou, K.–N., *An Introduction to Atmospheric Radiation*, p. 392, Academic Press, 1980.

Lorell, J., G. H. Born, E. J. Christensen, J. F. Jordan, P. A. Laing, W. L. Martin, W. L. Sjogren, I. I. Shapiro, R. D. Reasenberg, and G. L. Slater, Mariner 9 celestial mechanics experiment: Gravity field and pole direction of Mars, *Science*, *175*,

317–320, 1972.

Martin, T. Z., Mean thermal and albedo behavior of the Mars surface and atmosphere over a Martian year, *Icarus*, *45*, 427–446, 1981.

Martin, T. Z., Thermal infrared opacity of the Mars atmosphere, *Icarus*, *66*, 2–21, 1986.

Martin, T. Z. and H. H. Kieffer, Thermal infrared properties of the Martian atmosphere: 2. The 15 μm band measurements, *J. Geophys. Res.*, *84*, 2843–2852, 1979.

Martin, T. Z., A. R. Peterfreund, E. D. Miner, H. H. Kieffer, and G. E. Hunt, Thermal infrared properties of the Martian atmosphere: 1. Global behavior at 7, 9, 11, and 20 μm, *J. Geophys. Res.*, *84*, 2830–2842, 1979.

Owen, T., The composition of the Martian atmosphere, *Adv. Space Res.*, *2*, 75–80, 1982.

Pollack, J. B., R. M. Haberle, J. Schaeffer, and H. Lee, Simulations of the general circulation of the Martian atmosphere: 1. Polar processes, *J. Geophys. Res.*, *95*, 1447–1473, 1990.

Rodgers, C. D., Retrieval of atmospheric temperature and composition from remote measurements of thermal radiation, *Rev. Geophys. Space Phys.*, *14*, 609–624, 1976.

Rothermel, H., H. U. Käufl, U. Schrey, and S. Drapatz, Thermal structure of the Martian mesosphere, *Astron. Astrophys.*, *196*, 296–300, 1988.

Rothman, L. S., R. R. Gamache, A. Goldman, L. R. Brown, R. A. Toth, H. M. Pickett, R. L. Poynter, J.–M. Flaud, C. Camy–Peyret, A. Barbe, N. Husson, and M. A. H. Smith, The HITRAN database: 1986 edition, *Applied Optics*, *26*, 4058–4097, 1987.

Roush, T., J. Pollack, and J. Orenberg, Derivation of midinfrared (5–25 μm) optical constants of some silicates and palagonite, *Icarus*, *94*, 191–208, 1991.

Sieff, A. and D. Kirk, Structure of the atmosphere of Mars in summer at mid–latitudes, *J. Geophys. Res.*, *82*, 4364–4378, 1977.

Singer, R. B., Spectral evidence for the mineralogy of high–albedo soils and dust on Mars, *J. Geophys. Res.*, *87*, 10,159–10,168, 1982.

Smith, W. L., Iterative solution of the radiative transfer equation for the temperature and absorbing gas profile of an atmosphere, *Applied Optics*, *9*, 1993–1999, 1970.

Toon, O. B., J. B. Pollack, and C. Sagan, Physical properties of the particles composing the Martian dust storm of 1971–1972, *Icarus*, *30*, 663–696, 1977.

Wiscombe, W. J., Improved Mie scattering algorithms, *Applied Optics*, *19*, 1505–1509, 1980.

Wu, S. S. C., Photogrammetric portrayal of Mars topography, *J. Geophys. Res.*, *84*, 7955–7959, 1979.

Zurek, R. W., Martian great dust storms: An update, *Icarus*, *50*, 288–310, 1982.

Zurek, R. W., J. R. Barnes, R. M. Haberle, J. B. Pollack, J. E. Tillman, and C. B. Leovy, Dynamics of the Atmosphere of Mars , In *Mars* , C. Snyder, H. H. Kieffer, and B. M. Jakosky (ed.), University of Arizona Press, In Press, 1992.

PAPER II

Diagnostic Calculations of the Circulation in the Martian Atmosphere

Diagnostic Calculations of the Circulation in the Martian Atmosphere

Michelle Santee

Division of Geological and Planetary Sciences

California Institute of Technology

Pasadena, California 91125

and

David Crisp

Earth and Space Sciences Division

Jet Propulsion Laboratory, California Institute of Technology

Pasadena, California 91109

To be Submitted to *J. Geophys. Res.*

Abstract

The circulation of the Martian atmosphere during late southern summer is calculated diagnostically from the observed atmospheric temperature distribution. We use global maps of temperature and dust optical depth ($\sim 0 - 60$ km) retrieved from a subset of the Mariner 9 IRIS thermal emission spectra spanning $L_S = 343° - 348°$ [*Santee and Crisp*, 1992]. This thermal structure is characterized by a reversed meridional temperature gradient (temperatures increasing poleward) at altitudes above about 40 km, and temperatures that decrease from equator to pole at lower altitudes. Zonal–mean zonal winds are derived from the zonally–averaged temperatures assuming gradient wind balance and zero surface zonal wind. Both hemispheres have intense mid–latitude westerly jets (with velocities of 80–90 m/s near 50 km); in the southern tropics the winds are easterly and strong, with velocities of 100 m/s near 50 km. The north–south atmospheric transport includes contributions from the zonal–mean meridional circulation and large–scale waves. Their net effect can be approximated by the diabatic circulation, which is that circulation needed to maintain the observed temperature distribution (warm winter pole, cool tropics) in the presence of the radiative forcing. A radiative transfer model [*Crisp*, 1990] which accounts for absorption, emission and multiple scattering by particles and non–grey gases is used to compute the solar heating and thermal cooling rates from diurnal averages of the retrieved IRIS temperature and dust distributions. At pressures below 4 mbar, there are large net heating rates (up to 8 K/day) in the equatorial region and large net cooling rates (up to 20 K/day) in the polar regions. These net heating rates are used in a diagnostic stream function model which solves for the meridional and vertical components of the diabatic circulation simultaneously. We find a two–cell circulation, with upwelling over the equator ($\sim$ 1.5 cm/s), poleward motion in both hemispheres ($\sim$ 2 m/s), and subsidence over the poles (1–2 cm/s). This circulation is sufficiently vigorous that the

meridional transport time scale is $\sim$ 13 days. Vertical transport is primarily advective in nature, except in the high–altitude winter polar regions, where diffusive processes dominate. Water vapor desorbed from the low–latitude regolith during late northern winter/early northern spring may be transported upward by the ascending branch of this circulation, where it would be transported poleward by the high–altitude meridional winds. This process could provide a high–altitude source of water vapor for the polar hood.

1. Introduction

Atmospheric transport may be a crucial element in the seasonal cycles of carbon dioxide, dust, and water on Mars, but the extent of its contribution remains uncertain. Knowledge of the general circulation is insufficient at the present time to address even certain fundamental issues, such as whether a net transfer of dust or water is taking place between hemispheres. A brief review of the existing data pertaining to the seasonal dust and water cycles is provided below to illustrate this point. Part of the problem is that there have been no direct measurements of wind speed or direction in the region between the surface and approximately the 40 km level. However, as we will discuss in this paper, the atmospheric circulation can be calculated diagnostically from the observed atmospheric temperature distribution.

Most of the studies addressing the transport and deposition of airborne dust have focussed on dust storm conditions [see, *e.g.*, *Haberle et al.*, 1982; *Barnes and Hollingsworth*, 1987; *Zurek and Haberle*, 1988; *Barnes*, 1990a]. Almost every Martian year there are one or two dust storms of planetary, but not necessarily global, scale; more rarely, these storms intensify and expand to the point where they become planet–encircling [*Zurek*, 1982]. The severe dust storm which began three months before the arrival of the Mariner 9 spacecraft at Mars in November, 1971 was one such global event. All of the planetary–scale dust storms that have been observed originated in the southern hemisphere during southern spring and summer [*Zurek*, 1982]. Because dust raised during these storms spreads non–uniformly over large distances, the seasonality of the largest dust storms implies that there may be a net transfer of dust between regions on the planet. Spacecraft observations of variations in regional albedo features have provided direct evidence of dust redistribution over the surface of Mars. Based on albedo measurements from the Viking infrared thermal mapper (IRTM), *Christensen* [1988] concludes that, during the current epoch, there is a net transport of dust from

the south to the north. This conclusion is consistent with the results of *Haberle et al.* [1982], in which a numerical circulation model is used to simulate the response of the Martian atmosphere to global dust storms.

No equivalent great dust storms have been observed to occur near northern summer solstice to reverse the south–to–north cross–equatorial trend. However, there are other, less dramatic, dust transport mechanisms, affecting smaller quantities of dust, which may operate persistently enough to counteract the effects of the great dust storms. Frequent localized dust storms have been observed in both Mariner 9 and Viking data [*Leovy et al.*, 1972; *Peterfreund and Kieffer*, 1979] at a wide variety of seasons and latitudes. In addition, dust devils have been observed in Viking Lander meteorology data [*Ryan and Lucich*, 1983] and Viking Orbiter images [*Thomas and Gierasch*, 1985]. Dust entrained by local dust storms and dust devils would be transported away by the general circulation patterns. Still unanswered are the questions of whether the south–to–north transport due to great dust storms is compensated or augmented by these processes, and whether there is actually net accumulation of dust in certain regions of the planet. A quantitative understanding of this issue requires not only a knowledge of the spatial distribution of the dust, but also an accurate picture of the meridional circulation of the Martian atmosphere.

There is a similar ambiguity in the role of atmospheric transport in the seasonal water cycle. Considerable seasonal and spatial variability in the total column abundance of water vapor has been observed in both spacecraft and ground–based measurements [*Jakosky*, 1985]. From an analysis of Viking Mars Atmospheric Water Detector (MAWD) data, *Jakosky and Farmer* [1982] report that the northern hemisphere contains up to twice as much water vapor as the southern hemisphere, with the water abundance decreasing essentially monotonically from north to south. Because the south polar cap retains a CO_2 frost covering during the summer (at least during

the Viking year [*Kieffer*, 1979]), it acts as a cold trap for removing water from the atmosphere throughout the year. In contrast, the north polar cap acts as a sink for water only during winter. In the summer its CO_2 frost sublimes, revealing a water ice cap which serves as a source for water. *Jakosky and Farmer* [1982] argue that the strong latitudinal gradient of water and the asymmetry in the seasonal behavior of the polar caps implies a net annual transport of water southward, with a net loss of water from the north cap and a net gain onto the south cap.

Several authors [*Pollack et al.*, 1977; *Farmer and Doms*, 1979; *Barnes and Hollingsworth*, 1987; *Barnes*, 1990a] have also suggested the possibility of transport of water northward, particularly during the dust storms, which might balance or exceed the probable southward transport. Alternatively, *James* [1985; 1990] has proposed that the CO_2 cycle can act as a "pump" to maintain the latitudinal gradient of water vapor as a steady–state condition without resulting in a net transfer of water to the south. This is because Mars' large orbital eccentricity leads to an asymmetry in hemispheric solar insolation, which in turn leads to an asymmetry in the mass flux of CO_2 between the polar caps and an asymmetry in the advection of water vapor. In spite of these modeling efforts, it is clear that the magnitude, and even the direction, of the net annual interhemispheric transfer of water in the Martian atmosphere remains unknown.

The interplay between atmospheric transport and the exchange of water between the atmosphere and various seasonal reservoirs is also a key issue governing atmospheric water vapor. *Haberle and Jakosky* [1990] found an increase in southern hemisphere water vapor abundance just after the beginning of northern summer, along with a corresponding decrease in northern hemisphere water. Because there are no known sources for atmospheric water vapor in the south at this season, this provides further evidence of cross–equatorial transport of water vapor from the north

during northern summer. However, their modeling work indicates that not only is it unlikely that all of the observed water vapor in the northern hemisphere originated in the residual polar cap, but even if it did, the modeled high–latitude summertime circulation lacks the intensity and scale to transport it to the lower latitudes. They conclude that most of the water that sublimes from the residual cap during summer remains in the polar environment, and therefore additional sources for water must exist. There are other indicators of this as well [see, *e.g.*, *Jakosky*, 1983a; 1983b]; for instance, the first increase in atmospheric water vapor abundance in northern spring occurred at 20° N and not at the edge of the receding seasonal polar cap. This suggests that at least the initial part of the seasonal water vapor increase must be supplied by the low–latitude regolith [*Jakosky and Farmer*, 1982]. In order to evaluate the efficacy of atmospheric interactions with the regolith and other potential reservoirs, an understanding of the atmospheric transport of water over a range of altitudes during a Martian year is essential.

Unfortunately, there have been few direct measurements of wind speed or direction in the Martian atmosphere, and none on a global scale. The only *in–situ* wind measurements were made by the meteorology experiments onboard the Viking Landers [*e.g.*, *Hess et al.*, 1977]. They acquired detailed temporal records of wind speed and direction, but only for two locations on the planet and only at a fixed elevation ($\sim$ 1.6 m) above the surface. Several authors [*e.g.*, *Ryan et al.*, 1978; *Ryan and Henry*, 1979; *Tillman et al.*, 1979; *Barnes* 1980; 1981] have analyzed these data to provide constraints on larger–scale processes and the general circulation.

In the absence of other direct wind measurements, exhaustive compilations of cloud structures, including their spatial and temporal variations, have been undertaken for both Mariner 9 and Viking Orbiter images [*Leovy et al.*, 1972; *Briggs and Leovy*, 1974; *Briggs et al.*, 1977; *French et al.*, 1981; *Kahn*, 1983]. Although studies

of cloud motions and morphology have yielded wind directions, and in some cases, estimates of wind speeds, they suffer from a lack of systematic global coverage. Because regional winds may arise from a variety of factors, including the presence of slopes or strong horizontal surface temperature variations (*e.g.*, at the edges of the polar caps or in regions of large albedo or thermal inertia contrasts), it is not clear how representative these observed winds are of the mean flow.

Recently, *Lellouch et al.* [1991] have reported the first measurements of winds in the middle atmosphere of Mars (40–70 km), obtained from Doppler shifts of the $J = 2 - 1$ ^{12}CO rotational line. Taken during the 1988 opposition, these observations provide extensive coverage of the southern hemisphere near southern summer solstice ($L_S = 279°$). Their results are consistent with the thermal structure of the Martian middle atmosphere derived from infrared heterodyne spectroscopy [*Deming et al.*, 1986; *Rothermel et al.*, 1988]. They are also in general agreement with the modeling results of *Barnes* [1990b; 1991] and *Pollack et al.* [1990]. However, the *Lellouch et al.* measurements cannot be used to infer wind fields below the 40 km level.

Winds in the intermediate regime between the surface and the upper portion of the middle atmosphere can be determined indirectly from the observed atmospheric temperature distribution. The thermal structure of the Martian atmosphere has been investigated by remote–sensing instruments on several different spacecraft; however, the best existing data for studying the vertical temperature distribution on a global scale are thermal emission spectra recorded by the Mariner 9 infrared interferometer spectrometer (IRIS). Using a new technique for the simultaneous retrieval of atmospheric temperatures and airborne dust abundances from these thermal emission spectra, we have derived a comprehensive picture of the thermal structure and dust loading of the Martian atmosphere in a relatively clear period during late southern summer [*Santee and Crisp*, 1992; hereinafter Paper I]. In Paper I we examined a

subset of the IRIS data consisting of approximately 2400 spectra in a 12–day period extending from $L_S = 343° - 348°$. The retrieval algorithm is an iterative procedure which was performed on each spectrum, and global maps of temperature and dust optical depth as functions of latitude ($\pm 90°$), altitude ($\sim 0 - 60$ km), and Mars local time were constructed from the individual profiles.

One of the principal conclusions from Paper I is that both dayside and nightside atmospheric temperatures at altitudes above about 40 km are warmer over the winter (north) polar regions than over the equator or the summer (south) polar regions. These anomalous temperatures are consistent with the thermal structure in the middle atmosphere observed by *Deming et al.* [1986] and *Rothermel et al.* [1988], and they indicate that the atmosphere is not in radiative equilibrium. A similarly–reversed temperature gradient is present in the terrestrial atmosphere and is known to be a response to the meridional circulation, which produces enough adiabatic heating (or cooling) to overcome the radiative forcing [*Leovy*, 1964].

In the present paper we describe methods whereby the atmospheric circulation can be diagnosed from observed temperatures. We begin in Section 2.1 with a brief presentation of the primitive equations, which describe the large–scale circulation of the atmosphere. Equations for the zonal–mean flow are developed in Section 2.2. The calculation of zonal–mean zonal winds, which are derived from the observed meridional gradients of the zonally–averaged temperatures using the gradient thermal wind equation and assuming zero surface zonal wind, is examined in Section 2.3.

Both the zonal–mean meridional circulation and large–scale waves contribute to the north–south atmospheric transport. *Dunkerton* [1978] showed that the net effect of these processes can be approximated by the diabatic circulation, which is that circulation needed to maintain the observed temperature distribution (warm winter pole, cool tropics) in the presence of the radiative drive. These concepts are

reviewed in Section 2.4. In Section 2.5 we present a stream function model which solves for the meridional and vertical components of the diabatic circulation simultaneously. This model requires values for the net radiative heating rates. We use a radiative–convective–equilibrium model [*Crisp*, 1990] to compute solar and thermal fluxes and radiative heating and cooling rates from diurnal averages of the retrieved temperature and dust distributions. This model, which accounts for absorption, emission, and multiple scattering by particles and non–grey gases, is briefly described in Section 3.

In Section 4, the results of the circulation and heating rate calculations are discussed. Although similar calculations of the zonal–mean zonal wind have been reported previously [*Conrath*, 1981; *Leovy*, 1982; *Michelangeli et al.*, 1987], they were based on Mariner 9 meridional plane cross–sections of temperature which were not global in coverage. In addition, although *Crisp* [1990] computed global–annual–average solar heating rate profiles for a dust–free model Martian atmosphere, our results represent the first global zonal–mean solar heating, thermal cooling, and net radiative heating rates ever calculated from temperature observations of the Martian atmosphere. Finally, although numerical simulations of the Martian atmosphere have been conducted using a full three–dimensional general circulation model based on the primitive equations [*Pollack et al.*, 1981; *Pollack et al.*, 1990], and a two–dimensional coupled chemical, radiative, and dynamical model based on the transformed Eulerian–mean equations [*Moreau et al.*, 1991], our results constitute the first estimation of the diabatic circulation of the Martian atmosphere from actual temperature observations.

2. Diagnostic Calculations of the Atmospheric Circulation

2.1 The Primitive Equations

The large–scale circulation of the atmosphere is governed by the Navier–Stokes equation of motion for a gas in a rotating frame. Scale analysis, involving an inves-

tigation of the relative orders of magnitude of the various terms in the horizontal momentum equations, indicates that the Coriolis force associated with the horizontal component of the planet's rotation vector can be neglected [*Holton*, 1979]. In addition, the vertical momentum equation can be replaced by the hydrostatic approximation, and the distance from any point in the atmosphere to the center of the planet can be replaced by a mean radius. These simplifications lead to a set of equations known as the primitive equations.

In spherical, log–pressure coordinates, using notation similar to that of *Andrews, Holton, and Leovy* [1987], the primitive equations take the form:

$$\frac{\partial u}{\partial t} + \frac{u}{a\cos\phi}\frac{\partial u}{\partial \lambda} + \frac{v}{a}\frac{\partial u}{\partial \phi} + w\frac{\partial u}{\partial z} - \frac{uv\tan\phi}{a} - fv + \frac{1}{a\cos\phi}\frac{\partial \Phi}{\partial \lambda} = X \qquad (1.1)$$

$$\frac{\partial v}{\partial t} + \frac{u}{a\cos\phi}\frac{\partial v}{\partial \lambda} + \frac{v}{a}\frac{\partial v}{\partial \phi} + w\frac{\partial v}{\partial z} + \frac{u^2\tan\phi}{a} + fu + \frac{1}{a}\frac{\partial \Phi}{\partial \phi} = Y \qquad (1.2)$$

$$\frac{\partial \Phi}{\partial z} = \frac{RT}{H} \qquad (1.3)$$

$$\frac{1}{a\cos\phi}\frac{\partial u}{\partial \lambda} + \frac{1}{a\cos\phi}\frac{\partial}{\partial \phi}\Big(v\cos\phi\Big) + \frac{1}{\rho}\frac{\partial}{\partial z}\Big(\rho w\Big) = \frac{\partial \rho}{\partial t} \qquad (1.4)$$

$$\frac{\partial T}{\partial t} + \frac{u}{a\cos\phi}\frac{\partial T}{\partial \lambda} + \frac{v}{a}\frac{\partial T}{\partial \phi} + w\left[\frac{\partial T}{\partial z} + \frac{g}{c_p}\right] = Q\,. \qquad (1.5)$$

The first two equations express momentum balance in the zonal and meridional directions, respectively. t is time, u, v, and w are the velocity components in the zonal, meridional, and vertical directions, and the horizontal coordinates are λ for longitude and ϕ for latitude. The vertical coordinate is not the geometric height but rather the log–pressure altitude:

$$z = -H\,\ln(p/p_s) \qquad (2)$$

where p is the atmospheric pressure and the subscript "s" denotes a value at the surface. H is the mean atmospheric scale height ($H = RT/g$) calculated by assuming a constant reference temperature for T and a mean gas constant, R. g is the

gravitational acceleration (assumed constant). This choice of vertical coordinate is advantageous because it allows the primitive equations to assume simpler forms. Of the remaining terms in equations (1.1) and (1.2), a is the mean radius of the planet, and X and Y are horizontal components of friction or other unspecified nonconservative forces. The Coriolis parameter, which represents the vertical component of the planet's rotation vector, is given by:

$$f = 2\,\Omega \sin \phi \tag{3}$$

where

$$\Omega = \frac{2\pi}{\text{length of sidereal day}} \tag{4}$$

is the planet's angular velocity. Because the length of the Martian day is 24.6 hr, the rotation rate is $\Omega = 7.1 \times 10^{-5}\,\mathrm{s}^{-1}$, and the Coriolis forces are as important on Mars as they are on Earth.

The third equation represents hydrostatic balance in the vertical. It is written in terms of the geopotential, Φ, which is defined as the work required to raise a unit mass from the surface to a geometric height, z^*:

$$\Phi = \int_0^{z^*} g\,dz\,. \tag{5}$$

The form of equation (1.3) arises from combining equation (5) with the hydrostatic equation, $\partial p/\partial z^* = -\rho g$, and the ideal gas law, $p = \rho RT$, where ρ is the atmospheric density.

The fourth equation, the continuity equation, expresses the conservation of mass. The source and sink terms, represented by $\partial \rho/\partial t$, are included in this equation because of the condensation and sublimation of a significant fraction of the CO_2 atmosphere at high latitudes over the course of a year. One of the unique aspects of Martian meteorology is the fact that approximately 25 percent of the atmospheric

mass is cycled into and out of the seasonal polar caps [*Hess et al.*, 1979]. These terms are most important during the fall, when the cap is growing, and during the spring, when it is receding. A corresponding large–amplitude seasonal oscillation in the daily–average atmospheric pressure was observed at both Viking Lander sites [*Hess et al.*, 1979]. There was a deep pressure minimum near $L_S = 150°$, signalling maximum CO_2 accumulation onto the south polar cap at the end of southern winter. A secondary, much shallower minimum occurred near $L_S = 350°$, signalling maximum CO_2 accumulation onto the north polar cap at the end of northern winter. The daily–average pressure at both sites remained relatively constant from $L_S = 340° - 360°$, suggesting that the north polar cap was stable during this period (at least during the Viking year). It is therefore probable that the north polar cap had not begun to retreat at the time this data subset was recorded ($L_S = 343° - 348°$). In addition, based on a systematic review of wind direction information obtained from a variety of indicators, *Kahn* [1983] found that recession of the polar cap in the north produces much smaller mass fluxes than in the south, and hence has very little influence on wind directions during early northern spring. He concluded that during the late winter and early spring seasons in the north, wind directions are determined by the temperature field, not cap flows. *Pollack et al.* [1990] used a three–dimensional general circulation model of the Martian atmosphere to conduct numerical simulations of polar processes for different seasons and dust loadings. Simulations at $L_S = 342°$ (with a visible dust optical depth of $\tau = 1$) indicate that the importance of heat transport by the condensation flow (mass flow toward or away from polar regions where CO_2 is condensing or subliming) is relatively small at this season, except at the very center of the cap. Consequently, we neglect the $\partial\rho/\partial t$ term for these calculations.

Finally, equation (1.5) is the thermodynamic energy equation. c_p is the specific heat at constant pressure, which for a pure CO_2 atmosphere can be parameterized by

[*Touloukian and Makita*, 1970]:

$$c_p(T) = 443.15 + 1.688\,T - 1.269 \times 10^{-3}\,T^2 + 3.470 \times 10^{-7}\,T^3\,. \qquad (6)$$

The term g/c_p is the adiabatic lapse rate. The thermodynamic energy equation relates the time rate of change of the temperature following the fluid motion to the diabatic heating, Q. The term "diabatic" refers to a change in temperature involving the actual addition or removal of heat (as opposed to adiabatic heating). Diabatic processes include absorption of solar radiation, absorption and emission of infrared radiation, and latent heat release. Also, mixing of different air masses within a convective layer leads to diabatic heating through internal molecular processes of the system such as conduction, friction, and diffusion [*Hantel and Baader*, 1978; *Wallace and Hobbs*, 1977]. However, for most meteorological applications the molecular contributions are neglected. We also neglect the latent heating component because temperatures in our data subset rarely approach the CO_2 condensation temperature. Therefore, the diabatic heating reduces to the net radiative heating.

2.2 The Eulerian–Mean Equations

The atmospheric circulation can be mathematically decomposed into a zonally symmetric flow plus disturbances (usually called "eddies" or "waves") superimposed on it. Any field variable can be written as the sum of the zonal mean part, denoted by an overbar, and the deviation from the mean, denoted by a prime. Using the zonal wind, u, for illustration,

$$u(\lambda,\phi,z,t) = \overline{u}(\phi,z,t) + u'(\lambda,\phi,z,t)\,. \qquad (7)$$

The zonal averaging operator is defined by:

$$\overline{u}(\phi,z,t) = \frac{1}{2\pi}\int_0^{2\pi} u(\lambda,\phi,z,t)\,d\lambda\,. \qquad (8)$$

This average is an Eulerian mean, because it is taken at fixed values of the coordinates ϕ, z, and t. (A Lagrangian mean, in contrast, would involve taking averages following fluid parcels which are moving with the flow). Expanding all the field variables according to equation (7) and then applying the zonal averaging operator of equation (8) leads to a reformulation of the primitive equations in which the zonal circulation and the eddy terms have been separated:

$$\frac{\partial \overline{u}}{\partial t} + \frac{\overline{v}}{a}\frac{\partial \overline{u}}{\partial \phi} + \overline{w}\frac{\partial \overline{u}}{\partial z} - \frac{\overline{uv}\tan\phi}{a} - f\overline{v} - \overline{X} = -\frac{1}{a\cos^2\phi}\frac{\partial}{\partial \phi}\left(\overline{v'u'}\cos^2\phi\right) - \frac{1}{\rho}\frac{\partial}{\partial z}\left(\rho\,\overline{w'u'}\right) \quad (9.1)$$

$$\frac{\partial \overline{v}}{\partial t} + \frac{\overline{v}}{a}\frac{\partial \overline{v}}{\partial \phi} + \overline{w}\frac{\partial \overline{v}}{\partial z} + \frac{\overline{u}^2\tan\phi}{a} + f\overline{u} + \frac{1}{a}\frac{\partial \overline{\Phi}}{\partial \phi} - \overline{Y} = -\frac{1}{a\cos\phi}\frac{\partial}{\partial \phi}\left(\overline{v'^2}\cos\phi\right) - \frac{1}{\rho}\frac{\partial}{\partial z}\left(\rho\,\overline{w'v'}\right) - \frac{\overline{u'^2}\tan\phi}{a} \quad (9.2)$$

$$\frac{\partial \overline{\Phi}}{\partial z} - \frac{R\overline{T}}{H} = 0 \quad (9.3)$$

$$\frac{1}{a\cos\phi}\frac{\partial}{\partial \phi}\left(\overline{v}\cos\phi\right) + \frac{1}{\rho}\frac{\partial}{\partial z}\left(\rho\,\overline{w}\right) = 0 \quad (9.4)$$

$$\frac{\partial \overline{T}}{\partial t} + \frac{\overline{v}}{a}\frac{\partial \overline{T}}{\partial \phi} + \overline{w}\left[\frac{\partial \overline{T}}{\partial z} + \frac{g}{c_p}\right] - \overline{Q} = -\frac{1}{a\cos\phi}\frac{\partial}{\partial \phi}\left(\overline{v'T'}\cos\phi\right) - \frac{1}{\rho}\frac{\partial}{\partial z}\left(\rho\,\overline{w'T'}\right). \quad (9.5)$$

The terms "$\overline{v'u'}$" and "$\overline{v'T'}$" represent the "eddy momentum flux" and "eddy heat flux," respectively. The eddy flux terms, which involve zonal averages of the products of perturbations, have been segregated on the right–hand side of all of these equations.

2.3 The Gradient Thermal Winds

The zonal–mean zonal winds can be estimated directly from the observed thermal structure of the atmosphere. Considering a steady flow which is purely zonal and unforced (*i.e.*, frictionless), the meridional momentum equation (equation (9.2))

reduces to:

$$\frac{\overline{u}^2 \tan\phi}{a} + f\overline{u} = -\frac{1}{a}\frac{\partial\overline{\Phi}}{\partial\phi}. \tag{10}$$

Combining this equation with the hydrostatic equation (equation (9.3)) and cross-differentiating to eliminate the Φ term leads to:

$$\left[f + \frac{2\overline{u}\tan\phi}{a}\right]\frac{\partial\overline{u}}{\partial z} = -\frac{R}{aH}\frac{\partial\overline{T}}{\partial\phi}. \tag{11.1}$$

Equation (11.1) is called the "gradient thermal wind" equation, and it specifies the vertical wind shear due to meridional temperature gradients. The flow described by this equation is in a three-way balance between the Coriolis force, the centrifugal force, and the horizontal pressure gradient force. If the centrifugal acceleration term is small compared to the Coriolis term, it can be dropped from equation (11.1) to yield the "geostrophic thermal wind" equation:

$$f\frac{\partial\overline{u}}{\partial z} = -\frac{R}{aH}\frac{\partial\overline{T}}{\partial\phi}. \tag{11.2}$$

Equation (11.2) may not always be valid for Mars. Because the gradient wind equation accounts for the centrifugal force due to the curvature of air parcel trajectories, as well as the Coriolis force, it provides a more accurate estimate of the actual wind than does the geostrophic thermal wind equation. Both equations highlight the fact that the wind field is strongly coupled to the atmospheric temperature distribution.

To solve equation (11.1) for the zonal-mean zonal wind $\overline{u}$, the derivatives with respect to ϕ and z are approximated by finite differences [see, *e.g.*, *Haltiner and Williams*, 1980]. We divide the ϕ, z space into a grid of $M \times N$ points, which are evenly-spaced in their respective directions, so that any point on the grid is uniquely identified by the indices (m,n). A portion of the grid space is shown in Figure 1. Using centered finite difference formulas, derivatives of any variable, say ψ, at the point (m,n) can be expressed in terms of its values at the surrounding points. For completeness, the formulas for first and second derivatives are included:

$$\left(\frac{\partial\psi}{\partial\phi}\right)_{m,n} = \frac{\psi_{m+1,n} - \psi_{m-1,n}}{\phi_{m+1} - \phi_{m-1}} \tag{12.1}$$

$$\left(\frac{\partial^2\psi}{\partial\phi^2}\right)_{m,n} = \frac{\psi_{m+1,n} - 2\psi_{m,n} + \psi_{m-1,n}}{0.25(\phi_{m+1} - \phi_{m-1})^2} \tag{12.2}$$

$$\left(\frac{\partial^2\psi}{\partial z\partial\phi}\right)_{m,n} = \frac{\psi_{m+1,n+1} - \psi_{m-1,n+1} - \psi_{m+1,n-1} + \psi_{m-1,n-1}}{(\phi_{m+1} - \phi_{m-1})(z_{n+1} - z_{n-1})}\,. \tag{12.3}$$

However, because the quantity we are solving for appears in both the $2\overline{u}\tan\phi/a$ and $\partial\overline{u}/\partial z$ terms, a forward difference formula is more appropriate for the derivative with respect to z. That is:

$$\left(\frac{\partial\psi}{\partial z}\right)_{m,n} = \frac{\psi_{m,n+1} - \psi_{m,n}}{z_{n+1} - z_n}\,. \tag{12.4}$$

Applying the finite difference formulas to equation (11.1) and grouping like terms together yields a quadratic equation for $u_{m,n}$:

$$\left[\frac{2/a\,\tan\phi_m}{z_{n+1} - z_n}\right]\overline{u}^2_{m,n} - \left[\frac{2/a\,\tan\phi_m\,\overline{u}_{m,n+1} - f_m}{z_{n+1} - z_n}\right]\overline{u}_{m,n} - \left[\frac{R}{aH}\,\frac{\overline{T}_{m+1,n} - \overline{T}_{m-1,n}}{\phi_{m+1} - \phi_{m-1}} + \frac{f_m\,\overline{u}_{m,n+1}}{z_{n+1} - z_n}\right] = 0\,. \tag{13}$$

Because the solution for $\overline{u}_{m,n}$ involves the value of $\overline{u}_{m,n+1}$, the winds at some reference level must be known. Typically, u is assumed to be zero at the surface. Evidence that surface winds on Mars are generally light (less than 10 m/s) comes from the meteorology experiments onboard the Viking Landers [*Hess et al.*, 1977; *Ryan et al.*, 1978; *Ryan and Henry*, 1979; *Barnes*, 1980; 1981] and from constraints imposed by observations of resonant gravity waves in the winter polar region (see *Briggs and Leovy* [1974]).

There are certain circumstances under which the surface winds are not negligible. Viking Lander observations revealed that surface winds rose steadily with the onset of the global dust storms, with gusts reaching 30 m/s [*Ryan and Henry*, 1979]. Numerical simulations of global dust storms have predicted that (up to a point) higher

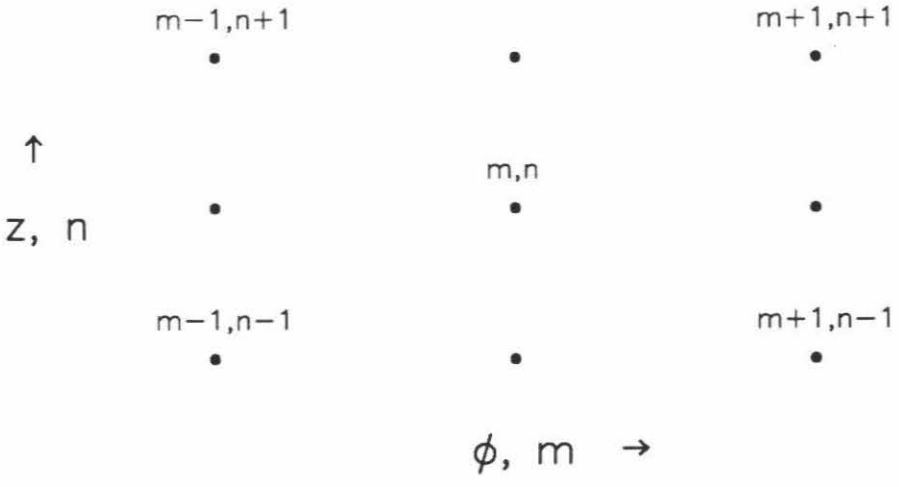

Figure 1. Grid space for finite differences.

dust opacities are accompanied by stronger surface winds [*Haberle et al.*, 1982]. Other modeling studies [*Haberle et al.*, 1979] have indicated that the magnitude of the surface wind is substantially enhanced (up to 30 m/s) when the condensation rate onto, or the sublimation rate from, the seasonal polar caps is at a maximum. Because this data subset represents a period well after the global dust storm had cleared (see Paper I), and because the polar cap at this season is relatively stable (see Section 2.1), we can assume negligible surface winds for the purposes of calculating the vertical wind shear.

2.4 The Transformed Eulerian–Mean Equations

A brief summary of the earliest attempts to model terrestrial middle atmospheric motions will help to elucidate why the Eulerian–mean equations (equation (9)) proved unsuitable for estimating mass transport. The evolution in the understanding of wave–mean flow interactions has been reviewed in depth by *Dunkerton* [1978], *Dunkerton* [1980], *Hsu* [1980], *Matsuno* [1980], and *Mahlman* [1984], among others. *Murgatroyd and Singleton* [1961] were the first to attempt to model the general circulation of the terrestrial middle atmosphere. They diagnosed the mean meridional circulation by assuming that adiabatic heating by the mean vertical motion exactly balanced the imposed net radiative heating; that is, they assumed that the eddy heating terms on the right hand side of equation (9.5) were negligible. Their resulting motion field essentially matched the Brewer–Dobson circulation that had earlier been inferred from the distributions of water vapor and ozone, with rising motions at equatorial latitudes and sinking near the poles.

Later, as observational data became available, *Vincent* [1968] was able to conduct a more extensive analysis. He included eddy heat and momentum fluxes in calculations of the mean meridional circulation and derived a substantially different

circulation. He found that the circulation consisted of two cells, one of which was a thermally–indirect Ferrel cell which involved rising motion over the winter pole and descending motion in the midlatitudes. An apparent paradox was created because, although the distributions of trace substances in the stratosphere supported the existence of the Brewer–Dobson circulation, diagnostic calculations of the Eulerian–mean meridional circulation revealed flow in the opposite direction. Historically, the Brewer–Dobson model fell out of favor after the importance of the eddy transports of heat and momentum was demonstrated.

The splitting of the flow into eddy fluxes and a mean meridional circulation, as in equation (9), is an artificial distinction imposed by the Eulerian–mean approach. In actuality, these two processes are highly interrelated. One of the earliest investigations to use a numerical general circulation model to study quantitatively the relative importance of the mean meridional circulation and the eddies in transporting trace substances in the stratosphere was that of *Hunt and Manabe* [1968]. Their work demonstrated that eddy fluxes due to planetary waves in the stratosphere are almost counteracted by advection due to the mean meridional circulation. This near–cancellation of the two transport processes is a consequence of the fact that stratospheric planetary waves approximately satisfy the "noninteraction" theorem. This theorem, which was established by several authors and generalized by *Andrews and McIntyre* [1976, 1978], states that waves which are linear, steady (not changing with time), and conservative (not being internally forced or dissipated) induce a mean meridional cell which acts to identically cancel the eddy fluxes of the waves themselves. Under these conditions the waves cause no changes to the basic flow. (Of course, there are physical processes which violate the noninteraction theorem; otherwise there would be no large departures of the atmospheric thermal structure from radiative equilibrium.) Because the eddy heat and momentum fluxes tend to force a

compensating mean meridional circulation, in the Eulerian–mean framework the net transport is generally the small residual of two large terms of opposite sign.

The eddy–mean cell compensation suggests that the conventional Eulerian definition of "mean" is not the most suitable one for estimation of the transport circulation. An alternative is the Lagrangian mean, which, instead of taking a simple zonal average along a latitude circle, involves averaging with respect to a curved material tube consisting of a set of fluid parcels [*Hsu*, 1980; *Matsuno*, 1980]. In the absence of waves, the material tube coincides with a latitude circle; under the influence of waves, it is distorted into a wavy shape. The motion of the center of mass of the tube defines the Lagrangian–mean motion. The Lagrangian–mean and Eulerian–mean circulations are quite distinct in general and may, in fact, be of opposite sign. However, net mass transport is achieved entirely by the Lagrangian–mean flow [*Dunkerton*, 1978]. *Dunkerton* rehabilitated the Brewer–Dobson cell by arguing that, because it was derived from a consideration of tracer transport, it should be viewed as a mass circulation, and should therefore be interpreted in a Lagrangian–mean, not an Eulerian–mean, sense. Thus the existence of the Brewer–Dobson circulation is not in conflict with the two–cell Eulerian–mean meridional circulation.

Although conceptually Lagrangian means are more appropriate for transport calculations, in practice the direct application of the Lagrangian–mean formalism to atmospheric data encounters serious technical difficulties. Eulerian quantities are much easier to calculate. An improvement over the traditional Eulerian formulation was suggested by *Andrews and McIntyre* [1976]. They introduced a "residual" mean meridional circulation, $(\overline{v}^*, \overline{w}^*)$, defined through the transformation:

$$\overline{v}^* \equiv \overline{v} - \frac{1}{\rho}\frac{\partial}{\partial z}\left(\frac{\rho\,\overline{v'T'}}{\frac{\partial \overline{T}}{\partial z} + \frac{g}{c_p}}\right) \tag{14.1}$$

$$\overline{w}^* \equiv \overline{w} + \frac{1}{a\cos\phi}\frac{\partial}{\partial \phi}\left(\frac{\overline{v'T'}\cos\phi}{\frac{\partial \overline{T}}{\partial z} + \frac{g}{c_p}}\right). \tag{14.2}$$

After using these definitions to substitute in for $\overline{v}$ and $\overline{w}$ in equation (9) and performing many algebraic manipulations, a set of Transformed Eulerian–Mean (TEM) equations is obtained:

$$\frac{\partial \overline{u}}{\partial t} + \frac{\overline{v}^*}{a\cos\phi}\frac{\partial}{\partial \phi}\left(\overline{u}\cos\phi\right) - f\overline{v}^* + \overline{w}^*\frac{\partial \overline{u}}{\partial z} - \overline{X} = \frac{1}{\rho a\cos\phi}\nabla\cdot\mathcal{F} \tag{15.1}$$

$$\frac{\overline{u}^2\tan\phi}{a} + f\overline{u} + \frac{1}{a}\frac{\partial \overline{\Phi}}{\partial \phi} = \mathcal{G} \tag{15.2}$$

$$\frac{\partial \overline{\Phi}}{\partial z} - \frac{R\overline{T}}{H} = 0 \tag{15.3}$$

$$\frac{1}{a\cos\phi}\frac{\partial}{\partial \phi}\left(\overline{v}^*\cos\phi\right) + \frac{1}{\rho}\frac{\partial}{\partial z}\left(\rho\overline{w}^*\right) = 0 \tag{15.4}$$

$$\frac{\partial \overline{T}}{\partial t} + \frac{\overline{v}^*}{a}\frac{\partial \overline{T}}{\partial \phi} + \overline{w}^*\left[\frac{\partial \overline{T}}{\partial z} + \frac{g}{c_p}\right] - \overline{Q} = -\frac{1}{\rho}\frac{\partial}{\partial z}\left[\frac{\rho\,\overline{v'T'}\,\frac{\partial \overline{T}}{\partial \phi}}{a\left(\frac{\partial \overline{T}}{\partial z} + \frac{g}{c_p}\right)} + \rho\,\overline{w'T'}\right] . \tag{15.5}$$

The vector $\mathcal{F}$ is called the Eliassen–Palm (EP) flux, and $\mathcal{G}$ represents all the terms that disrupt the gradient–wind balance between $\overline{u}$ and $\overline{\Phi}$.

In the transformed mean, the meridional circulation arising from eddy heat transport is removed from the Eulerian circulation. That is, $\overline{w}^*$ represents the component of the Eulerian mean vertical velocity whose adiabatic cooling is not exactly cancelled by the horizontal eddy heat flux, and it is therefore the part of the mean circulation which is relevant for mass transport. One of the principal advantages to the TEM equations is that to solve for the net transport it is no longer necessary to subtract two large effects; the problem has been formulated directly in terms of the remainder. A second advantage is that the residual mean circulation provides a description of atmospheric motions that is close to the actual behavior of fluid parcels. *Dunkerton* [1978] has shown that, for linear, steady, and conservative waves, $\overline{w}^* = \overline{w}^L$, where $\overline{w}^L$ is the Lagrangian–mean vertical velocity. It must be emphasized that in the presence of wave transience or damping the residual circulation and the Lagrangian–mean (transport) circulation are not equivalent.

Dunkerton [1978] further argued that, under certain approximations, the residual (hence mass transport) circulation can be inferred solely from the Eulerian–mean net diabatic heating. The resulting $\overline{v}^*$ and $\overline{w}^*$ are called the "diabatic circulation". The main approximation involves the term on the right–hand side of equation (15.5), which is sometimes referred to as the "wave heating". The generalized noninteraction theorem can be used to prove that, for steady, linear, conservative disturbances, the EP flux divergence and the wave heating both vanish [*Andrews and McIntyre*, 1976]. In actuality, because the observed climatological temperature field is far from the radiative equilibrium structure, the EP flux divergence must be non–zero and the waves must be transient, nonlinear, or nonconservative. It is generally believed that the "breaking" of vertically–propagating gravity waves provides the majority of the forcing of a non–zero EP flux divergence in the terrestrial mesosphere [*Holton*, 1983; *Andrews, Holton, and Leovy*, 1987]. *Barnes* [1990b; 1991] has suggested that breaking topographically–forced gravity waves could explain the large deviations from radiative equilibrium recently observed [*Deming et al.*, 1986; *Rothermel et al.*, 1988] in the middle atmosphere of Mars. *Andrews, Holton, and Leovy* [1987] assert that the wave heating term is negligible for quasi–geostrophic motions (in fact, it drops out of the quasi–geostrophic form of the TEM equations) and for gravity waves. On the basis of *Vincent* [1968], *Dunkerton* [1978] assumed that the vertical eddy flux can be neglected. *Hitchman and Leovy* [1986] estimated this term for the terrestrial middle atmosphere from satellite data and found it to be much smaller than the other terms in the thermodynamic energy equation. Similar assumptions have routinely been made by other researchers [for example, *Holton and Wehrbein*, 1980; *Crisp*, 1983; *Solomon et al.*, 1986; *Rosenfield et al.*, 1987; *Gille et al.*, 1987; *Shine*, 1989]. With these precedents, and in the absence of information about the atmosphere of Mars, we will also neglect the wave heating.

The terms in equation (15.5) associated with the meridional velocity ($\overline{v}^*$) and seasonal change ($\partial/\partial t$) are also customarily ignored [*e.g.*, *Dunkerton*, 1978; *Rosenfield et al.*, 1987; *Gille et al.*, 1987]. This leads to a very simplified balance equation:

$$\overline{w}^* \left[\frac{\partial \overline{T}}{\partial z} + \frac{g}{c_p} \right] \approx \overline{Q} \,. \tag{16}$$

Equation (16) states that the net vertical transport is obtainable from a knowledge of the diabatic heating and the static stability alone. Equation (16) is often combined with the continuity equation (equation (15.4)) and used in an iterative procedure to estimate the residual meridional circulation ($\overline{v}^*$, $\overline{w}^*$). Although this strategy provides an adequate first approximation to the diabatic circulation, it is predicated on an inherent inconsistency, and it depends strongly on a proper normalization of the net radiative heating rate to ensure that global mass balance constraints are satisfied (see, *e.g.*, the review in *Shine* [1989]).

2.5 The Stream Function Model

In this paper we adopt an approach that solves for $\overline{v}^*$ and $\overline{w}^*$ simultaneously. The meridional advection term is retained in the thermodynamic energy equation, but the $\partial \overline{T}/\partial t$ term is of little consequence due to the limited seasonal extent (only twelve days) of the data subset analyzed in Paper I. Neglecting the wave–heating term, equation (15.5) then reduces to:

$$\frac{\overline{v}^*}{a} \frac{\partial \overline{T}}{\partial \phi} + \overline{w}^* \left[\frac{\partial \overline{T}}{\partial z} + \frac{g}{c_p} \right] = \overline{Q} \,. \tag{17}$$

This equation is coupled to the continuity equation through the definition of a zonal–mean stream function, ψ. The form of ψ is to some extent arbitrary and was adopted from *Shia et al.* [1989]:

$$\overline{v}^* = -\frac{1}{\cos\phi} e^{\frac{z}{H}} \frac{\partial}{\partial z} \left(e^{-\frac{z}{H}} \psi \right) = \frac{1}{\cos\phi} \left[\frac{\psi}{H} - \frac{\partial \psi}{\partial z} \right] \tag{18.1}$$

$$\overline{w}^* = \frac{1}{a \cos\phi} \frac{\partial \psi}{\partial \phi} \,. \tag{18.2}$$

Substituting these expressions into equation (17) yields:

$$\frac{1}{a\cos\phi}\left[\frac{\psi}{H}-\frac{\partial\psi}{\partial z}\right]\frac{\partial\overline{T}}{\partial\phi}+\frac{1}{a\cos\phi}\left[\frac{\partial\overline{T}}{\partial z}+\frac{g}{c_p}\right]\frac{\partial\psi}{\partial\phi}=\overline{Q}. \tag{19}$$

Straightforward integration of this equation is precluded by numerical instabilities.

Run–Lie Shia [personal communication, 1990] suggested taking the derivative of the entire equation with respect to latitude (ϕ). Applying $\partial/\partial\phi$ to equation (19) and grouping ψ terms together leads to:

$$\begin{aligned}\frac{1}{aH\cos\phi}\left[\frac{\partial^2\overline{T}}{\partial\phi^2}+\tan\phi\frac{\partial\overline{T}}{\partial\phi}\right]\psi-\frac{1}{a\cos\phi}\left[\frac{\partial^2\overline{T}}{\partial\phi^2}+\tan\phi\frac{\partial\overline{T}}{\partial\phi}\right]\frac{\partial\psi}{\partial z}\\+\frac{1}{a\cos\phi}\left[\frac{1}{H}\frac{\partial\overline{T}}{\partial\phi}+\left(\frac{\partial\overline{T}}{\partial z}+\frac{g}{c_p}\right)\tan\phi+\frac{\partial}{\partial\phi}\left(\frac{\partial\overline{T}}{\partial z}+\frac{g}{c_p}\right)\right]\frac{\partial\psi}{\partial\phi}\\+\frac{1}{a\cos\phi}\left(\frac{\partial\overline{T}}{\partial z}+\frac{g}{c_p}\right)\frac{\partial^2\psi}{\partial\phi^2}-\frac{1}{a\cos\phi}\frac{\partial\overline{T}}{\partial\phi}\frac{\partial^2\psi}{\partial z\partial\phi}=\frac{\partial\overline{Q}}{\partial\phi}.\end{aligned} \tag{20}$$

This mathematical "trick" changes the character of the equation and allows it to be integrated numerically. An additional benefit is that in this form of the equation the diabatic heating appears only as a derivative with respect to latitude, eliminating the need for a heating rate correction. For notational simplicity, A, B, C, D, and E are introduced for the coefficients of the ψ terms, and F is used for the right–hand side of equation (20):

$$A\psi+B\frac{\partial\psi}{\partial z}+C\frac{\partial\psi}{\partial\phi}+D\frac{\partial^2\psi}{\partial\phi^2}+E\frac{\partial^2\psi}{\partial z\partial\phi}=F. \tag{21}$$

The simplest approach to solving equation (21) is to use finite differences to approximate the derivatives on a grid of points in ϕ and z (see Section 2.3). The centered finite–difference formulas of equation (12) must be applied to both the ψ terms and their coefficients in equation (21). The coefficients in their expanded finite–difference forms are written as follows:

$$A_{m,n} = \frac{1}{aH\cos\phi_m}\left[\frac{\overline{T}_{m+1,n} - 2\overline{T}_{m,n} + \overline{T}_{m-1,n}}{0.25\left(\phi_{m+1} - \phi_{m-1}\right)^2} + \tan\phi_m\left(\frac{\overline{T}_{m+1,n} - \overline{T}_{m-1,n}}{\phi_{m+1} - \phi_{m-1}}\right)\right] \quad (22.1)$$

$$B_{m,n} = -H\,A_{m,n} \quad (22.2)$$

$$C_{m,n} = \frac{1}{a\cos\phi_m}\left[\frac{1}{H}\frac{\overline{T}_{m+1,n} - \overline{T}_{m-1,n}}{\phi_{m+1} - \phi_{m-1}} + g\left(\frac{c_{p_{m+1,n}}^{-1} - c_{p_{m-1,n}}^{-1}}{\phi_{m+1} - \phi_{m-1}}\right) + \frac{\overline{T}_{m+1,n+1} - \overline{T}_{m-1,n+1} - \overline{T}_{m+1,n-1} + \overline{T}_{m-1,n-1}}{\left(z_{n+1} - z_{n-1}\right)\left(\phi_{m+1} - \phi_{m-1}\right)} + \tan\phi_m\left(\frac{\overline{T}_{m,n+1} - \overline{T}_{m,n-1}}{z_{n+1} - z_{n-1}} + \frac{g}{c_{p_{m,n}}}\right)\right] \quad (22.3)$$

$$D_{m,n} = \frac{1}{a\cos\phi_m}\left[\frac{\overline{T}_{m,n+1} - \overline{T}_{m,n-1}}{z_{n+1} - z_{n-1}} + \frac{g}{c_{p_{m,n}}}\right] \quad (22.4)$$

$$E_{m,n} = -\frac{1}{a\cos\phi_m}\left[\frac{\overline{T}_{m+1,n} - \overline{T}_{m-1,n}}{\phi_{m+1} - \phi_{m-1}}\right] \quad (22.5)$$

$$F_{m,n} = \frac{\overline{Q}_{m+1,n} - \overline{Q}_{m-1,n}}{\phi_{m+1} - \phi_{m-1}}. \quad (22.6)$$

Expanding equation (21) according to equation (12) leads to:

$$A\,\psi_{m,n} + B\left[\frac{\psi_{m,n+1} - \psi_{m,n-1}}{z_{n+1} - z_{n-1}}\right] + C\left[\frac{\psi_{m+1,n} - \psi_{m-1,n}}{\phi_{m+1} - \phi_{m-1}}\right] + D\left[\frac{\psi_{m+1,n} - 2\psi_{m,n} + \psi_{m-1,n}}{0.25(\phi_{m+1} - \phi_{m-1})^2}\right] + E\left[\frac{\psi_{m+1,n+1} - \psi_{m+1,n-1} - \psi_{m-1,n+1} + \psi_{m-1,n-1}}{(z_{n+1} - z_{n-1})(\phi_{m+1} - \phi_{m-1})}\right] = F. \quad (23)$$

Rearranging this equation so that like ψ terms are grouped together, and defining $\Delta z \equiv z_{n+1} - z_{n-1}$ and $\Delta\phi \equiv \phi_{m+1} - \phi_{m-1}$, results in:

$$\frac{E}{\Delta z\Delta\phi}\psi_{m-1,n-1} - \frac{B}{\Delta z}\psi_{m,n-1} - \frac{E}{\Delta z\Delta\phi}\psi_{m+1,n-1} + \left[\frac{4D}{\Delta\phi^2} - \frac{C}{\Delta\phi}\right]\psi_{m-1,n} + \left[A - \frac{8D}{\Delta\phi^2}\right]\psi_{m,n} + \left[\frac{C}{\Delta\phi} + \frac{4D}{\Delta\phi^2}\right]\psi_{m+1,n} - \frac{E}{\Delta z\Delta\phi}\psi_{m-1,n+1} + \frac{B}{\Delta z}\psi_{m,n+1} + \frac{E}{\Delta z\Delta\phi}\psi_{m+1,n+1} = F_{m,n}. \quad (24)$$

The introduction of a second set of coefficients will again simplify the notation:

$$\begin{aligned} &a_{m,n}\,\psi_{m-1,n-1} + b_{m,n}\,\psi_{m,n-1} + c_{m,n}\,\psi_{m+1,n-1} + \\ &d_{m,n}\,\psi_{m-1,n} \quad + e_{m,n}\,\psi_{m,n} \quad + f_{m,n}\,\psi_{m+1,n} \quad + \\ &g_{m,n}\,\psi_{m-1,n+1} + h_{m,n}\,\psi_{m,n+1} + i_{m,n}\,\psi_{m+1,n+1} = F_{m,n}\,. \end{aligned} \tag{25}$$

Equation (25) represents a system of simultaneous equations for the ψ's that can be compactly expressed using matrix notation:

$$\mathbf{A}_n\,\vec{\psi}_{n-1} + \mathbf{B}_n\,\vec{\psi}_n + \mathbf{C}_n\,\vec{\psi}_{n+1} = \vec{\mathbf{f}}_n \tag{26}$$

where $\vec{\psi}_n$ and $\vec{\mathbf{f}}_n$ are $M \times 1$ column vectors composed of the individual ψ's and f's:

$$\vec{\psi}_n = \begin{bmatrix} \psi_{1,n} \\ \psi_{2,n} \\ \vdots \\ \psi_{M,n} \end{bmatrix}, \qquad \vec{\mathbf{f}}_n = \begin{bmatrix} f_{1,n} \\ f_{2,n} \\ \vdots \\ f_{M,n} \end{bmatrix} \tag{27}$$

and $\mathbf{A}_n$, $\mathbf{B}_n$, and $\mathbf{C}_n$ are $M \times M$ tridiagonal matrices composed of the coefficients of the ψ terms:

$$\mathbf{A}_n = \begin{bmatrix} b_{1,n} & c_{1,n} & 0 & \cdots & \cdots & 0 \\ a_{2,n} & b_{2,n} & c_{2,n} & 0 & \cdots & 0 \\ 0 & a_{3,n} & b_{3,n} & c_{3,n} & \cdots & 0 \\ \vdots & 0 & \ddots & \ddots & \ddots & \vdots \\ \vdots & \vdots & \cdots & a_{M-1,n} & b_{M-1,n} & c_{M-1,n} \\ 0 & 0 & 0 & \cdots & a_{M,n} & b_{M,n} \end{bmatrix} \tag{28.1}$$

$$\mathbf{B}_n = \begin{bmatrix} e_{1,n} & f_{1,n} & 0 & \cdots & \cdots & 0 \\ d_{2,n} & e_{2,n} & f_{2,n} & 0 & \cdots & 0 \\ 0 & d_{3,n} & e_{3,n} & f_{3,n} & \cdots & 0 \\ \vdots & 0 & \ddots & \ddots & \ddots & \vdots \\ \vdots & \vdots & \cdots & d_{M-1,n} & e_{M-1,n} & f_{M-1,n} \\ 0 & 0 & 0 & \cdots & d_{M,n} & e_{M,n} \end{bmatrix} \tag{28.2}$$

$$\mathbf{C}_n = \begin{bmatrix} h_{1,n} & i_{1,n} & 0 & \cdots & \cdots & 0 \\ g_{2,n} & h_{2,n} & i_{2,n} & 0 & \cdots & 0 \\ 0 & g_{3,n} & h_{3,n} & i_{3,n} & \cdots & 0 \\ \vdots & 0 & \ddots & \ddots & \ddots & \vdots \\ \vdots & \vdots & \cdots & g_{M-1,n} & h_{M-1,n} & i_{M-1,n} \\ 0 & 0 & 0 & \cdots & g_{M,n} & h_{M,n} \end{bmatrix}. \tag{28.3}$$

Of course, equations (26)–(28) hold for all N grid levels, and are therefore also more compactly expressed in matrix form:

$$\begin{bmatrix} \mathbf{B}_1 & \mathbf{C}_1 & 0 & \dots & \dots & 0 \\ \mathbf{A}_2 & \mathbf{B}_2 & \mathbf{C}_2 & 0 & \dots & 0 \\ 0 & \mathbf{A}_3 & \mathbf{B}_3 & \mathbf{C}_3 & \dots & 0 \\ \vdots & 0 & \ddots & \ddots & \ddots & \vdots \\ \vdots & \vdots & \dots & \mathbf{A}_{N-1} & \mathbf{B}_{N-1} & \mathbf{C}_{N-1} \\ 0 & 0 & 0 & \dots & \mathbf{A}_N & \mathbf{B}_N \end{bmatrix} \begin{bmatrix} \vec{\psi}_1 \\ \vec{\psi}_2 \\ \vec{\psi}_3 \\ \vdots \\ \vec{\psi}_{N-1} \\ \vec{\psi}_N \end{bmatrix} = \begin{bmatrix} \vec{\mathbf{f}}_1 \\ \vec{\mathbf{f}}_2 \\ \vec{\mathbf{f}}_3 \\ \vdots \\ \vec{\mathbf{f}}_{N-1} \\ \vec{\mathbf{f}}_N \end{bmatrix} . \qquad (29)$$

The super–matrix on the left–hand side is an $N \times N$ tridiagonal matrix whose elements are themselves tridiagonal matrices. Because this is an ill–conditioned matrix, special precautions must be taken in inverting it to solve for the ψ's. Yuk Yung [personal communication, 1991] provided a routine for solving this set of equations; its structure is similar to that of programs designed to invert tridiagonal matrices with scalar elements [*Press et al.*, 1989].

The solution to equation (29) depends on the boundary conditions that are applied. We assume that $\psi \equiv 0$ on the boundaries of the domain, which are the south pole, the north pole, the surface, and the top of the atmosphere. This condition requires that there is no mass flow through these boundaries. These boundary conditions can be stated as:

$$\psi_{1,n} = \psi_{M,n} = \psi_{m,1} = \psi_{m,N} = 0 . \qquad (30)$$

Because of these boundary conditions, we only need solve for interior grid points, resulting in a reduction in the total dimensions of the matrices in equation (29) such that: $M \rightarrow M-2$, $N \rightarrow N-2$.

Once the tridiagonal solver has yielded values for the stream function, equation (18) is used to calculate the residual circulation:

$$\overline{v}^*_{m,n} = \frac{1}{\cos\phi_m}\left[\frac{\psi_{m,n}}{H} - \frac{\psi_{m,n+1}-\psi_{m,n-1}}{z_{n+1}-z_{n-1}}\right] \qquad (31.1)$$

$$\overline{w}^*_{m,n} = \frac{1}{a\cos\phi_m}\left[\frac{\psi_{m+1,n}-\psi_{m-1,n}}{\phi_{m+1}-\phi_{m-1}}\right] . \qquad (31.2)$$

The stream function model was validated in several ways. First, its behavior was examined for a variety of input vertical and horizontal grids. The nominal temperature and net heating rate fields are specified on a vertical grid composed of 30 levels equally–spaced in the logarithm of the pressure between 6.0 mbar and 10^{-3} mbar, and on a horizontal grid divided into 10° latitude bins. Bilinear interpolation was used to map these fields onto higher–resolution grids. Several experiments were performed, with a maximum resolution of 50 vertical levels and 2.5° latitude bins. The model behavior was very consistent for all of the test cases, with no spurious structure introduced by the additional degree of resolution.

The stream function model was also validated by computing the diabatic circulation of the terrestrial atmosphere for four representative months (January, April, July, October). The meridional temperature cross–sections for these calculations were obtained from an eight–year average of National Meteorological Center (NMC) data (1979–1986, inclusive), and the ozone profiles were obtained from a seven–year average of SAGE II data [Mimi Gerstell, personal communication, 1992]. The circulation above the 20 km level deduced from the NMC temperatures using the stream function model was compared to a number of other recent diagnostic calculations. These studies, which employ a variety of radiative transfer schemes and input temperature and ozone data, include: *Hitchman and Leovy* [1986], *Solomon et al.* [1986], *Rosenfield et al.* [1987], *Gille et al.* [1987], *Shine* [1989], and *Yang et al.* [1990]. Despite the differences in both data and models, all these studies produce generally similar fields, and our results compare favorably to them in both overall structure and actual velocities.

3. The Radiative Transfer Model

An accurate description of the diabatic heating in the atmosphere is crucial

for determining the diabatic circulation. As discussed in Section 2.1, the diabatic heating can be assumed to equal the net radiative heating for this Martian season. *Crisp* [1986; 1989] developed an efficient, accurate radiative–convective–equilibrium model which accounts for absorption, emission, and multiple scattering by particles and non–grey gases. We use this model to compute solar fluxes and heating rates and thermal fluxes and cooling rates from diurnal averages of the temperature and dust distributions retrieved from the IRIS data in Paper I. Net radiative heating rates are found by summing the solar heating and thermal cooling rates at each latitude and atmospheric level. A brief description of the radiative transfer model is given in the next two sections.

3.1 Solar Heating Rates

Both scattering and absorption contribute to the extinction of solar radiation in the Martian atmosphere. During dusty conditions, the principal scatterers are the dust particles suspended in the atmosphere, but Rayleigh scattering by CO_2 molecules also causes extinction. In addition, CO_2 and dust particles are the principal absorbing constituents in the atmosphere. *Crisp* [1990] computed globally–averaged solar heating rates in a dust–free model Martian atmosphere and showed that absorption by O_3, H_2O, CO, and O_2 produces negligible heating at most levels. The problem of finding solar fluxes and heating rates in a vertically inhomogeneous, scattering, absorbing atmosphere is discussed in detail in *Crisp* [1986] (for Venus) and will only be summarized briefly here. This problem can be separated into two parts: (1) the solar flux in the ultraviolet and visible regions, which is calculated by considering multiple scattering and absorption by dust particles and Rayleigh scattering by CO_2 molecules (*i.e.*, gaseous absorption is ignored), and (2) the solar flux in the near–infrared region, which is calculated by considering only absorption by dust particles and CO_2 (*i.e.*, scattering in the near–infrared absorption bands is ignored).

The radiative heating rate depends on the amount of radiative energy that is deposited in the atmosphere, and it therefore depends on the divergence of the solar flux along the optical path:

$$\frac{dT}{dt} = -\frac{g}{c_p}\frac{dF^{\text{net}}}{dp} \tag{32}$$

where F^{net} is the frequency–integrated net solar flux, which is the difference between the upward and downward solar fluxes. The computation of the solar heating rate therefore requires a detailed description of the solar flux distribution throughout the atmosphere.

To calculate solar fluxes in the Martian atmosphere, the solar spectrum is divided into 216 bands between 0.18 μm and 5.5 μm, chosen such that the optical properties and the solar flux are nearly constant across each band. The vertically inhomogeneous atmosphere is divided into 30 homogeneous layers, equally–spaced in the logarithm of the pressure, between the surface (at 6 mbar) and approximately the 10^{-3} mbar level. This pressure grid matches that of the global temperature maps of Paper I. The optical properties, including the effective extinction optical depth (the sum of the dust scattering and absorption optical depths and the Rayleigh scattering optical depth for CO_2), the single–scattering albedo (the ratio of the scattering optical depth to the extinction optical depth), and the scattering asymmetry parameter (a measure of the degree of forward scattering), are specified in each atmospheric layer for each solar spectral band. The flux is then found for the mean values of these quantities in each narrow interval, and the results are summed.

For the case of scattering of solar radiation in a plane–parallel atmosphere, the radiative transfer equation for the diffuse intensity, $I(\tau,\mu)$, takes the form of a complicated integro–differential equation. Various techniques have been developed to obtain an approximate solution to this equation. Eddington methods are first moment methods that represent the angular dependence of the intensity field in terms of two

functions of optical depth, τ. That is, $I(\tau, \mu) = I_0(\tau) + \mu\, I_1(\tau)$, where μ is the cosine of the zenith angle. Here, we use the delta–Eddington approximation of *Joseph et al.* [1976]; this method is also discussed in *Meador and Weaver* [1980] and *King and Harshvardhan* [1986], among others. The equation of transfer is replaced by two coupled, first–order ordinary differential equations describing the upward and downward intensities. In order to solve these equations, it is necessary to specify the form of the single–scattering phase function, which describes the angular distribution of the scattered radiation. Scattering from particles larger than the wavelength is characterized by highly asymmetric phase functions, with strong forward–scattering components. Under the delta–Eddington approximation of *Joseph et al.* [1976], the phase function is parameterized by a Dirac delta function forward scatter peak and a two–term Legendre polynomial expansion. It should be noted that the delta–Eddington approximation is most accurate for optically–thick atmospheres with large single–scattering albedos [*King and Harshvardhan*, 1986], and might produce flux errors as large as 15 percent for optically–thin cases with small single–scattering albedos [*Crisp*, 1986].

The delta–Eddington/adding model described by *Crisp* [1986] provides an approach for applying the delta–Eddington method to vertically–inhomogeneous atmospheres. The *Crisp* [1986] model employs the delta–Eddington approximation to define the coefficients of the pair of differential equations and solve for the diffuse reflectivity and transmissivity of each homogeneous layer as well as the upward diffuse flux and the downward diffuse flux at the interfaces between the atmospheric layers. The vertical inhomogeneity of the atmosphere is treated by concatenating the homogeneous layers using a simplified version of the layer–adding method proposed by *Shettle and Weinman* [1970] and *Lacis and Hansen* [1974]. Given the reflectivity and transmissivity of two individual layers, the reflectivity and transmissivity of a composite layer is obtained by computing the successive reflections back and forth

between the two layers. This method is used to find the diffuse reflectivity and the downward diffuse flux at the base of inhomogeneous layers which were built up by starting at the top of the atmosphere and successively adding homogeneous layers onto the bottom of the combined layer. In a similar manner, this method provides the diffuse reflectivity and the upward diffuse flux at the top of inhomogeneous layers which were built up by starting at the surface and successively adding homogeneous layers onto the top of the combined layer. These reflectivities and diffuse fluxes are then combined to calculate the upward, downward, and net fluxes at each model atmosphere level. The total ultraviolet and visible solar flux is found by computing these fluxes in each solar spectral interval and summing the results.

In the near–infrared, absorption by CO_2 becomes important. The strongest CO_2 bands are the ν_3 asymmetric stretch fundamental centered at 4.3 μm and combination bands centered 2.0, 2.7, 4.8, and 5.2 μm; there are also several weaker combination bands located between 1 and 2 μm. Within gas absorption bands, we neglect the effects of multiple scattering and use a fundamentally different approach to compute the solar flux. Unlike in *Crisp* [1986], the gas transmittance is calculated using a Voigt quasi–random model [*Crisp*, 1990]. The dust transmittance is calculated from the dust optical depth using Beer's law, and the total atmospheric transmittance, $\mathcal{T}$, is found by taking their product. These algorithms are described in Paper I and the Appendix. The downward flux at any level is then determined by:

$$F(p) = F_0 \cos\theta_z \mathcal{T}(p, \theta_z) \tag{33}$$

where F_0 is the solar flux incident at the top of the atmosphere, and θ_z is the solar zenith angle. In a similar manner, the upward flux at any level is determined from the component of the incident radiation reflected by the surface. These upward and downward values are calculated in each near–infrared spectral interval and combined to produce net quantities which are in turn added to the results from the ultraviolet

and visible regions to yield total net solar fluxes. Equation (32) is then applied to compute the solar heating rate at each model atmosphere level.

3.2 Thermal Cooling Rates

Although the emission and absorption of infrared radiation can produce either heating or cooling of the atmosphere, at longer wavelengths it is traditionally referred to as "thermal cooling". A detailed description of the use of the radiative transfer model to compute thermal fluxes and cooling rates is presented (for Venus) in *Crisp* [1989], and is only briefly summarized here. The spectrum in this region is divided into 27 unevenly–spaced intervals between 5.5 μm and 500 μm. This range includes the strong CO_2 absorption band centered at 15 μm, due to the ν_2 bending fundamental, as well as several other combination bands centered at 7, 8, 9.6, and 10.6 μm. The CO_2 transmittances are calculated using the Voigt quasi–random model [*Crisp*, 1990] (unlike in *Crisp* [1989]). Because the single–scattering albedo of the dust particles is quite low over much of this wavelength range (Paper I), atmospheric scattering processes are ignored. However, absorption by the dust particles is significant and is again treated by Beer's law.

Expressions for the upward and downward thermal fluxes can be derived from the equation of radiative transfer. For a narrow frequency interval, $\Delta\nu$, these expressions are:

$$F^{\uparrow}(\Delta\nu,p) = \epsilon\pi B[\Delta\nu,T_s]\,\mathcal{T}(p_s,p,\Delta\nu) - \int_{p}^{p_s} \pi B[\Delta\nu,T(p)]\,\frac{d\mathcal{T}(p,p',\Delta\nu)}{dp'}\,dp' \quad (34.1)$$

$$F^{\downarrow}(\Delta\nu,p) = \int_{0}^{p} \pi B[\Delta\nu,T(p)]\,\frac{d\mathcal{T}(p,p',\Delta\nu)}{dp'}\,dp' . \quad (34.2)$$

The first term on the right–hand side of equation (34.1) is a boundary term that accounts for the upwelling radiation from the surface, which is assumed to have a wavelength–dependent emissivity, ϵ, and a temperature, T_s. B is the Planck function,

and $\mathcal{T}(p, p', \Delta\nu)$ is the atmospheric transmittance between levels p and p'. Equation (34.2) lacks a boundary term because it is assumed that there is no source of thermal flux at the top of the atmosphere (only one percent of the incident solar flux falls in this wavelength region). The integral in both equations accounts for the transfer of thermal radiation between each level of the atmosphere and all other levels. These integrals are solved numerically by methods described in *Crisp* [1989]. Subtracting the upward and downward values yields net thermal fluxes, from which the cooling rate at each atmospheric level can be calculated using equation (32).

3.3 Optical Properties of the Airborne Dust Particles

To account for airborne dust particles in the solar and thermal flux calculations, the wavelength–dependent optical properties of the dust must be specified. In Paper I, we assumed that the dust is composed of palagonite, which is its closest spectral analog. The real and imaginary refractive indices of palagonite were provided by *Roush* [1991]. A log–normal particle size distribution with a mode radius of 0.5 μm and a variance of 0.15 was adopted, and a Mie–scattering program was used to compute the extinction efficiency factors for the dust particles over the range 5.0–25.0 μm. These dust parameters produce a much better match to the IRIS spectra in our data subset than those derived by *Toon et al.* [1977], who used a modified gamma distribution with a mode radius of 0.4 μm. In particular, the ratio of 9 μm to 20 μm dust optical depth is significantly improved. The same information is required in the visible and near–infrared regions of the spectrum to calculate solar fluxes, but these wavelengths were not included in the *Roush* [1991] study.

The radiative properties of the suspended dust particles at solar wavelengths have been defined by *Pollack et al.* [1977], and revised by *Pollack et al.* [1979]. They analyzed observations of the Martian sky and several celestial objects taken by the

cameras on the Viking Landers to estimate the dust optical depth, mean particle radius, imaginary index of refraction, single scattering albedo, asymmetry parameter, and extinction efficiency. The latter three parameters are tabulated as a function of wavelength between 0.35–1.05 μm in *Pollack* [1982].

We initially used the *Pollack* [1982] quantities in the radiative transfer model to calculate solar fluxes and heating rates. We calculated the visible optical depths from the retrieved 9 μm optical depth, the 9 μm extinction efficiency computed by the Mie scattering program, and the visible extinction efficiencies of *Pollack* [1982]. For example, the dust extinction optical depth at 0.6 μm ($\tau(0.6\,\mu\text{m})$) was obtained from the known 9 μm value ($\tau(9\,\mu\text{m})$) via the relation:

$$\tau(0.6\,\mu\text{m}) = \frac{Q_{\text{ext}}(0.6\,\mu\text{m})}{Q_{\text{ext}}(9\,\mu\text{m})}\,\tau(9\,\mu\text{m}) \tag{35}$$

where the Q_{ext} terms are the extinction efficiency factors. However, the ratio of the *Pollack* [1982] $Q_{\text{ext}}(0.6\,\mu\text{m})$ to the computed $Q_{\text{ext}}(9\,\mu\text{m})$ is approximately 7. Previous studies have estimated this ratio to be 1.85 [*Zurek*, 1982] and 2.5 [*Martin*, 1986]. The large value of the ratio of the visible to 9 μm extinction efficiencies resulted in large visible dust opacities ($\tau_{\text{vis}} \sim 1.5$), which in turn resulted in large solar heating rates. Residuals between the globally–averaged solar heating and thermal cooling rates were as large as 35 K/day at some atmospheric levels. The expectation that a state of approximate radiative equilibrium should prevail throughout most of the Martian atmosphere suggests that these visible extinction efficiencies are too high.

The most likely source for this error is the choice of the particle size distribution in the calculation of the infrared extinction efficiency factors of the dust. As discussed in Paper I, this choice was motivated by a need for a narrower particle size distribution than the one used by *Toon et al.* [1977] in order to reproduce the observed IRIS spectra at both 9 μm and 20 μm. However, the log–normal size distribution we selected is probably too narrow. A recent analysis of infrared spectrometer (ISM) observations of

Mars in the range 0.75–3.15 μm from the Phobos 2 spacecraft [*Drossart et al.*, 1991] also concludes that the *Toon et al.* size distribution cannot reproduce the component of the spectrum due to airborne dust for the low–dust conditions during the Phobos mission. *Drossart et al.* use a generalized Mie scattering model to fit retrieved ISM dust reflectance spectra, and find that a narrower modified gamma distribution (with a mode radius of 0.31 μm) provides a much better fit for low–dust conditions than the *Toon et al.* distribution. The mode radius of the *Drossart et al.* size distribution is smaller than the mode radius of our distribution, but, because their modified gamma distribution is broader than our log–normal distribution, it encompasses both larger and smaller particles. We experimented with the new *Drossart et al.* distribution, and found that it produces nearly identical $\tau(20\,\mu\text{m})/\tau(9\,\mu\text{m})$ ratios, and much smaller $\tau_{\text{vis}}/\tau(9\,\mu\text{m})$ ratios (~ 3.125), but it still produces unrealistically large solar heating rates. Further investigations of dust particle size distributions were beyond the scope of this work.

The simplest way to address this problem is to scale the visible extinction efficiencies by a constant factor, which is chosen by trial and error to produce small solar heating—thermal cooling residuals in the global average. The wavelength–dependence of the *Pollack* [1982] values is preserved because all quantities between 0.35–1.05 μm are multiplied by the same factor. We find that scaling the extinction efficiencies by 0.25 produces reasonable solar heating results (with residuals between the globally–averaged solar heating and thermal cooling rates generally about 5 K/day). This factor corresponds to a ratio of visible to infrared optical depth of 1.75, which is more in line with the previous estimates. The impact that airborne dust will have on both the solar heating and the thermal cooling rates can be evaluated by examining the absorption efficiency factor, Q_{abs}, which is calculated by differencing the extinction and scattering efficiency factors. Q_{abs} is plotted as a function of wavenumber in Fig-

ure 2. The dust absorption peaks at 9 μm and is also significant in the 15–20 μm region, as discussed in Paper I. Figure 2 shows that dust absorption is also strong in the range 0.35–0.5 μm, where a significant fraction of the total solar flux falls.

4. Results and Discussion

We used the diagnostic methods described in Section 2 to define two aspects of the atmospheric dynamics: the gradient winds, and the net meridional circulation. These calculations require a knowledge of the atmospheric temperature structure. The diurnal–mean temperature distribution was obtained by averaging the 2 AM and 2 PM meridional–plane cross–sections of atmospheric temperature presented in Paper I. These diurnally–averaged temperatures are shown in Figure 3. The IRIS spectra from which the temperatures were determined were obtained during $L_S = 343° - 348°$, corresponding to late southern summer on Mars.

For consistency with the results of Paper I, the vertical coordinate in all subsequent figures is the atmospheric pressure, p. The approximate altitude, z, corresponding to a given pressure level can be calculated from equation (2); z is plotted as a function of p in Figure 4. This correlation of altitude with pressure is based on the following values: $p_s = 6.0$ mbar, $R = 191.0$ J/K/kg, $g = 3.74$ m/s^2, and $T = 196$ K (the globally– and diurnally–averaged value of the atmospheric temperature at the surface), resulting in a mean scale height $H = 10$ km.

Because the net radiative heating rates are central to the calculation of the diabatic circulation, they are discussed first. Solar heating rates and thermal cooling rates are calculated from the IRIS temperature maps using the radiative transfer model, and the influence of airborne dust on the radiative forcing is investigated. Next a description of the zonal–mean zonal winds is provided. Although the principal results are obtained from the gradient thermal wind equation, winds obtained from

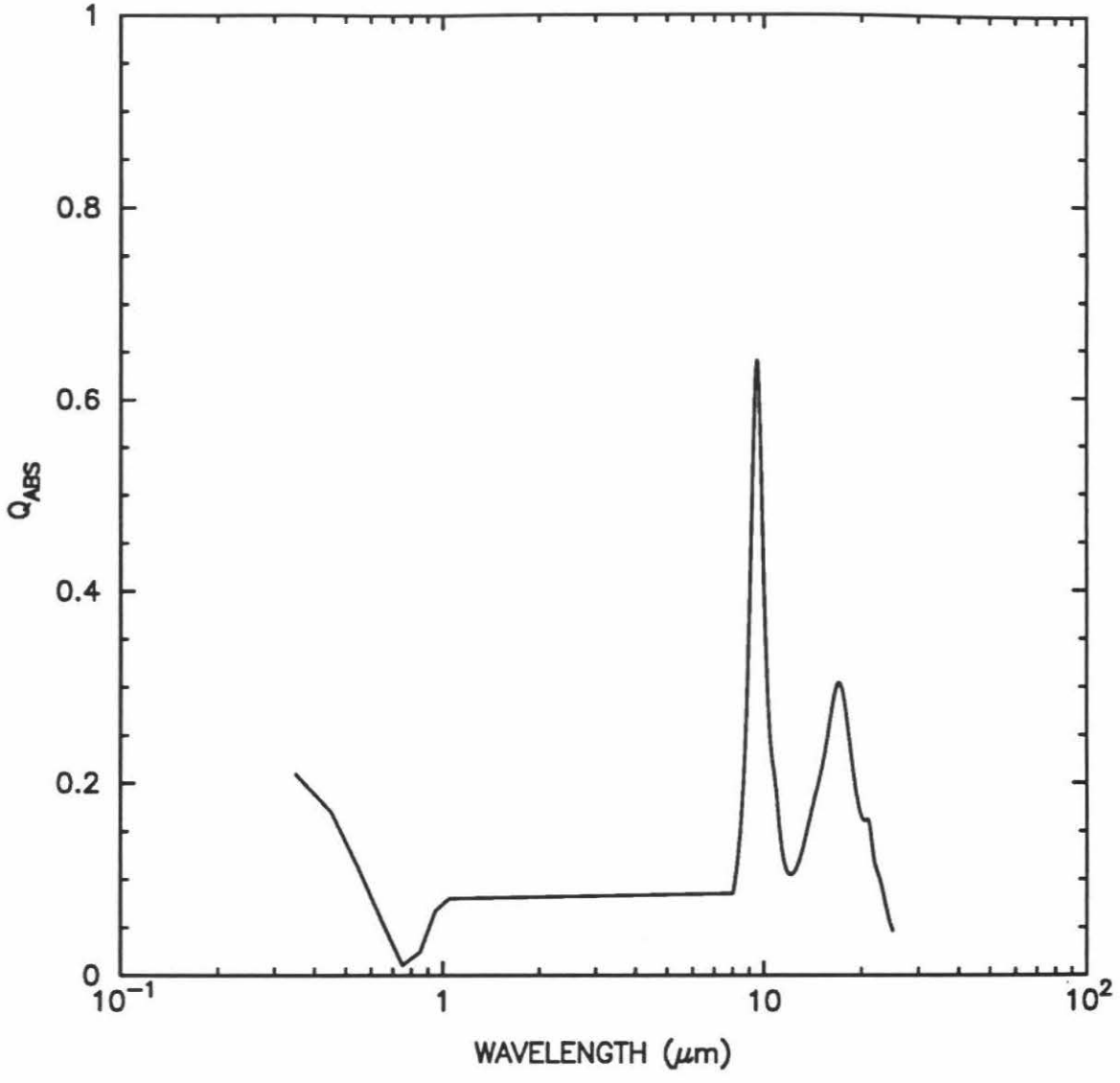

Figure 2. Absorption efficiency factor Q_{abs} for Martian dust particles. The infrared values (5–25 μm) were obtained in Paper I, the visible values (0.35–1.05 μm) were obtained by scaling the results of *Pollack* [1982] by a factor of 0.25, and values in the intermediate region of the spectrum were obtained by linear interpolation.

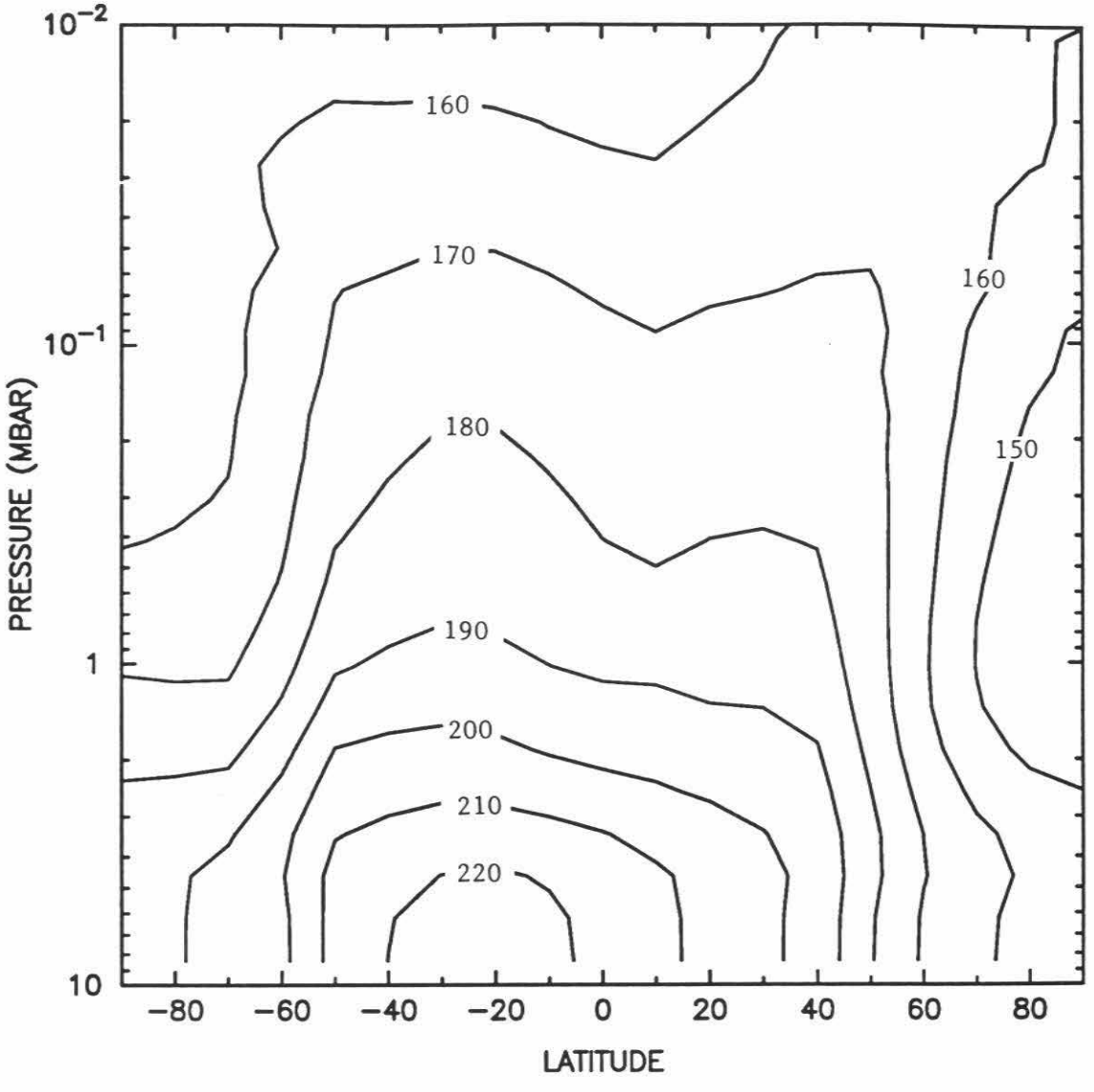

Figure 3. Diurnal–mean temperatures obtained by averaging the 2 AM and 2 PM temperature maps retrieved from the IRIS spectra in Paper I.

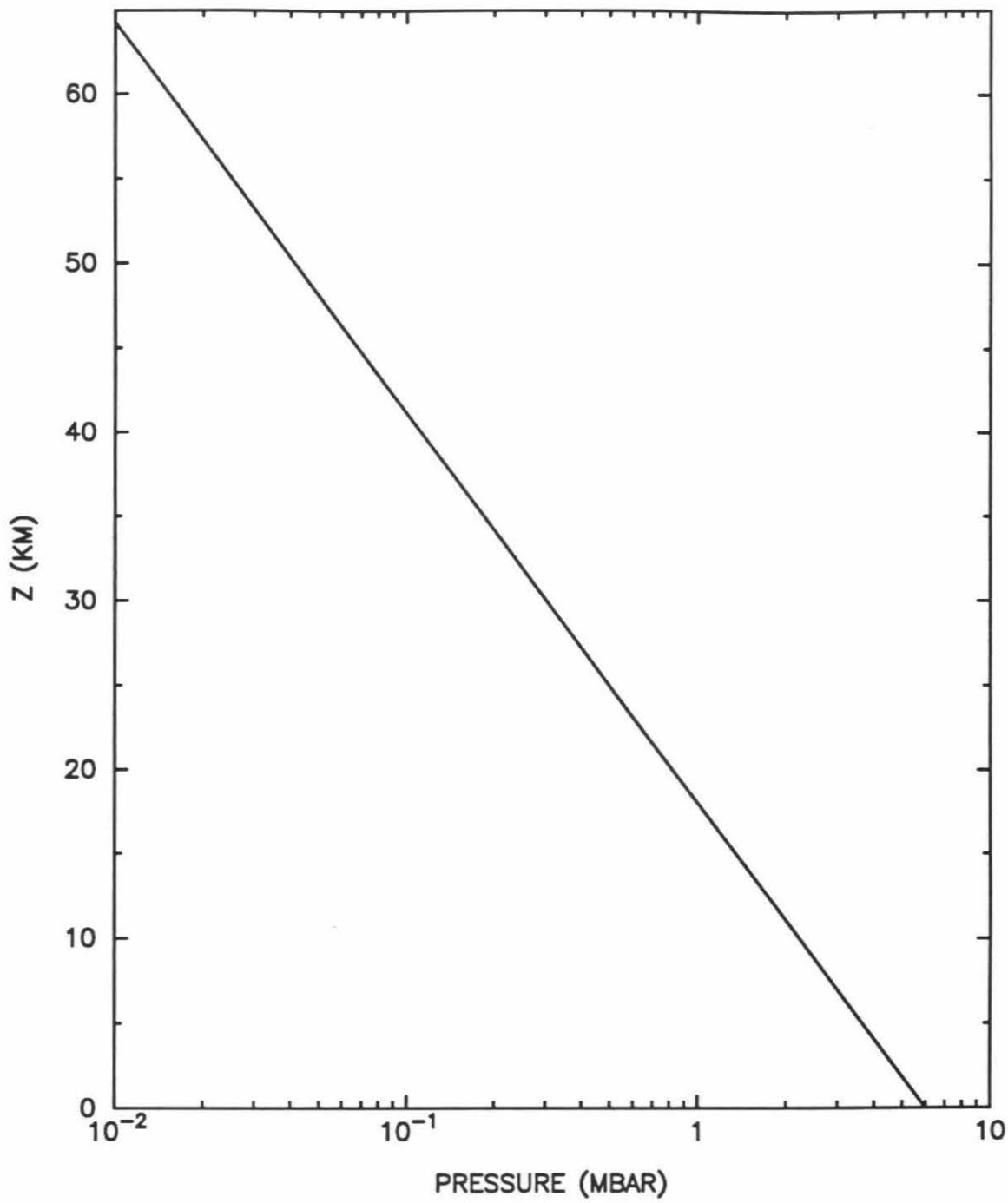

Figure 4. Log–pressure altitude as a function of pressure. Approximate altitudes corresponding to the pressure coordinates of all subsequent figures can be found from this plot.

the geostrophic thermal wind equation are also included to facilitate comparisons with previous studies. Finally, the vertical and meridional components of the diabatic circulation diagnosed from the net heating rates using the stream function model are presented, and various implications of the magnitude and direction of this circulation are explored.

4.1 Solar Heating, Thermal Cooling, and Net Heating Rates

Radiative heating and cooling rates depend on the flux divergence along the atmospheric path (see equation (32)), which in turn depends on the absorber abundances. The vertical distribution of heating rates is therefore strongly influenced by the vertical distribution of the principal absorbers. In the terrestrial middle atmosphere, absorption by O_3 is responsible for the majority of the solar heating, and the structure of the temperature and heating rate fields is closely coupled to its vertical profile. In contrast, O_3 abundances on Mars are low, and *Crisp* [1990] has shown that O_3 contributes less than one percent to the solar heating rates at most levels. In the Martian atmosphere, CO_2 is the most important absorbing gas at solar wavelengths [*Crisp*, 1990], but airborne dust can produce much more absorption at these wavelengths (Figure 2), and consequently much larger heating rates.

We have used the radiative transfer model described in Section 3 to investigate the impact of airborne dust on the solar heating and thermal cooling rates. Diurnal averages of the retrieved IRIS temperature and dust distributions from Paper I were used to calculate solar heating rates under dusty atmospheric conditions. They are shown as a function of latitude and pressure in Figure 5a. The maximum solar heating rate, 20 K/day, occurs over the equatorial regions. There is a slight asymmetry in the meridional distribution of solar heating rate, with southern latitudes exhibiting more heating than the corresponding northern latitudes. This effect arises from a

combination of increased airborne dust abundances in the southern hemisphere (see Paper I) and the longer duration of daylight there at this season (late southern summer). These values can be compared to the results, shown in Figure 5b, calculated from the radiative transfer model using the same IRIS temperatures but assuming dust–free atmospheric conditions. Although the dust–free heating rates match the dusty–atmosphere values at the top of the domain, they are five to twenty times smaller at the 1.0 mbar level. The maximum values of solar heating occur at lower altitudes under dusty conditions because the vertical dust profile is peaked at the surface (see Paper I). The enhanced heating rates obtained for the dusty–atmosphere conditions illustrate that absorption of solar radiation by airborne dust particles provides the most potent radiative drive in the Martian atmosphere. However, these solar heating rates must be used with caution because their magnitudes are a strong function of the vertical dust opacity profile and the optical properties assumed for the dust particles at visible wavelengths (see Section 3.3), which are poorly constrained by existing observations.

Although airborne dust exerts the major influence on solar heating rates, CO_2 dominates the thermal cooling rates at pressures below 1 mbar. Throughout this region of the atmosphere, the primary energy loss occurs via emission in the CO_2 15 μm band. This band is particularly effective for cooling the atmosphere because the peak of the Planck function for a blackbody at $T = 200$ K is situated at 15 μm. Airborne dust can also contribute substantially to the cooling near the surface. The general pattern of cooling in Figure 6a (corresponding to the dusty–atmosphere conditions) correlates very strongly with the temperature and dust distributions. The cooling rates are largest (> 25 K/day) at low altitudes over the summer tropics, where atmospheric temperatures and dust abundances are highest, and they are smallest (~ 5 K/day) at low altitudes over the polar regions, where atmospheric tempera-

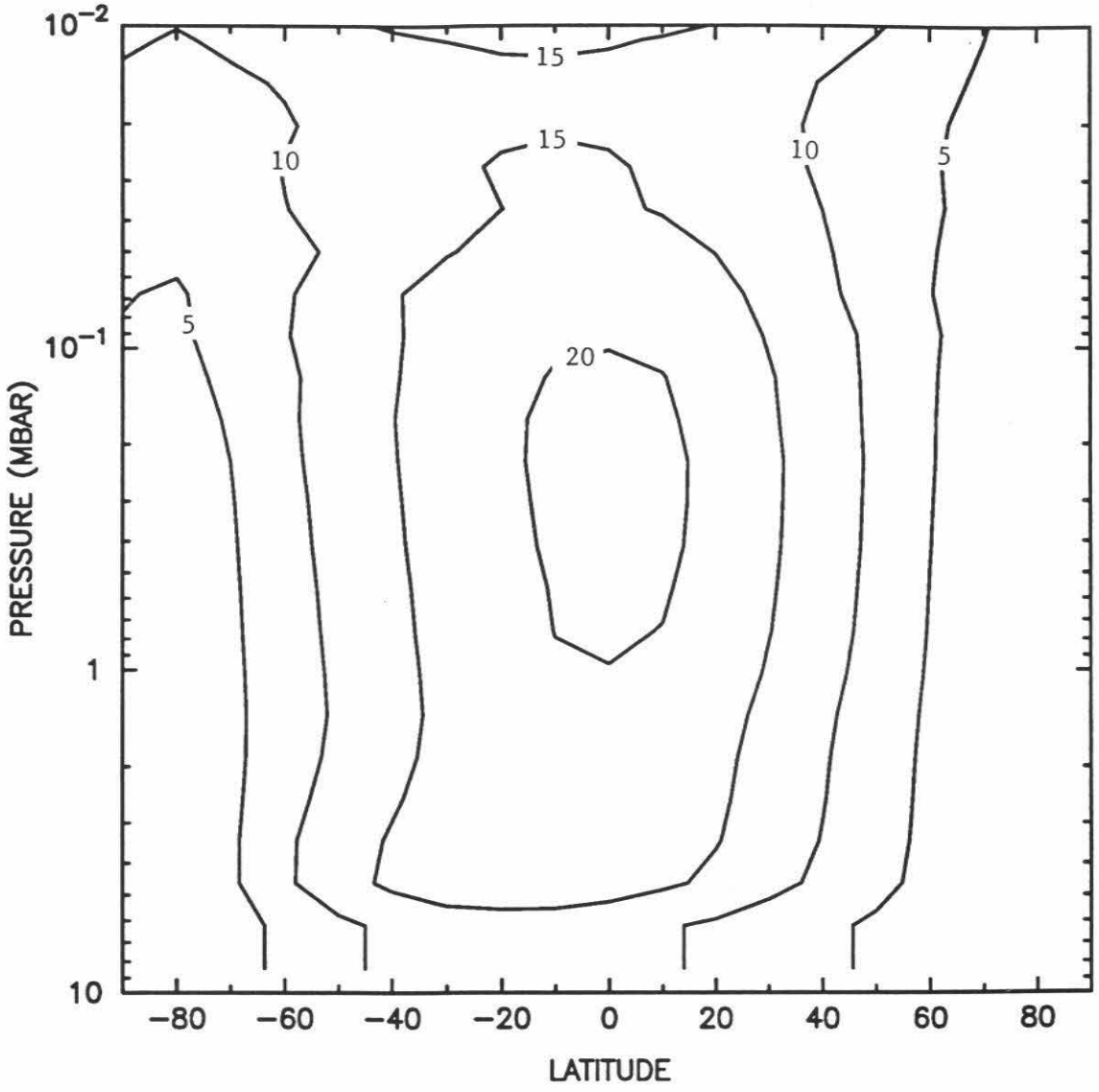

Figure 5a. Solar heating rates (K/day) calculated from the retrieved IRIS temperature and dust distributions using the radiative transfer model.

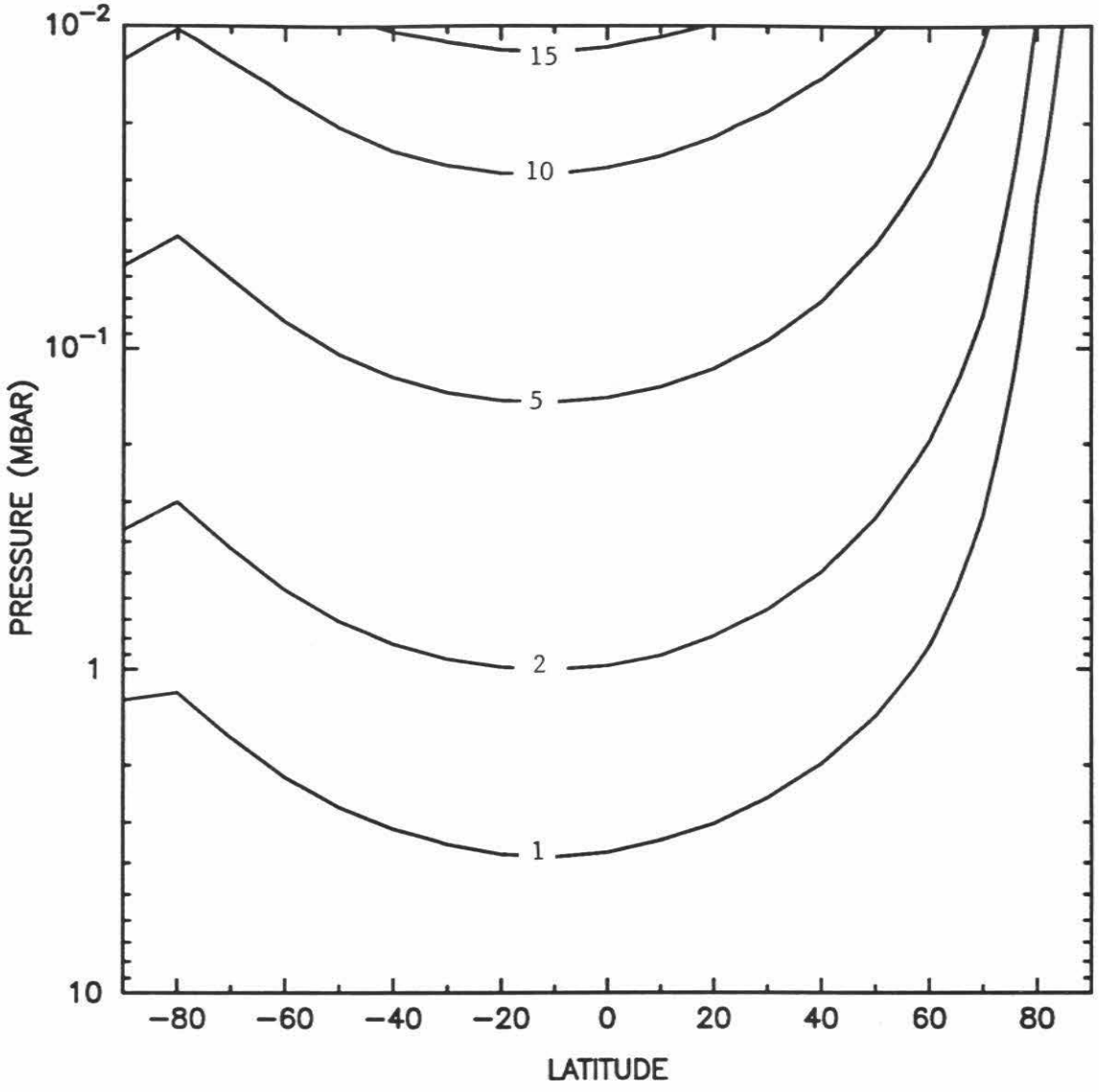

Figure 5b. Solar heating rates (K/day) calculated from the retrieved IRIS temperature distribution but assuming that the atmosphere is dust–free. The contour interval is nonuniform.

tures and dust abundances are lowest. The cooling rates in the equatorial regions do not vary monotonically with altitude. A portion of the thermal flux emitted by the warm atmospheric layers nearest the surface is absorbed by the overlying cooler layers. There is therefore a thermal heating component to offset some of the thermal cooling, resulting in lower thermal cooling rates around the 1 mbar level. Above this level of reduced thermal cooling, the cooling rates increase by about 5 K/day, and then decrease as the atmospheric temperature drops near the top of the domain.

The cooling rates for the dust–free atmosphere (Figure 6b) are virtually identical to those of Figure 6a at pressures below 1 mbar. However, the cooling rates for the two cases are entirely different in the tropical lower atmosphere, where much less cooling occurs in the dust–free case. The discrepancy between these two sets of cooling rates arises from the contribution to the cooling made by airborne dust particles, and the inherent differences between gas (line) emission and dust (continuum) emission. The radiation mean free path is inversely proportional to the local absorber density [*Goody and Yung*, 1989]. At lower pressures, the radiation mean free path is relatively long, and photons emitted by CO_2 molecules have a high probability of reaching space. Near the surface, the line cores are optically thick, and the radiation mean free path is extremely short. Photons emitted by CO_2 molecules have a high probability of being re–absorbed by other CO_2 molecules. Because the line core regions are optically thick at low altitudes, the transmittance, the flux divergence, and the cooling rates are small. This situation is changed when the effects of airborne dust are included. For non–dust storm conditions, the dust in the atmosphere is optically thin, so that the emitted photons have a high probability of reaching space. In addition, unlike CO_2, which can emit only in narrow spectral lines, the absorption coefficient of the dust is relatively uniform at all wavenumbers (see Figure 2). The dust particles are therefore effective broad–band emittors, and they produce the large

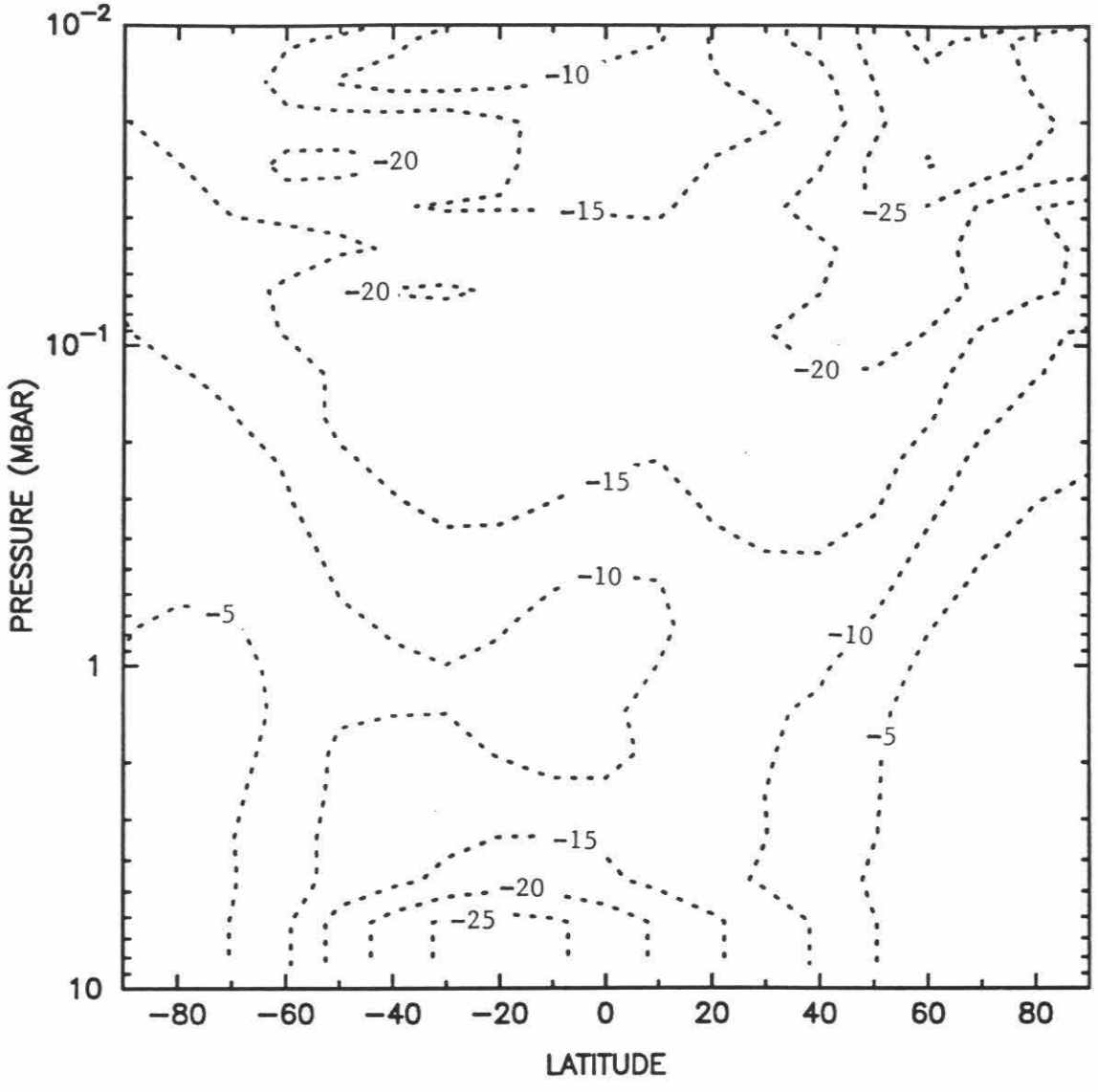

Figure 6a. Thermal cooling rates (K/day) calculated from the retrieved IRIS temperature and dust distributions using the radiative transfer model.

cooling rates in the lower atmosphere which appear in Figure 6a.

The relative role that dust plays in determining the radiative heating rates can be further illuminated by calculating their global–average values. For the atmosphere to be in perfect radiative equilibrium, the solar heating and thermal cooling terms must exactly cancel. However, the fact that radiative equilibrium is not satisfied locally in a certain region of the atmosphere does not preclude the possibility of global radiative equilibrium there. The effects of large–scale motions in the atmosphere are largely nullified in the global average. Area–weighted globally–averaged heating and cooling rate profiles are shown in Figure 7a for the dusty–atmosphere conditions. Departures of approximately thirty percent from global radiative equilibrium are seen at the levels just above the surface, where convection acts to cool the surface and warm the atmosphere. The disparities between the globally–averaged solar heating and thermal cooling rates in other regions of the atmosphere are most likely due to uncertainties in the dust optical properties or vertical distribution. The dust retrieval algorithm of Paper I does not strongly constrain the vertical distribution of the dust, and as a result the retrieved dust profiles are not unique. The redistribution of even a minute quantity of dust along the atmospheric column could reduce the solar heating below 0.3 mbar and enhance it above that level, bringing the two curves in Figure 7a into closer agreement. Small uncertainties in the dust extinction efficiencies, as described in Section 3.3, could also explain the excess solar heating in the lower part of the atmosphere. The net heating residuals in Figure 7a are not much larger than those often computed for the terrestrial atmosphere (see, *e.g.*, *Rosenfield, et al.* [1987]), where the atmospheric temperatures and absorber amounts are much better constrained by observations.

Global average solar heating and thermal cooling rates for the dust–free case are shown in Figure 7b. The thermal cooling rates above 1 mbar are virtually un-

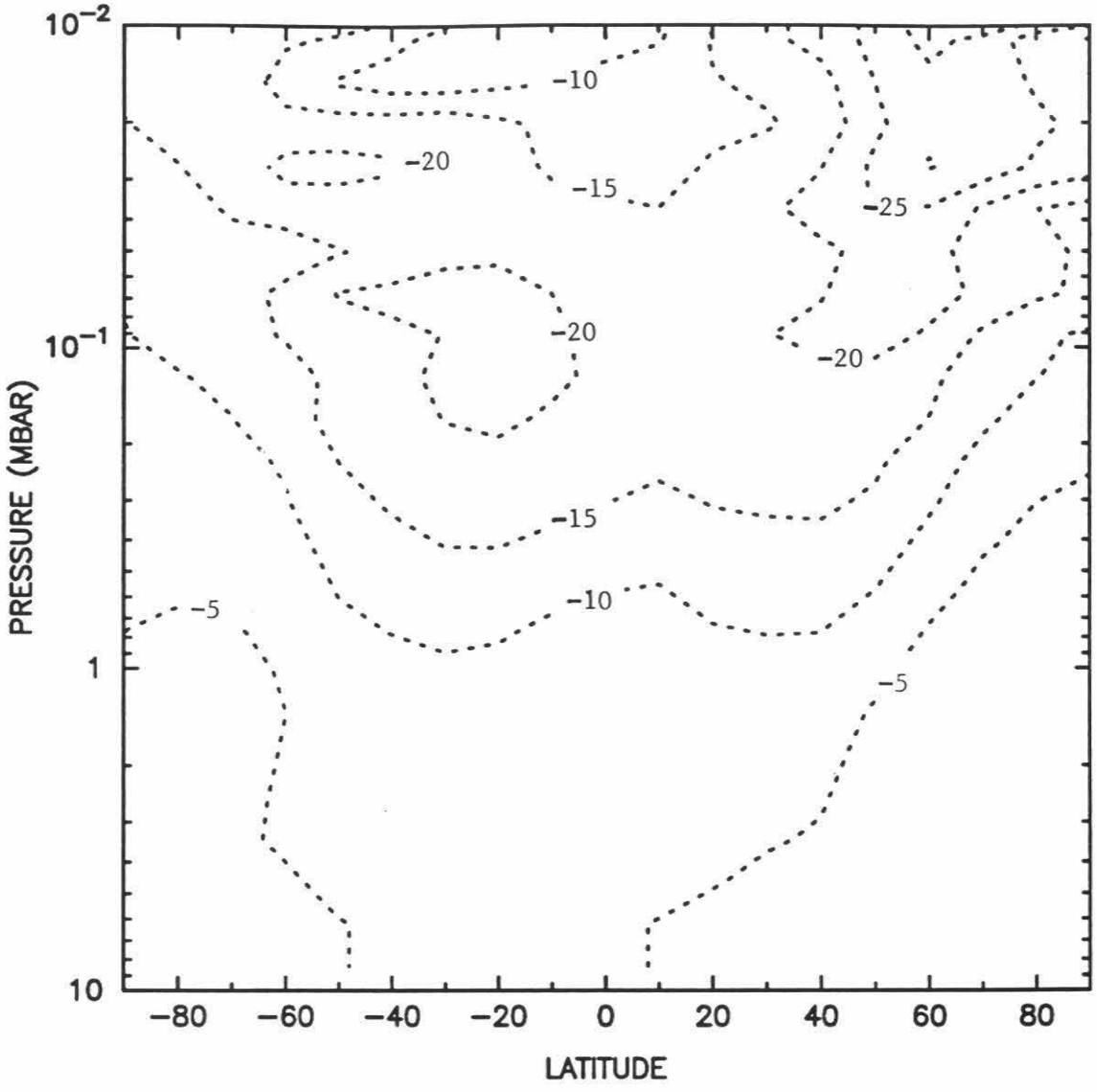

Figure 6b. Thermal cooling rates (K/day) calculated from the retrieved IRIS temperature distribution but assuming that the atmosphere is dust–free.

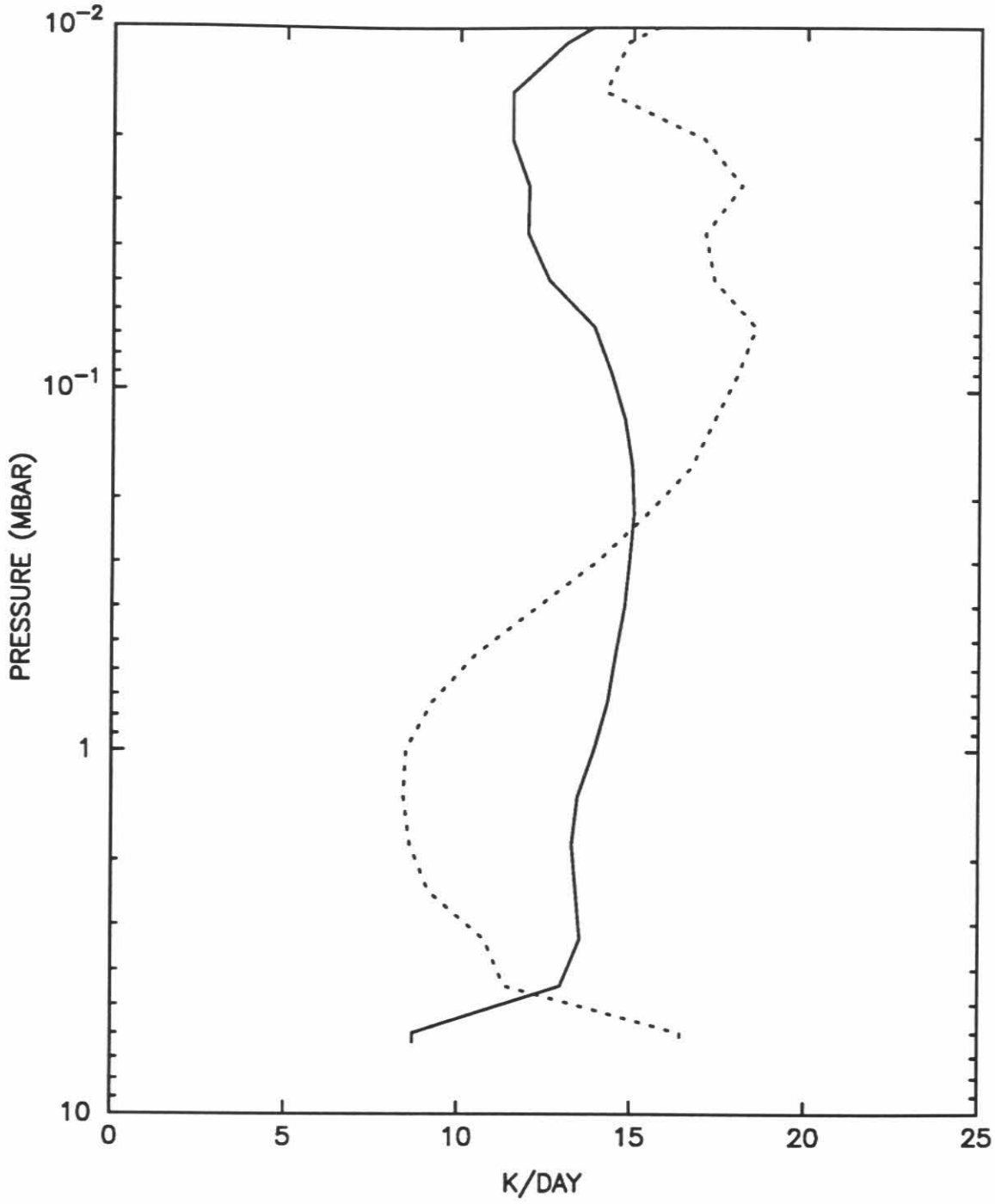

Figure 7a. Global–average solar heating (solid line) and thermal cooling (dashed line) rate profiles for the dusty–atmosphere conditions. The absolute values of the thermal cooling rates are plotted here.

changed, while the cooling rates below 1 mbar are significantly smaller for the dust–free case, as discussed for Figure 6. In the absence of dust heating, the globally–averaged solar heating rate varies from about 1 K/day at the surface to about 14 K/day at 10^{-2} mbar. These results agree closely with those obtained by *Crisp* [1990] using a dust–free model atmosphere and an earlier version of the radiative transfer model.

Net radiative heating rates, found by summing the solar heating (Figure 5a) and thermal cooling (Figure 6a) rates at each latitude and atmospheric level, are presented in Figure 8. (Net heating rates are not shown for the dust–free case. The temperatures from which the cooling rates are calculated (Figure 3) have been strongly influenced by the presence of dust in the atmosphere, and their use in an assessment of the effects of dust on the net heating would introduce an inherent inconsistency.) For presentation purposes, the net heating rates have been normalized by subtracting the residual of the global–average rates of Figure 7a at each pressure level. This procedure will not affect the calculation of the diabatic circulation (see Section 2.5). At pressures below 4.0 mbar, there are large net heating rates (up to 8 K/day) in the equatorial region and large net cooling rates (up to 20 K/day) in the polar regions. The heating and cooling rates are approximately symmetric about the equator, although the polar cooling is much weaker in the southern hemisphere (where the sun is shining). Because no large temperature changes occur during the twelve days represented by this subset of IRIS data (see Paper I), there must exist a non–radiative mechanism which acts to cool the tropics (by up to 8 K/day) and warm the polar regions (by up to 20 K/day) in order to maintain the observed temperature structure in the presence of this radiative forcing. For example, upwelling over the equator would produce expansional cooling to offset the net radiative heating, while downwelling over the poles would produce compressional heating to offset the net radiative cooling. This

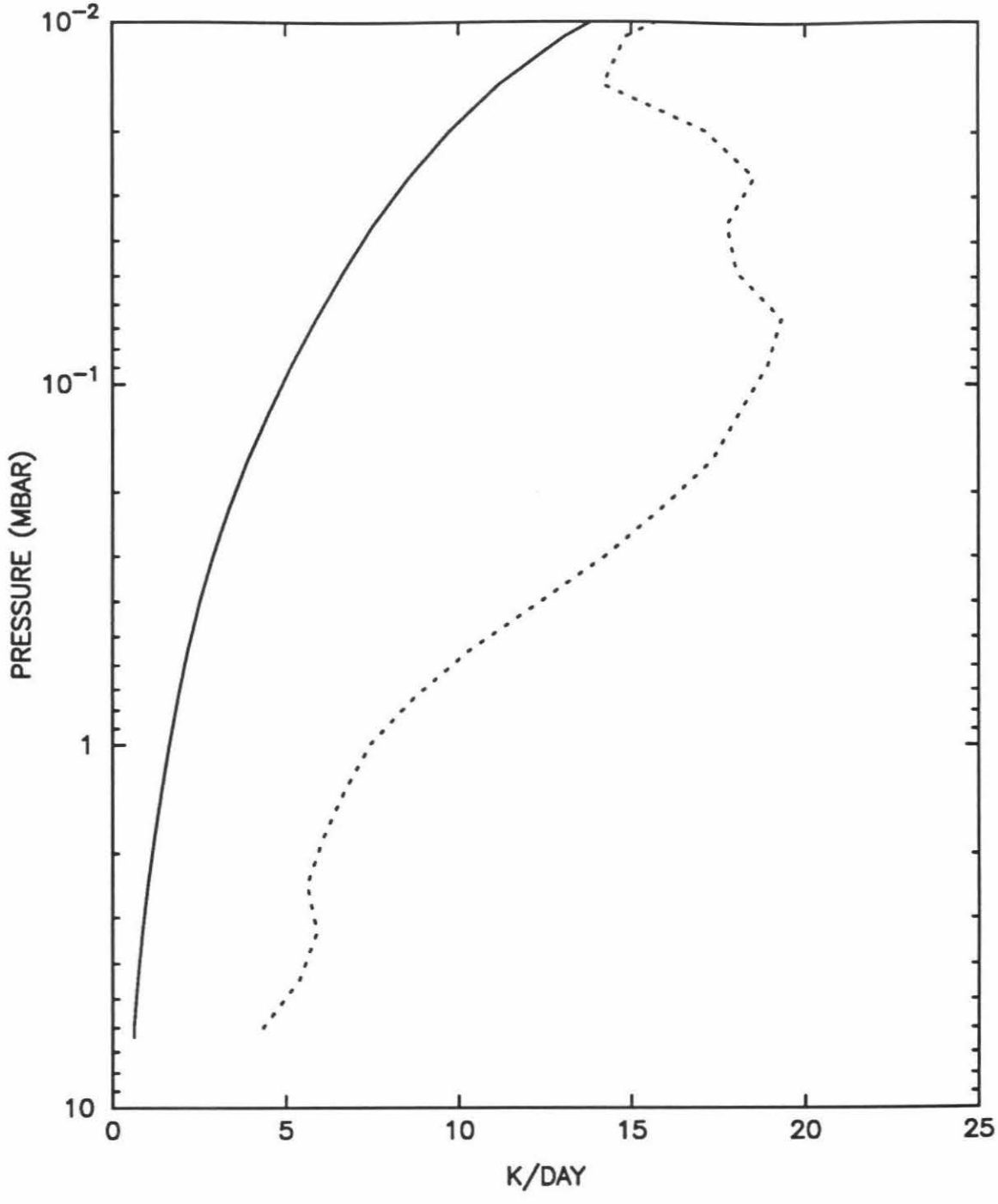

Figure 7b. Global–average solar heating (solid line) and thermal cooling (dashed line) rate profiles for the dust–free case. The absolute values of the thermal cooling rates are plotted here.

circulation, called the diabatic circulation, is described in Section 4.3.

4.2 Zonal–Mean Zonal Winds

The zonal winds were computed from the gradient thermal wind equation (equation (11.1)) assuming zero wind velocity at the surface. The resulting gradient wind field is shown in Figure 9a. One of the characteristics of the thermal wind equation is that the zonal wind increases with altitude in the presence of equator–to–pole temperature gradients. Because the horizontal temperature gradients are steeper in the northern (winter) midlatitudes (see Paper I), the eastward (westerly) winds aloft are slightly more intense over the northern regions, although both hemispheres have strong mid–latitude eastward jets. Winds in the equatorial regions where the Coriolis parameter approaches zero are omitted from this figure. In the southern tropics the winds are strongly westward (easterly); there is only a small corresponding region of easterlies at the top of the domain in the northern hemisphere.

For comparison purposes, a calculation was performed with the same temperatures but using the simpler geostrophic thermal wind equation (equation (11.2)). The overall morphology of the geostrophic wind field (shown in Figure 9b) is similar to that of Figure 9a, but the geostrophic upper–level westerly jets are up to 30 m/s stronger. A parallel overestimation of the zonal–mean westerlies has been found in calculations of the terrestrial zonal winds. In a comparison of gradient and geostrophic mean zonal winds, *Marks* [1989] notes that their spatial structures are very similar but that the maximum values of the positive gradient winds are up to twenty percent less than the corresponding geostrophic values, and that the differences between them are greatest in the regions of strong winds.

Several different calculations of the zonal winds based on Mariner 9 data have been reported previously, but none of these are global in coverage. *Briggs and Leovy*

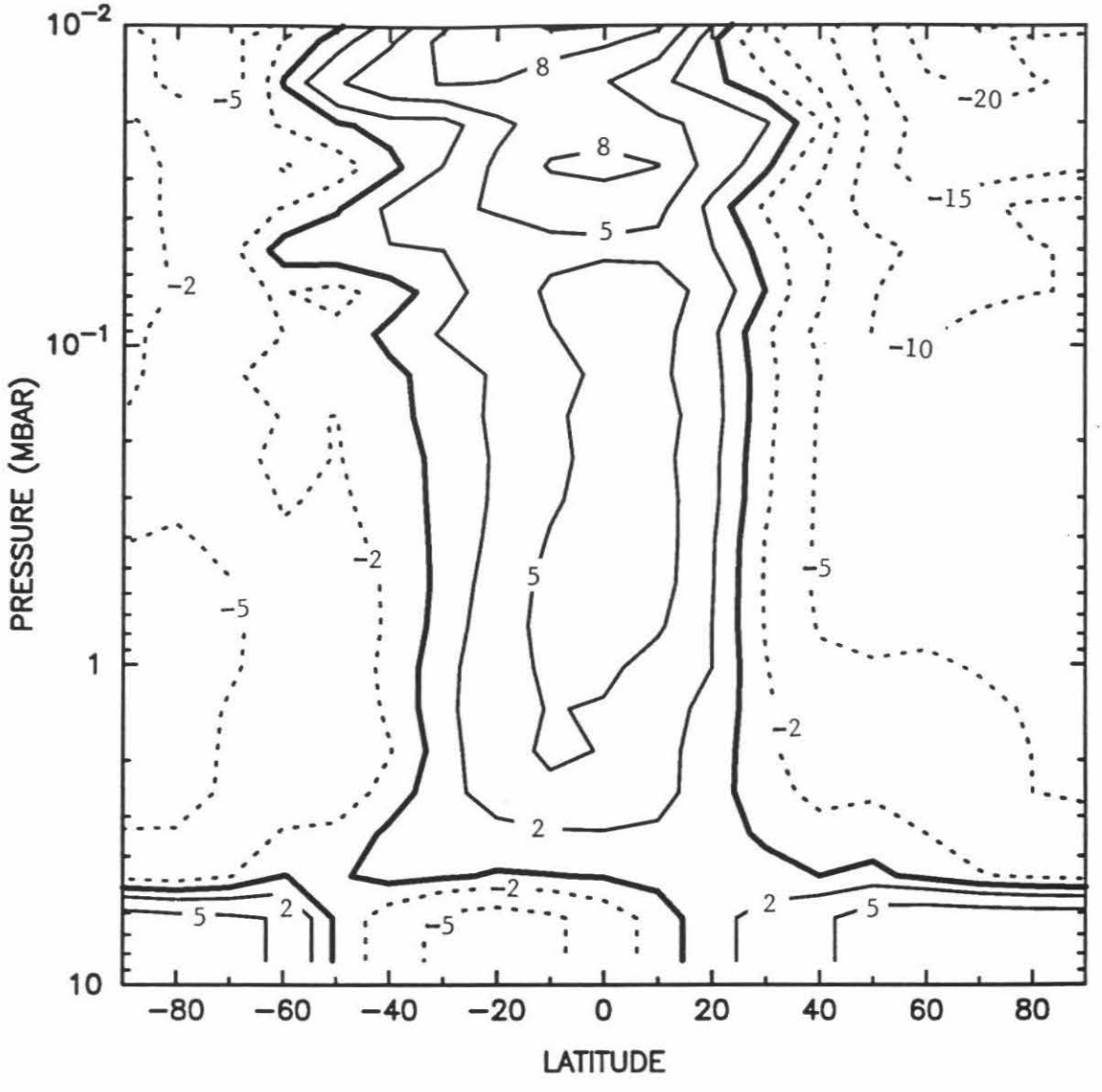

Figure 8. Net radiative heating rates (K/day) for the nominal IRIS temperatures and dust abundances, calculated by summing the solar heating and thermal cooling rates. Negative contours are dashed, the zero contour is thicker, and the contour interval is nonuniform.

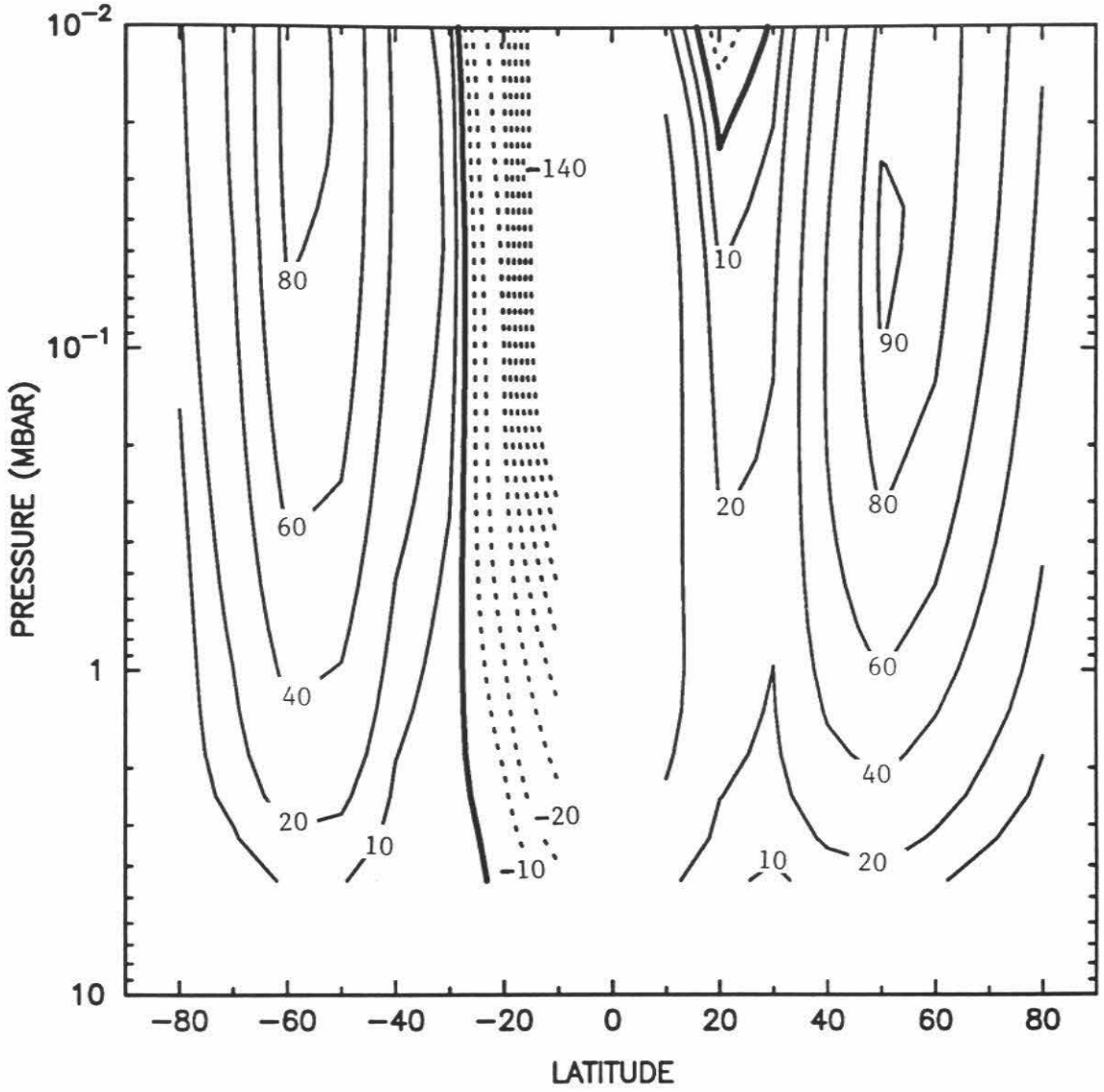

Figure 9a. Zonal–mean zonal winds calculated from the gradient thermal wind equation. Positive values represent eastward winds, negative contours are dashed, the zero contour is thicker, and the contour interval is nonuniform.

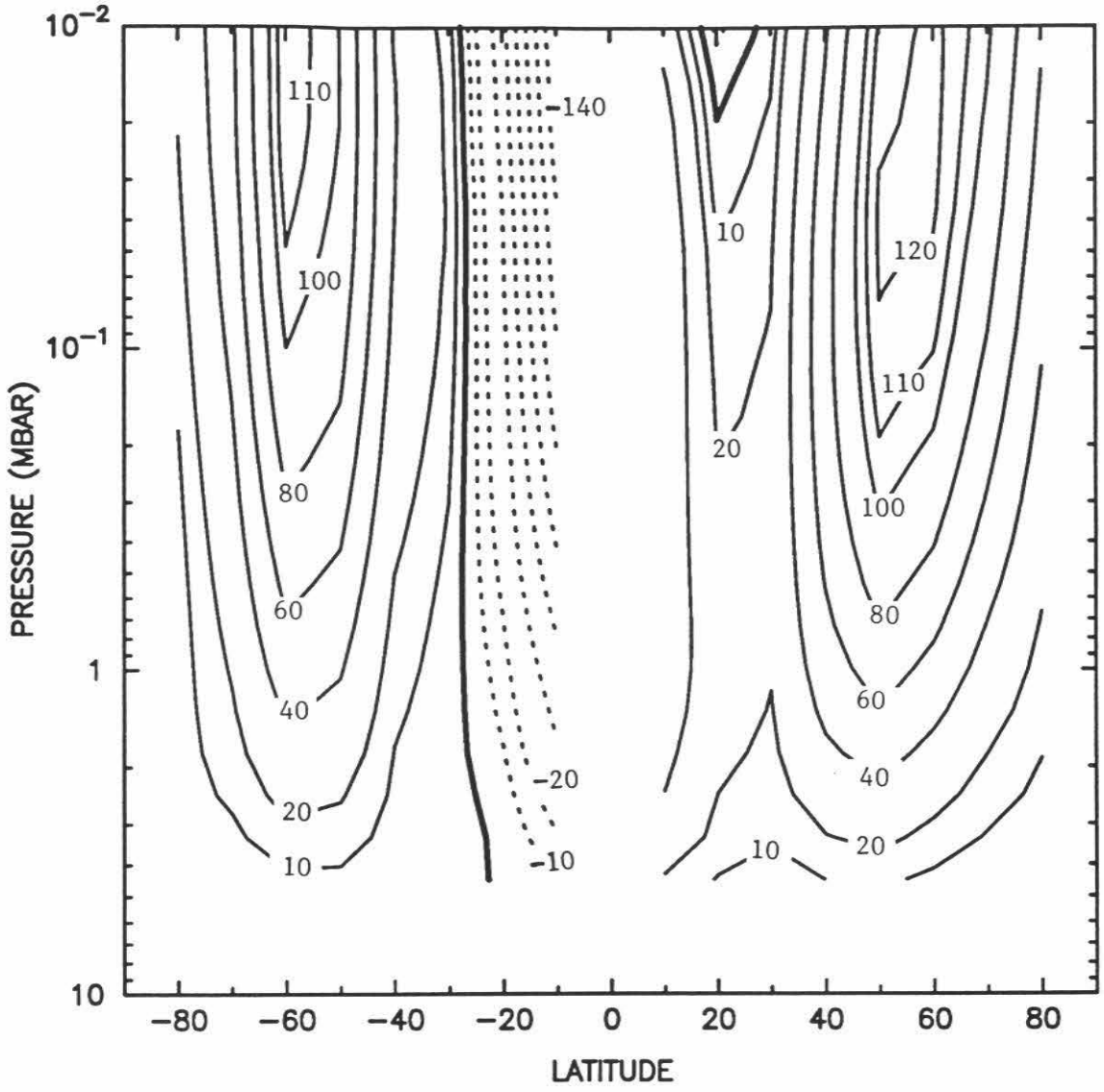

Figure 9b. Zonal–mean zonal winds calculated from the geostrophic thermal wind equation. Positive values represent eastward winds, negative contours are dashed, the zero contour is thicker, and the contour interval is nonuniform.

[1974] examine Mariner 9 television images taken during northern winter, and find evidence for resonant gravity waves in the middle latitudes. Using gravity–wave theory along with temperatures in the 45° – 50° N latitude range obtained from inversion of IRIS spectra recorded on one orbit near $L_S = 320°$ and a wavelength for the lee waves of 30 km, *Briggs and Leovy* estimate the surface zonal wind to be 10 m/s. From the geostrophic approximation they calculate a profile of the zonal wind up to 30 km altitude. Their results show the wind speed increasing up the column to a maximum value at the top of the domain of nearly 120 m/s.

Pollack et al. [1981] present geostrophic zonal winds computed from Mariner 9 IRIS data as one means of validating results from the NASA/Ames Mars general circulation model (GCM). These cross–sections encompass the area between 50° S and 70° N, from the surface to the 0.3 mbar level, and include spectra spanning $L_S = 43° - 54°$. This season is roughly midway between the spring equinox and the summer solstice in the northern hemisphere. The zonal wind field is characterized by a strong eastward jet (with velocities exceeding 120 m/s) between 1.0 mbar and 0.5 mbar at 50° S latitude, much weaker eastward winds (with velocities of 20–30 m/s) at that altitude between 60° – 80° N latitude, and westward winds (of unspecified magnitude) in the region between the equator and 40° N. The occurrence of westward winds in the northern tropics, rather than the southern tropics as in Figure 9, and the much weaker eastward winds in the northern high latitudes, are consequences of the fact that *Pollack et al.* [1981] analyzed IRIS spectra representing a different season from those of Paper I.

Haberle et al. [1992] use the NASA/Ames Mars GCM to simulate the response of the Martian atmospheric circulation to variations in season and dust loading. Comparisons with these GCM results yield some insight into the behavior depicted in Figure 9. Because the interval represented by our data subset ($L_S = 343° - 348°$)

falls between solstice and equinox, we will examine the GCM results at both of these seasons. GCM experiments for northern winter solstice ($L_S = 280° - 286°$) under relatively clear conditions reveal zonal winds which are easterly in the southern hemisphere (with peak velocities of 60 m/s) and westerly in the northern hemisphere (with peak velocities of 120 m/s). The intense westerly jet is centered near 50° – 60° N and 35–40 km altitude, whereas the easterly jet in the summer hemisphere is much broader, covering the entire tropical region at 40 km altitude. The GCM zonal wind field for a period just past northern spring equinox ($L_S = 15° - 24°$) is very symmetric with respect to the equator. Westerlies appear in both hemispheres, but these westerly jets (peak velocities of 80 m/s at 50° S and 40 m/s at 60° N) are weaker than those present during solstice conditions due to weaker latitudinal temperature gradients. Easterlies have formed in the tropical regions of both hemispheres above 30 km altitude and near the surface, although not in the intermediate region of the atmosphere. Thus, Figure 9 represents a transitional period from a season in which the winds are easterly throughout the southern hemisphere and westerly throughout the northern hemisphere, to a season in which the winds are westerly at the higher latitudes of both hemispheres and easterly in the tropics.

Geostrophic zonal winds calculated from Mariner 9 IRIS spectra at the same season as those of Paper I are reported by *Conrath* [1981]. *Conrath* constructs a northern–hemisphere mean meridional temperature cross–section by averaging temperature profiles retrieved from spectra recorded during $L_S = 330° - 350°$. He finds an eastward jet of 160 m/s at about 0.2 mbar and 60° N. *Michelangeli et al.* [1987] use the *Conrath* [1981] temperature distribution, but assume gradient wind balance to compute the zonal winds. They present a cross–section of the zonal–mean gradient wind between 15° – 85° N and 5.0 – 0.2 mbar which exhibits the same features as Figure 9a. The ageostrophic correction to the zonal–mean zonal wind reduces the

maximum eastward velocity from 160 m/s to 100 m/s, which is in better agreement with the results displayed in Figure 9a.

4.3 The Diabatic Circulation

The dynamical heat transport in the meridional plane that balances the net radiative heating is called the diabatic circulation. In the absence of wave transience or dissipation, the diabatic circulation represents the true net motion of air parcels. The diagnostic stream function model described in Section 2.5 is used to simultaneously solve for the meridional and vertical components of the diabatic circulation. This model uses the diurnal–mean temperatures of Figure 3 and the net radiative heating rates of Figure 8. The resulting meridional and vertical velocities are depicted in Figures 10a and 10b, respectively. The mass–weighted stream function can be defined [*Reiter*, 1975]:

$$\Psi_m = 2\pi a \rho_s e^{\frac{-z}{H}} \psi \,. \tag{36}$$

The density of the atmosphere at the surface is $\rho_s = p_s/gH = 1.6 \times 10^{-2}$ kg/m^3. Equation (36) was used to construct the stream lines of mass flow, which are shown in Figure 10c.

Figures 10a–10c depict a two–cell diabatic circulation, with rising motion in the equatorial region and sinking motion over both poles. Figure 10a shows transport from the equator toward the poles throughout most of the atmosphere, with return flow in the lowest levels. The vertical velocity field is fairly symmetric (Figure 10b), although the southern hemisphere exhibits a bias toward upward motion, while the northern hemisphere exhibits a bias toward downward motion. This data set represents a transitional period ($L_s = 343° - 348°$) between solstitial and equinoctial conditions. It is likely that the vertical velocity field becomes even more symmetric as the season progresses towards the equinox.

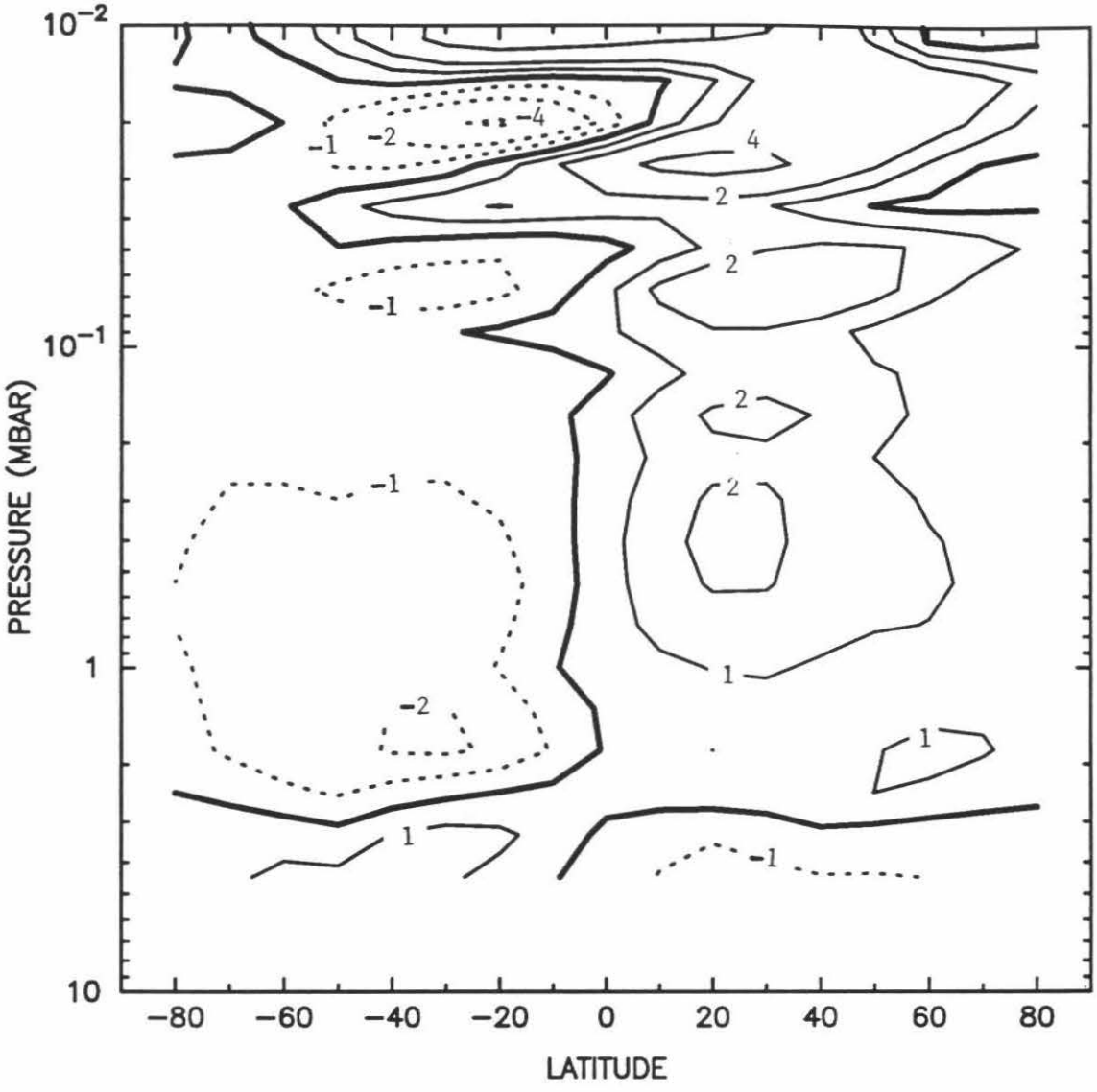

Figure 10a. Diabatic meridional velocity, in m/s. Positive values represent northward winds, negative contours are dashed, the zero contour is thicker, and the contour interval is nonuniform.

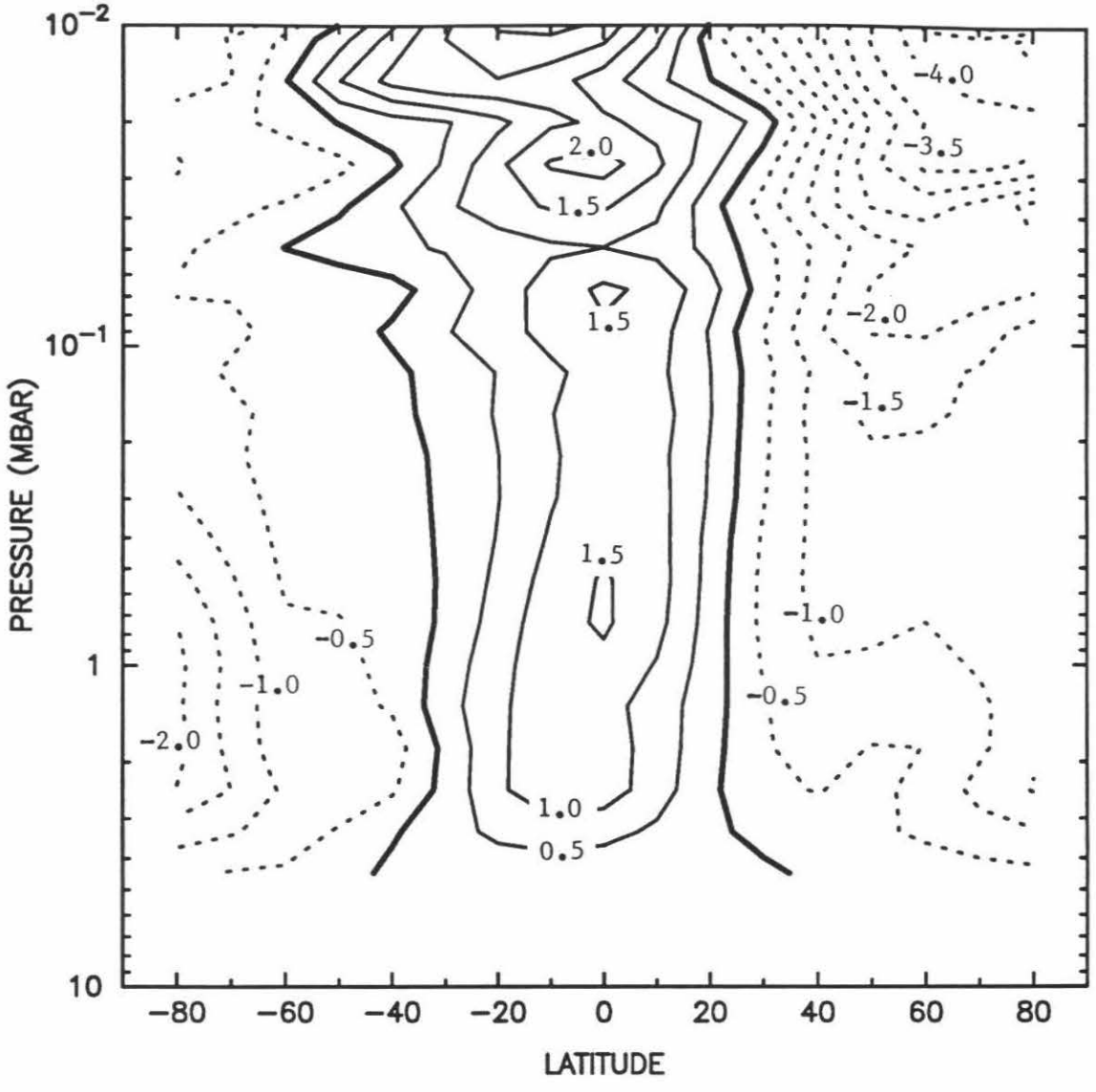

Figure 10b. Diabatic vertical velocity, in cm/s. Positive values represent upward winds, negative contours are dashed, and the zero contour is thicker.

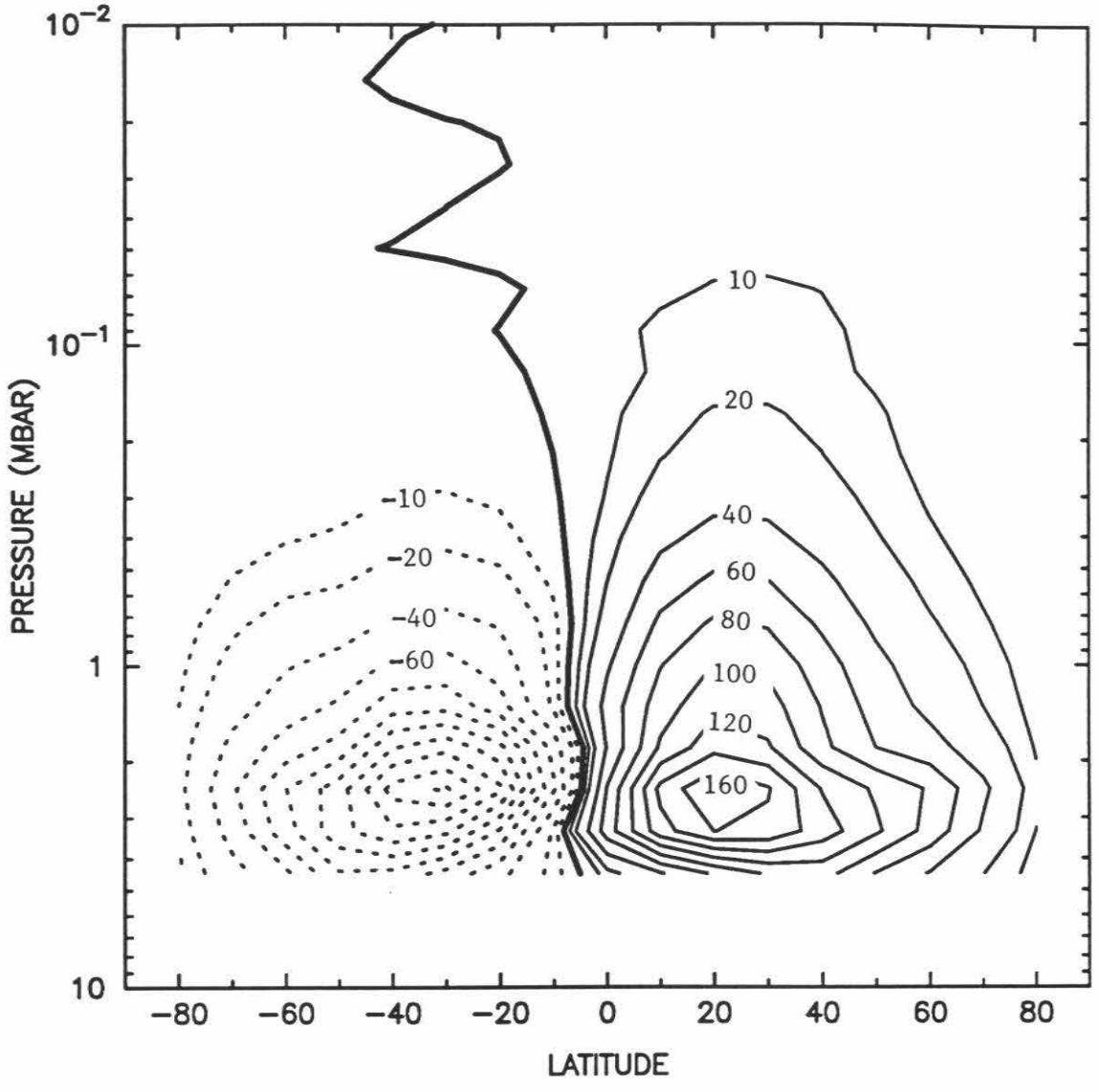

Figure 10c. Mass–weighted stream function, Ψ_m, in units of 10^7 kg/s. Positive values represent clockwise flow, negative contours are dashed, the zero contour is thicker, and the contour interval is nonuniform.

These results can be compared to those of *Moreau et al.* [1991], which were derived from a two–dimensional coupled chemical, radiative, and dynamical model of the dust–free Martian atmosphere. They obtain the meridional distribution of temperature at $L_S = 351°$ by explicitly including radiative transfer and transport of heat in the solution of the thermodynamic energy equation. They model the transport by a transformed Eulerian mean meridional circulation which is forced by wave driving. Their parameterization of the wave driving includes planetary and gravity wave dissipation, but neglects the effects of atmospheric tides. In addition, they use a much more approximate radiative transfer model than the one described in Section 3. They neglect the effects of atmospheric dust, which dominates the solar heating even during relatively "clear" periods. They use an empirical parameterization for the CO_2 absorption at near–infrared wavelengths which does not include Voigt effects, and consequently is not valid for the low–pressure Martian atmosphere. Their radiative transfer model at thermal wavelengths also neglects Voigt effects, and above 40 km altitude they employ a Newtonian cooling formulation to calculate the cooling rate. These simplifications result in modeled temperatures which are about 20 K cooler than those of Figure 3 throughout most of the atmosphere. They present a plot of the stream function, the general character of which agrees well with Figure 10c. Although they do not include plots of the velocity fields, they quote values for the maximum meridional velocity of 1.6 m/s at 50 km and 45° N latitude, and the maximum vertical velocity downward over the polar regions of 1.3 cm/s. The diabatic circulation computed from IRIS observations (Figure 10) is more robust than the circulation derived by *Moreau et al.* [1991]. We find a maximum meridional velocity of 4 m/s at about 55 km at both 20° N and 20° S latitudes, and a maximum downward vertical velocity of 4 cm/s at 60 km over the north pole.

The Martian atmosphere contains substantial quantities of dust even dur-

ing non–dust storm conditions, and we account for the consequent enhancement of the thermal forcing in our models. Because the thermal structure the atmosphere would have in the absence of dust is not an observable quantity, our diagnostic model cannot be used to infer the dust–free circulation. However, simulations with a zonally–symmetric primitive equation model by *Haberle et al.* [1982] indicate that the introduction of dust into the atmosphere causes a significant strengthening of the circulation.

The stream function model results can also be compared to the Mars GCM results of *Haberle et al.* [1992] (see the discussion of this model in Section 4.2). *Haberle et al.* present a plot of the mass stream function for the northern spring equinox experiment. This circulation consists of two cells of fairly comparable strength whose common rising branch is centered slightly south of the equator. The peak mass flux associated with these cells (10^9 kg/s) is in good agreement with the maximum contour of Figure 10c. Unfortunately, *Haberle et al.* do not include any information about the individual meridional or vertical velocity fields, so no comparisons with Figures 10a or 10b can be made.

Comparison of Figure 8 and Figure 10b shows that the vertical velocity structure strongly reflects the diabatic heating distribution. The strength of the meridional circulation is directly proportional to the strength of the radiative drive because it provides the necessary adiabatic heating and/or cooling compensation. The diabatic circulation presented in Figures 10a–10c is qualitatively similar to the terrestrial diabatic circulation at a comparable season, but it is generally more vigorous. Comparisons with the calculations for the terrestrial atmosphere cited above reveal that the Martian horizontal velocity is higher by as much as a factor of two, while the Martian vertical velocity is up to ten times higher.

In the Earth's stratosphere, the meridional circulation is extremely important

to the distribution of trace gases, particularly ozone. At lower stratospheric altitudes, where the photochemical lifetime of ozone is long, its abundance is primarily controlled by the atmospheric dynamics. The mean circulation provides a mechanism for exchange between tropospheric and stratospheric air masses. The tropical branch of the circulation introduces significant amounts of tropospheric air into the stratosphere, which, for reasons of mass continuity, must return to the troposphere at high latitudes. If advection by the mean circulation is the most important process involved in troposphere–stratosphere exchange, it is possible to define a characteristic advective exchange time, or residence time, for parcels in the stratosphere [*Reiter*, 1975; *Chamberlain and Hunten*, 1987]:

$$t_A^{-1} = -\frac{1}{\mathcal{M}} \frac{d\mathcal{M}}{dt} \tag{37}$$

where $\mathcal{M}$ is the total stratospheric air mass.

The strong mean meridional circulation in the Martian atmosphere should also play an important role in the distribution of airborne dust, as well as water (ice, vapor) and other trace gases. We have evaluated equation (37) for Mars. We estimate the mass of the Martian "stratosphere" (the atmosphere above the 1 mbar, or approximately 20 km, level) by multiplying the column density above that level, $\int_{20\ \mathrm{km}}^{\infty} \rho(z) dz = 1\ \mathrm{mbar}/g$, by the surface area at that level, $S = 4\pi(a + 20\ \mathrm{km})^2$, to give $\mathcal{M} = 3.9 \times 10^{15}$ kg. Substituting equations (18.1) and (18.2) into equation (36) leads to:

$$\Psi_m(\phi, z) = -2\pi a \rho_s \cos\phi \int_0^z e^{\frac{-z'}{H}} \overline{v}^* \, dz' \tag{38.1}$$

$$\Psi_m(\phi, z) = 2\pi a^2 \rho_s e^{\frac{-z}{H}} \int_{-\pi/2}^{\phi} \cos\phi' \, \overline{w}^* \, d\phi' . \tag{38.2}$$

The first expression represents the vertically–integrated mass flux across latitude ϕ, and the second expression represents the horizontally–integrated mass flux across a

pressure surface, denoted by the log–pressure coordinate z. Thus the mass–weighted stream function corresponds to the integrated mass flux across a surface in either the horizontal or vertical directions, and it can be used for $d\mathcal{M}/dt$ in equation (37). We calculate the actual value of $d\mathcal{M}/dt$ by summing the absolute values of the mass–weighted stream function at the 1 mbar pressure level in the region of equatorial upwelling where the diabatic vertical velocity $\overline{w}^*$ is positive. This procedure results in a value of the integrated mass flux of about 3.5×10^9 kg/s, leading to a residence time $t_A = 1.1 \times 10^6$ s $\sim$ 13 days. We can infer a "horizontal exchange time", t_A^{N-S}, from t_A by invoking mass continuity. Because the parcels are constrained to travel around a closed stream line, the horizontal and vertical transport times must be equal, and $t_A^{N-S} = t_A$. If these large transport rates are sustained for an entire season, the Martian stratosphere is ventilated in about 13 days. This value of the exchange time conforms to modeling results obtained by *Barnes* [1990b]. He utilizes a simplified dynamical model of the zonal–mean flow to investigate the possible effects of breaking gravity waves on the circulation in the middle Martian atmosphere, defined as the region between 10–100 km. *Barnes* computes vertical velocities exceeding several centimeters per second, and concludes that the exchange time between the lower portion of the middle atmosphere (10–40 km) and the upper portion of the middle atmosphere (40–100 km) is 5–10 days. The calculation of equation (37) performed for the Earth by *Shia et al.* [1989] reveals that it takes about 1.8 years for the terrestrial stratosphere to be completely overturned.

There is another possible transport mechanism in addition to the winds: diffusion. Although the only true diffusion in the atmosphere occurs at the molecular level, it is convenient to represent turbulent mixing by analogy to molecular diffusion processes. The term "turbulence" encompasses all dynamical phenomena with length and time scales much shorter than the planetary circulations presented above.

The simplest approach to including the effects of eddy transfer in the Martian atmosphere is to parameterize the eddy heat and momentum fluxes using eddy diffusion coefficients.

The vertical eddy diffusion coefficient has been estimated by several authors using different techniques. *Conrath* [1975] deduces the dust optical depth during the dissipation phase of the 1971 dust storm from Mariner 9 IRIS temperature profiles and a simplified atmospheric heating model. He finds that the dust opacity exhibits an exponential decay with the same characteristic time constant at both upper and lower atmospheric levels. This behavior cannot be explained by gravitational settling alone; it requires substantial vertical mixing, with a vertical eddy diffusion coefficient $K_{zz} \geq 10^3$ m^2/s. *Zurek* [1976] estimates the eddy diffusion coefficient for the turbulence generated by the diurnal atmospheric tide to be $K_{zz} \sim 5 \times 10^3$ m^2/s. *Kong and McElroy* [1977] investigate a variety of photochemical models and conclude that mixing coefficients in excess of 10^3 m^2/s are required to match the observed abundances of various atmospheric constituents. *Toon et al.* [1977] use a multiple scattering radiation code to find the best fit synthetic spectra to the Mariner 9 IRIS observations. They conclude that the size distribution of the dust particles did not change appreciably during the dissipation of the dust storm, and they invoke vertical mixing on the order of 10^3 m^2/s to explain the constancy of the distribution. *Anderson and Leovy* [1978] examine Mariner 9 television reflectance profiles which crossed the limb of Mars. From an analysis of the decay of dust scale heights they also determine the vertical eddy mixing coefficient to be $K_{zz} \sim 10^3$ m^2/s.

These determinations of dynamical mixing parameterize all contributions to the vertical transport as an eddy diffusion coefficient. The derived values therefore include the effects of large–scale organized motions, such as the mean meridional circulation, and are consequently much larger than they would be if they represented

only the small–scale eddy mixing processes. The treatment of dynamics is similar in *Kahn* [1990], who uses a simple steady–state model of a nonprecipitating water ice haze to deduce the vertical eddy diffusion coefficient. However, this model, which is constrained by Viking Orbiter imaging limb observations of the haze extinction opacity and the vertical extent of the haze layer, yields values of $K_{zz} = 10$ m^2/s. *Kahn* [1990] attributes the discrepancy between his value and those determined previously to real variability in dynamical mixing due to different seasons and locations. Recently, *Moreau et al.* [1991] have calculated a meridional–plane cross–section of K_{zz} for $L_S = 351°$ using a two–dimensional model which accounts for both the advection due to the residual mean meridional circulation and eddy mixing associated with absorption of waves. They find that K_{zz} has a value of 30 m^2/s everywhere below 30 km, and at all altitudes in most of the southern hemisphere, but that it reaches about 160 m^2/s in a small area located at 55° N latitude and 55 km altitude.

The characteristic diffusion time, which is the dynamical time associated with the vertical mixing, is given by [*Chamberlain and Hunten*, 1987]:

$$t_D = \frac{H^2}{K_{zz}}. \tag{39}$$

Using a value of $K_{zz} = 30$ m^2/s from the work of *Moreau et al.* [1991], representing the majority of the atmosphere, and a scale height $H = 10$ km, the characteristic diffusion time $t_D = 3.3 \times 10^6$ s $\sim$ 40 days. Thus t_D is three times larger than t_A, implying that vertical transport in the Martian atmosphere is primarily advective, rather than diffusive, in nature. However, using the maximum K_{zz} of 160 m^2/s leads to $t_D = 6.25 \times 10^5$ s $\sim$ 7 days. This value suggests that diffusive processes dominate at higher altitudes in the winter polar regions, where planetary wave activity is maximum [*Sharman and Ryan*, 1980]. In contrast, based on an upper limit of $K_{zz} = 1$ m^2/s for the stratosphere of the Earth from *Shia et al.* [1989], the characteristic diffusion time for the terrestrial stratosphere (1.5 years) is comparable to the time scale due

to advection, and both processes are important for tracer transport.

The characteristic horizontal diffusion time over a planetary radius is defined:

$$t_D^{\mathrm{N-S}} = \frac{a^2}{K_{yy}} \tag{40}$$

where K_{yy} is the horizontal eddy diffusivity. The value of K_{yy} is even less constrained for Mars than K_{zz}. *Barnes* [1990a] uses a simplified dynamical model to simulate the transport of dust to high northern latitudes during a planetary wave–induced polar warming event. He assigns a constant value of 10^6 m^2/s to the horizontal mixing coefficient. This is the same order of magnitude as the high–latitude stratospheric K_{yy} derived for the Earth by *Shia et al.* [1989]. With this value of K_{yy} the diffusion time $t_D^{\mathrm{N-S}} = 1.2 \times 10^7$ s $\sim$ 133 days, implying that horizontal transport on Mars is primarily due to advection.

The influence that the meridional circulation has on a chemical species can be evaluated by comparing the dynamical time constant to the photochemical time constant, which is calculated for each species from its rate of loss. One of the most radiatively important trace gases in the Martian atmosphere is ozone. Although O_3 molecules are temporarily removed from the atmosphere by photolysis, its overall abundance is not affected by this process because of the rapid recombination of O and O_2. To calculate a chemical time constant it is necessary to examine the four main reactions leading to the destruction of odd oxygen ($O + O_3$) in the Martian atmosphere:

$$HO_2 + O \rightarrow O_2 + OH \tag{41.1}$$

$$O + OH \rightarrow O_2 + H \tag{41.2}$$

$$O_3 + H \rightarrow O_2 + OH \tag{41.3}$$

$$NO_2 + O \rightarrow NO + O_2 . \tag{41.4}$$

The chemical lifetime for odd oxygen is then given by:

$$t_C^{O_x} = \frac{[O_3] + [O]}{k_1 [O][HO_2] + k_2 [O][OH] + k_3 [O_3][H] + k_4 [NO_2][O]} \quad (42)$$

where the square brackets signify a concentration in molecules/ cm^3, and $k_1 - k_4$ are the rate constants for reactions (41.1)–(41.4), respectively. The Caltech/JPL one–dimensional photochemical model of the Martian atmosphere [*Yung et al.*, 1988] was used to evaluate these reactions for mid–latitude conditions. Model results at 40 km altitude [Hari Nair, personal communication] indicate that the chemical time constant for odd oxygen is about $t_C^{O_x} = 6120$ s = 1.7 hr. (For comparison, the photochemical lifetime of ozone based solely on photolysis is 625 s). Because the photochemical time constant is much shorter than the dynamical time constant, ozone is in a state of photochemical equilibrium. Although the circulation may affect the ozone distribution indirectly, through the effects of temperature or by altering the concentration of water vapor (to which ozone is strongly coupled), it does not have a direct impact.

There are atmospheric constituents, such as CO, whose distributions are controlled by dynamics. The only loss mechanism of significance for CO in the Martian atmosphere is the reaction:

$$CO + OH \rightarrow CO_2 + H\,. \quad (43)$$

The chemical lifetime for CO, which is derived in a manner similar to that of equation (42), is $t_C^{CO} = 2.8 \times 10^7$ s $\sim$ 320 days. CO is therefore sufficiently long–lived to be thoroughly mixed by atmospheric motions. This result is in agreement with microwave observations, which indicate uniform CO volume mixing ratios [*Clancy et al.*, 1990].

A similar comparison can be undertaken for airborne dust, although in this case the only removal process is gravitational settling. Following *Conrath* [1975], the terminal velocity, w_T, of the dust particles is given by the Stokes–Cunningham relation

for spherical particles for the case where the molecular mean free path, λ, is large compared to the particle diameter, d:

$$w_T = \left[\frac{\rho_d\, g\, d^2}{18\eta}\right]\left[1 + \frac{2}{d}\left(\lambda_r \frac{p_r}{p}\right)\right]. \tag{44}$$

The following values are assumed: dust particle density $\rho_d = 3\times10^3$ kg/m^3, molecular viscosity $\eta = 1.5 \times 10^{-5}$ kg/m/s, and reference pressure $p_r = 25$ mbar at which $\lambda_r = 2.2 \times 10^{-6}$ m. Once the velocity at which the particles are falling has been calculated for given values of d and p, the characteristic settling time is found by:

$$t_S = \frac{H}{w_T}. \tag{45}$$

Conrath [1975] deduces a mean particle diameter of approximately 2 μm for the suspended dust. The characteristic settling time for a 2 μm particle at 1 mbar is $t_S \sim 12$ days. The fact that the settling time is comparable to the timescale for vertical advection implies that the dust is well mixed. Any 2 μm dust particles entrained by local dust storms at 1 mbar ($\sim$ 18 km, which is the upper limit on the local dust cloud height inferred by *Peterfreund and Kieffer* [1979]) have a residence time sufficiently long to allow for horizontal transport. Assuming the dust remains suspended for 12 days and 1 m/s is a representative meridional velocity, the dust particles would be transported 1000 km, or approximately one–fifth of the distance between the equator and the pole. In contrast, the characteristic settling time for a 5 μm particle varies from $t_S \sim 5$ days at 1 mbar, to $t_S \sim 13$ days at 3 mbar ($\sim$ 6.5 km). The ascending motion in the non–perturbed atmosphere, after the dissipation of the dust storm, is not intense enough to support dust particles of this size over large vertical extent.

Water vapor is also an important trace species in the Martian atmosphere. *Haberle and Jakosky* [1990] argue that the absence of widespread optically thick clouds and precipitation implies that the residence time for atmospheric water vapor is long, on the order of several weeks. Because this is somewhat longer than the

dynamical time scales, the water vapor should be well–mixed in the atmospheric regions below the condensation level. Recent ground–based observations of the 1.35 cm water emission line for $L_S = 344°$ [*Clancy et al.*, 1992] indicate that water vapor is uniformly distributed in altitude up to 20 km. Above 20 km it decreases rapidly, possibly due to the effects of saturation and ice particle fallout.

The largest known active reservoir of water on Mars is the north polar cap. The strong latitudinal gradient of water from north to south may be associated with a diffusion of vapor to the south [*Jakosky and Farmer*, 1982]. Previous models of the exchange of water with the regolith and with the polar caps [*Jakosky*, 1983b] have utilized a purely diffusive transport formulation. However, the advective meridional circulation (Figure 10a) could produce an equatorward transport of water from the north polar cap at low atmospheric levels. In addition, transport by the large–scale circulation at higher atmospheric levels may oppose the effects of diffusion, which can only act to move water down the gradient of total column abundance.

Haberle and Jakosky [1990] explore the possibility that the permanent north polar cap acts as the sole source for the increased atmospheric water vapor observed in the northern hemisphere during northern spring. Through two–dimensional transport simulations they show that additional sources of water vapor, such as the low–latitude regolith, are necessary to explain the observations. The amount of adsorbed water in the regolith which can diffuse into the atmosphere is a function of the abundance and vertical distribution of the water already present in the atmosphere. *Haberle and Jakosky* propose that the ascending branch of the atmospheric circulation could act to redistribute the water vapor such that the surface layer is extremely dry, and the mixing ratio actually increases with height in the lower atmosphere. This drying of the surface layer would force additional water out of the regolith. In the northern tropics, the redistributed water would be transported poleward by the high–

altitude meridional winds. This would lead to an enhancement of water vapor over the high northern latitudes, where the winds blow downward. This process could provide a high–altitude supply of water vapor for the condensate hazes — the so–called "polar hood" — seen persistently at latitudes northward of 45° N between the northern autumnal and vernal equinoxes [*Leovy et al.*, 1972; *Briggs and Leovy*, 1974; *Christensen and Zurek*, 1984]. The winter polar cap cannot be the source for the polar hood water vapor because the winds are directed downward at these latitudes during this season.

We can roughly estimate the magnitude of the transport of water back to the north polar cap by the meridional circulation. The value of the integrated mass flux across the 20° N latitude line (see Figure 10c) for the region in which $\overline{v}^*$ is positive, but which is below the level where condensation is initiated ($\sim$ 20 km, from *Clancy et al.* [1992]), is 4.2×10^9 kg/s. The return flow at this latitude, in the region in which $\overline{v}^*$ is negative, has an integrated mass flux of 2.3×10^9 kg/s. Thus the net flux across the 20° N latitude line is 1.9×10^9 kg/s in the poleward direction. A typical low–latitude column abundance of water for $L_S = 345°$ is 10 pr μm [*Jakosky and Farmer*, 1982], which is equivalent to 10^{-3} g(H_2O)/ cm^2 [*Jakosky*, 1985]. This leads to a mass mixing ratio $r = 6 \times 10^{-5}$. The flux of water vapor is therefore 1.2×10^5 kg/s, or $\sim 1.8 \times 10^{12}$ kg in one Martian season (one quarter of a Martian year of 687 days). The total amount of water that appears in the northern hemisphere after exposure of the residual cap is 7×10^{11} kg [*Haberle and Jakosky*, 1990]. There are several possible reasons why the estimate of the northward transport of water vapor exceeds the total observed amount. First, the strength of the meridional circulation diagnosed for this interval may not be sustained throughout the entire season. Second, some of the water vapor may condense out to form ice, and some of the ice may fall out as "snow", as proposed by *Kahn* [1990].

Kahn [1990] suggests that the thin hazes observed in Viking Orbiter limb images provide a mechanism for scavenging water vapor and accumulating it into ice particles. During northern summer, when the atmospheric water vapor mixing ratios are largest, a significant fraction of the ice particles grow large enough to precipitate out as a late–season snow. This process may be responsible for drying out upper atmospheric layers and moving water closer to the surface, improving the efficiency of adsorption and ice deposit formation in the regolith. *Kahn* assumes no advective loss of vapor or ice and finds that the amount of water supplied to the regolith in the low northern latitudes by this process is roughly equal to the observed springtime increase.

We can formulate a scenario which incorporates the hypotheses of both *Haberle and Jakosky* [1990] and *Kahn* [1990], and helps to explain the maintenance of the polar hood. Water vapor desorbed from the low–latitude regolith during late northern winter/early northern spring is pumped up to higher altitudes by the ascending branch of the meridional circulation. The water will freeze out to form ice particles, some of which might grow large enough to precipitate out. However, because the atmosphere is very dry at this season, particle growth is inhibited at high altitudes. Smaller particles remain suspended in the atmosphere, and are transported by the high–altitude meridional winds into the polar regions, where they contribute to the formation of the polar hood.

Although this study has yielded insight into the magnitude and direction of atmospheric transport processes on Mars, it does not provide a complete picture of the circulation patterns. The data subset investigated in this study represents only one 12–day interval during late southern summer. Even if all available spectra had been processed, the entire Mariner 9 data set encompasses only two Martian seasons. A more comprehensive examination of the meridional circulation over an annual cycle

must await data from the Mars Observer mission, which is scheduled to launch in the fall of 1992.

5. Summary

We have presented diagnostic methods for defining the circulation of the atmosphere from a knowledge of its thermal structure. We have used diurnal averages of the meridional–plane cross–sections of atmospheric temperature and dust optical depth retrieved from Mariner 9 IRIS thermal emission spectra for a twelve–day interval in late southern summer ($L_S = 343° - 348°$). The retrieval methods and the resulting global maps of temperature and dust optical depth are described in *Santee and Crisp* [1992]. Solar heating and thermal cooling rates are computed from these temperature and dust distributions using a radiative transfer model [*Crisp*, 1990] which accounts for absorption, emission, and multiple scattering by particles and non–grey gases.

Absorption of sunlight by atmospheric dust dominates the solar heating rates. The CO_2 15 μm band produces the majority of the cooling at most levels, but airborne dust particles also contribute significantly to the near–surface cooling rates. Large net radiative heating rates (up to 8 K/day) are found in the equatorial region, and large net radiative cooling rates (up to 20 K/day) are found in the polar regions.

Zonal–mean zonal winds are derived from the meridional gradients of the observed temperatures assuming gradient wind balance and zero surface zonal wind. Outside of the tropics in both hemispheres, the zonal winds are westerly, with intense mid–latitude jets near 50 km altitude. In the southern tropics the winds are strongly easterly at all altitudes, but there is only a small corresponding region of easterlies near 60 km in the northern tropics.

The diabatic meridional circulation is calculated from the net radiative heating rates using a diagnostic stream function model which solves for the vertical and

meridional velocities simultaneously. At this season, the circulation consists of two cells, with rising motion over the equatorial region, poleward flow in both hemispheres, sinking motion over both polar regions, and then return flow in the lowest atmospheric levels. The maximum meridional velocity is 4 m/s at about 55 km at both 20° N and 20° S latitudes. The vertical velocity field is fairly symmetric, although the winds in the winter hemisphere are stronger, with a maximum downward vertical velocity of 4 cm/s at 60 km over the north pole.

This paper presents the first estimates of the meridional circulation in the Martian atmosphere diagnosed from actual temperature observations. This diabatic circulation is qualitatively similar to that of Earth's atmosphere at a comparable season, but is generally more vigorous. It is also much more vigorous than the residual mean meridional circulation derived previously from a two–dimensional tracer transport model of the Martian atmosphere [*Moreau*, 1991]. This diabatic meridional circulation places constraints on the atmospheric transport of dust in late southern summer, during non–dust storm conditions. A comparison of characteristic settling and meridional transport times reveals that 2 μm dust particles can be transported over global scales, whereas 5 μm particles do not remain suspended in the atmosphere for periods sufficient for long–range transport.

The strong meridional circulation also has important implications for the role of atmospheric transport in the seasonal cycle of water on Mars. Water vapor desorbed from the low–latitude regolith during late northern winter and early northern spring may be blown upward by the ascending branch of this circulation. The high–altitude meridional winds may advect this water back to the polar regions. This process could provide a high–altitude source of water vapor for the formation and maintenance of the north polar hood and the replenishment of the north polar cap.

References

Anderson, E. and C. Leovy, Mariner 9 Television Limb Observations of Dust and Ice Hazes on Mars, *J. Atmos. Sci.*, *35*, 723–734, 1978.

Andrews, D. G., J. R. Holton, and C. B. Leovy, *Middle Atmosphere Dynamics*, p. 489, Academic Press, 1987.

Andrews, D. G. and M. E. McIntyre, Planetary Waves in Horizontal and Vertical Shear: The Generalized Eliassen–Palm Relation and the Mean Zonal Acceleration, *J. Atmos. Sci.*, *33*, 2031–2048, 1976.

Andrews, D. G. and M. E. McIntyre, Generalized Eliassen–Palm and Charney–Drazin Theorems for Waves on Axisymmetric Mean Flows in Compressible Atmospheres, *J. Atmos. Sci.*, *35*, 175–185, 1978.

Barnes, J. R., Time Spectral Analysis of Midlatitude Disturbances in the Martian Atmosphere, *J. Atmos. Sci.*, *37*, 2002–2015, 1980.

Barnes, J. R., Midlatitude Disturbances in the Martian Atmosphere: A Second Mars Year, *J. Atmos. Sci.*, *38*, 225–234, 1981.

Barnes, J. R., Transport of Dust to High Northern Latitudes in a Martian Polar Warming, *J. Geophys. Res.*, *95*, 1381–1400, 1990a.

Barnes, J. R., Possible Effects of Breaking Gravity Waves on the Circulation of the Middle Atmosphere of Mars, *J. Geophys. Res.*, *95*, 1401–1421, 1990b.

Barnes, J. R., A Simple Nearly Analytic Model of a Gravity Wave Driven Middle Atmosphere Circulation, *J. Atmos. Sci.*, *48*, 225–235, 1991.

Barnes, J. R. and J. L. Hollingsworth, Dynamical Modeling of a Planetary Wave Mechanism for a Martian Polar Warming, *Icarus*, *71*, 313–334, 1987.

Briggs, G. A. and C. B. Leovy, Mariner 9 Observations of the Mars North Polar

Hood, *Bull. Am. Meteor. Soc.*, *55*, 278–296, 1974.

Briggs, G. A., K. Klaasen, T. Thorpe, J. Wellman, and W. Baum, Martian Dynamical Phenomena During June–November 1976: Viking Orbiter Imaging Results, *J. Geophys. Res.*, *82*, 4121–4149, 1977.

Chamberlain, J. W. and D. M. Hunten, *Theory of Planetary Atmospheres: An Introduction to their Physics and Chemistry*, p. 481, Academic Press, 1987.

Christensen, P. R., Global Albedo Variations on Mars: Implications for Active Aeolian Transport, Deposition, and Erosion, *J. Geophys. Res.*, *93*, 7611–7624, 1988.

Christensen, P. R. and R. W. Zurek, Martian North Polar Hazes and Surface Ice: Results from the Viking Survey/Completion Mission, *J. Geophys. Res.*, *89*, 4587–4596, 1984.

Clancy, R. T., A. W. Grossman, and D. O. Muhleman, VLA Mapping of 1.35 cm Water Emission from the Mars Atmospheric Limb, Paper presented at the *Workshop on the Martian Surface and Atmosphere through Time*, Boulder, CO, 1992.

Clancy, R. T., D. O. Muhleman, and G. L. Berge, Global Changes in the 0–70 km Thermal Structure of the Mars Atmosphere Derived from 1975 to 1989 Microwave CO Spectra, *J. Geophys. Res.*, *95*, 14,543–14,554, 1990.

Conrath, B. J., Thermal Structure of the Martian Atmosphere during the Dissipation of the Dust Storm of 1971, *Icarus*, *24*, 36–46, 1975.

Conrath, B. J., Planetary–Scale Wave Structure in the Martian Atmosphere, *Icarus*, *48*, 246–255, 1981.

Crisp, D. (1983). *Radiative Forcing of the Venus Mesosphere* Ph.D. Thesis, Princeton University.

Crisp, D., Radiative Forcing of the Venus Mesosphere. I. Solar Fluxes and Heating Rates, *Icarus*, *67*, 484–514, 1986.

Crisp, D., Radiative Forcing of the Venus Mesosphere. II. Thermal Fluxes, Cooling Rates, and Radiative Equilibrium Temperatures, *Icarus*, *77*, 391–413, 1989.

Crisp, D., Infrared Radiative Transfer in the Dust–Free Martian Atmosphere, *J. Geophys. Res.*, *95*, 14,577–14,588, 1990.

Deming, D., M. J. Mumma, F. Espenak, and T. Kostiuk, Polar Warming in the Middle Atmosphere of Mars, *Icarus*, *66*, 366–379, 1986.

Drossart, P., J. Rosenqvist, S. Erard, Y. Langevin, J.–P. Bibring, and M. Combes, Martian Aerosol Properties from the Phobos ISM Experiment, *Ann. Geophys.*, *9*, 754–760, 1991.

Dunkerton, T., On the Mean Meridional Mass Motions of the Stratosphere and Mesosphere, *J. Atmos. Sci.*, *35*, 2325–2333, 1978.

Dunkerton, T., A Lagrangian Mean Theory of Wave, Mean–Flow Interaction With Applications to Nonacceleration and Its Breakdown, *Rev. Geophys. Space Phys.*, *18*, 387–400, 1980.

Farmer, C. B. and P. E. Doms, Global Seasonal Variation of Water Vapor on Mars and the Implications for Permafrost, *J. Geophys. Res.*, *84*, 2881–2888, 1979.

French, R. G., P. J. Gierasch, B. D. Popp, and R. J. Yerdon, Global Patterns in Cloud Forms on Mars, *Icarus*, *45*, 468–493, 1981.

Gille, J. C., L. V. Lyjak, and A. K. Smith, The Global Residual Mean Circulation in the Middle Atmosphere for the Northern Winter Period, *J. Atmos. Sci.*, *44*, 1437–1452, 1987.

Goody, R. M. and Y. L. Yung, *Atmospheric Radiation: Theoretical Basis*, p. 519, Oxford University Press, 1989.

Haberle, R. M., C. B. Leovy, and J. B. Pollack, A Numerical Model of the Martian Polar Cap Winds, *Icarus*, *39*, 151–183, 1979.

Haberle, R. M., C. B. Leovy, and J. B. Pollack, Some Effects of Global Dust Storms on the Atmospheric Circulation of Mars, *Icarus*, *50*, 322–367, 1982.

Haberle, R. M. and B. M. Jakosky, Sublimation and Transport of Water from the North Residual Polar Cap on Mars, *J. Geophys. Res.*, *95*, 1423–1437, 1990.

Haberle, R. M., J. B. Pollack, J. R. Barnes, R. W. Zurek, C. B. Leovy, J. R. Murphy, H. Lee, and J. Schaeffer, Mars Atmospheric Dynamics as Simulated by the NASA/Ames General Circulation Model: I. The Zonal–Mean Circulation, Submitted to *J. Geophys. Res.*, 1992.

Haltiner, G. J. and R. T. Williams, *Numerical Prediction and Dynamic Meteorology*, p. 477, John Wiley and Sons, 1980.

Hantel, M. and H.–R. Baader, Diabatic Heating Climatology of the Zonal Atmosphere, *J. Atmos. Sci.*, *35*, 1180–1189, 1978.

Hess, S. L., R. M. Henry, C. B. Leovy, J. A. Ryan, and J. E. Tillman, Meteorological Results From the Surface of Mars: Viking 1 and 2, *J. Geophys. Res.*, *82*, 4559–4574, 1977.

Hess, S. L., R. M. Henry, and J. E. Tillman, The Seasonal Variation of Atmospheric Pressure on Mars as Affected by the South Polar Cap, *J. Geophys. Res.*, *84*, 2923–2927, 1979.

Hitchman, M. H. and C. B. Leovy, Evolution of the Zonal Mean State in the Equatorial Middle Atmosphere during October 1978 – May 1979, *J. Atmos. Sci.*, *43*, 3159–3176, 1986.

Holton, J. R., *An Introduction to Dynamic Meteorology*, p. 391, Academic Press, 1979.

Holton, J. R., The Influence of Gravity Wave Breaking on the General Circulation of the Middle Atmosphere, *J. Atmos. Sci.*, *40*, 2497–2507, 1983.

Holton, J. R. and W. M. Wehrbein, A Numerical Model of the Zonal Mean Circulation of the Middle Atmosphere, *Pure Appl. Geophys.*, *118*, 285–306, 1980.

Hsu, C.–P., Air Parcel Motions during a Numerically Simulated Sudden Stratospheric Warming, *J. Atmos. Sci.*, *37*, 2768–2792, 1980.

Hunt, B. G. and Manabe, S., Experiments with a Stratospheric General Circulation Model: II. Large–Scale Diffusion of Tracers in the Stratosphere, *Mon. Wea. Rev.*, *96*, 503–539, 1968.

Jakosky, B. M., The Role of Seasonal Reservoirs in the Mars Water Cycle: I. Seasonal Exchange of Water with the Regolith, *Icarus*, *55*, 1–18, 1983a.

Jakosky, B. M., The Role of Seasonal Reservoirs in the Mars Water Cycle: II. Coupled Models of the Regolith, the Polar Caps, and Atmospheric Transport, *Icarus*, *55*, 19–39, 1983b.

Jakosky, B. M., The Seasonal Cycle of Water on Mars, *Space Sci. Rev.*, *41*, 131–200, 1985.

Jakosky, B. M. and C. B. Farmer, The Seasonal and Global Behavior of Water Vapor in the Mars Atmosphere: Complete Global Results of the Viking Atmospheric Water Detector Experiment, *J. Geophys. Res.*, *87*, 2999–3019, 1982.

James, P. B., The Martian Hydrologic Cycle: Effects of CO_2 Mass Flux on Global Water Distribution, *Icarus*, *64*, 249–264, 1985.

James, P. B., The Role of Water Ice Clouds in the Martian Hydrologic Cycle, *J. Geophys. Res.*, *95*, 1439–1445, 1990.

Joseph, J. H., W. J. Wiscombe, and J. A. Weinman, The Delta–Eddington Approximation for Radiative Flux Transfer, *J. Atmos. Sci.*, *33*, 2452–2459, 1976.

Kahn, R., Some Observational Constraints on the Global–Scale Wind Systems of Mars, *J. Geophys. Res.*, *88*, 10,189–10,209, 1983.

Kahn, R., Ice Haze, Snow, and the Mars Water Cycle, *J. Geophys. Res.*, *95*, 14,677–14,693, 1990.

Kieffer, H. H., Mars South Polar Spring and Summer Temperatures: A Residual CO_2 Frost, *J. Geophys. Res.*, *84*, 8263–8288, 1979.

King, M. D. and Harshvardhan, Comparative Accuracy of the Albedo, Transmission and Absorption for Selected Radiative Transfer Approximations, NASA Technical Note 1160, Goddard Space Flight Center, 1986.

Kong, T. Y. and M. B. McElroy, Photochemistry of the Martian Atmosphere, *Icarus*, *32*, 168–189, 1977.

Lacis, A. A. and J. E. Hansen, A Parameterization for the Absorption of Solar Radiation in the Earth's Atmosphere, *J. Atmos. Sci.*, *31*, 118–133, 1974.

Lellouch, E., J. J. Goldstein, S. W. Bougher, G. Paubert, and J. Rosenqvist, First Absolute Wind Measurements in the Middle Atmosphere of Mars, *Astrophys. J.*, *383*, 401–406, 1991.

Leovy, C. B., Simple Models of Thermally Driven Mesospheric Circulation, *J. Atmos. Sci.*, *21*, 327–341, 1964.

Leovy, C. B., Martian Meteorological Variability, *Adv. Space Res.*, *2*, 19–44, 1982.

Leovy, C. B., G. A. Briggs, A. T. Young, B. A. Smith, J. B. Pollack, E. N. Shipley, and R. L. Wildey, The Martian Atmosphere: Mariner 9 Television Experiment Progress Report, *Icarus*, *17*, 373–393, 1972.

Mahlman, J. D., D. G. Andrews, D. L. Hartmann, T. Matsuno, and R. G. Murgatroyd, Transport of Trace Constituents in the Stratosphere , In *Dynamics of the Middle Atmosphere* , J. R. Holton and T. Matsuno (ed.), 387–416, 1984.

Marks, C. J., Some Features of the Climatology of the Middle Atmosphere Revealed by Nimbus 5 and 6, *J. Atmos. Sci.*, *46*, 2485–2508, 1989.

Martin, T. Z., Thermal Infrared Opacity of the Martian Atmosphere, *Icarus*, *66*, 2–21, 1986.

Matsuno, T., Lagrangian Motion of Air Parcels in the Stratosphere in the Presence of Planetary Waves, *Pure Appl. Geophys.*, *118*, 188–216, 1980.

Meador, W. E. and W. R. Weaver, Two–Stream Approximations to Radiative Transfer in Planetary Atmospheres: A Unified Description of Existing Methods and a New Improvement, *J. Atmos. Sci.*, *37*, 630–643, 1980.

Michelangeli, D. V., R. W. Zurek, and L. S. Elson, Barotropic Instability of Midlatitude Zonal Jets on Mars, Earth, and Venus, *J. Atmos. Sci.*, *44*, 2031–2041, 1987.

Moreau, D., L. W. Esposito, and G. Brasseur, The Chemical Composition of the Dust–Free Martian Atmosphere: Preliminary Results of a Two–Dimensional Model, *J. Geophys. Res.*, *96*, 7933–7945, 1991.

Murgatroyd, R. J. and F. Singleton, Possible Meridional Circulations in the Stratosphere and Mesosphere, *Quart. J. Roy. Meteorol. Soc.*, *87*, 125–135, 1961.

Peterfreund, A. R. and H. H. Kieffer, Thermal Infrared Properties of the Martian Atmosphere: 3. Local Dust Clouds, *J. Geophys. Res.*, *84*, 2853–2863, 1979.

Pollack, J. B., Properties of Dust in the Martian Atmosphere and its Effect on Temperature Structure, *Adv. Space Res.*, *2*, 45–56, 1982.

Pollack, J. B., D. Colburn, R. Kahn, J. Hunter, W. Van Camp, C. E. Carlston, and M. R. Wolf, Properties of Aerosols in the Martian Atmosphere, as Inferred from Viking Lander Imaging Data, *J. Geophys. Res.*, *82*, 4479–4495, 1977.

Pollack, J. B., D. S. Colburn, F. M. Flasar, R. Kahn, C. E. Carlston, and D. Pidek, Properties and Effects of Dust Particles Suspended in the Martian Atmosphere, *J. Geophys. Res.*, *84*, 2929–2945, 1979.

Pollack, J. B., C. B. Leovy, P. W. Greiman, Y. Mintz, A Martian General Circulation Experiment with Large Topography, *J. Atmos. Sci.*, *38*, 3–29, 1981.

Pollack, J. B., R. M. Haberle, J. Schaeffer, and H. Lee, Simulations of the General Circulation of the Martian Atmosphere: 1. Polar Processes, *J. Geophys. Res.*, *95*, 1447–1473, 1990.

Press, W. H., B. P. Flannery, S. A. Teukolsky, and W. T. Vetterling, *Numerical Recipes: The Art of Scientific Computing*, p. 702, Cambridge University Press, 1989.

Reiter, E. R., Stratospheric–Tropospheric Exchange Processes, *Rev. Geophys. Space Phys.*, *13*, 459–474, 1975.

Rosenfield, J. E., M. R. Schoeberl, and M. A. Geller, A Computation of the Stratospheric Diabatic Circulation Using an Accurate Radiative Transfer Model, *J. Atmos. Sci.*, *44*, 859–876, 1987.

Rothermel, H., H. U. Käufl, U. Schrey, and S. Drapatz, Thermal Structure of the Martian Mesosphere, *Astron. Astrophys.*, *196*, 296–300, 1988.

Roush, T., J. Pollack, and J. Orenberg, Derivation of Midinfrared (5–25 μm) Optical Constants of Some Silicates and Palagonite, *Icarus*, *94*, 191–208, 1991.

Ryan, J. A., R. M. Henry, S. L. Hess, C. B. Leovy, J. E. Tillman, and C. Walcek, Mars Meteorology: Three Seasons at the Surface, *Geophys. Res. Lett.*, *5*, 715–718, 1978.

Ryan, J. A. and R. M. Henry, Mars Atmospheric Phenomena During Major Dust Storms, as Measured at Surface, *J. Geophys. Res.*, *84*, 2821–2829, 1979.

Ryan, J. A. and R. D. Lucich, Possible Dust Devils, Vortices on Mars, *J. Geophys. Res.*, *88*, 11,005–11,011, 1983.

Santee, M. and D. Crisp, The Thermal Structure and Dust Loading of the Martian

Atmosphere During Late Southern Summer: Mariner 9 Revisited, Submitted to *J. Geophys. Res.*, 1992.

Sharman, R. D. and J. A. Ryan, Mars Atmosphere Pressure Periodicities from Viking Observations, *J. Atmos. Sci.*, *37*, 1994–2001, 1980.

Shettle, E. P. and J. A. Weinman, The Transfer of Solar Irradiance Through Inhomogeneous Turbid Atmospheres Evaluated by Eddington's Approximation, *J. Atmos. Sci.*, *27*, 1048–1055, 1970.

Shia, R.–L., Y. L. Yung, M. Allen, R. W. Zurek, and D. Crisp, Sensitivity Study of Advection and Diffusion Coefficients in a Two–Dimensional Stratospheric Model Using Excess Carbon 14 Data, *J. Geophys. Res.*, *94*, 18,467–18,484, 1989.

Shine, K., Sources and Sinks of Zonal Momentum in the Middle Atmosphere Diagnosed Using the Diabatic Circulation, *Quart. J. Roy. Meteorol. Soc.*, *115*, 265–292, 1989.

Solomon, S., J. T. Kiehl, R. R. Garcia, and W. Grose, Tracer Transport by the Diabatic Circulation Deduced from Satellite Observations, *J. Atmos. Sci.*, *43*, 1603–1617, 1986.

Thomas, P. and P. J. Gierasch, Dust Devils on Mars, *Science*, *230*, 175–177, 1985.

Tillman, J. E., R. M. Henry, and S. L. Hess, Frontal Systems During Passage of the Martian North Polar Hood Over the Viking Lander 2 Site Prior to the First 1977 Dust Storm, *J. Geophys. Res.*, *84*, 2947–2955, 1979.

Toon, O. B., J. B. Pollack, and C. Sagan, Physical Properties of the Particles Composing the Martian Dust Storm of 1971–1972, *Icarus*, *30*, 663–696, 1977.

Touloukian, Y. S. and T. Makita, Specific Heat: Nonmetallic liquids and gases , In *Thermophysical Properties of Matter 6* , Y. S. Touloukian (ed.), 143–151, 1970.

Vincent, D. G., Mean Meridional Circulations in the Northern Hemisphere Lower

Stratosphere during 1964 and 1965, *Quart. J. Roy. Meteorol. Soc.*, *94*, 333–349, 1968.

Wallace, J. M. and P. V. Hobbs, *Atmospheric Science: An Introductory Survey*, p. 467, Academic Press, 1977.

Yang, H., K. K. Tung, and E. Olaguer, Nongeostrophic Theory of Zonally Averaged Circulation. Part II: Eliassen–Palm Flux Divergence and Isentropic Mixing Coefficient, *J. Atmos. Sci.*, *47*, 215–241, 1990.

Yung, Y. L., J.–S. Wen, J. P. Pinto, M. Allen, K. K. Pierce, and S. Paulson, HDO in the Martian Atmosphere: Implications for the Abundance of Crustal Water, *Icarus*, *76*, 146–159, 1988.

Zurek, R. W., Diurnal Tide in the Martian Atmosphere, *J. Atmos. Sci.*, *33*, 321–337, 1976.

Zurek, R. W., Martian Great Dust Storms: An Update, *Icarus*, *50*, 288–310, 1982.

Zurek, R. W. and R. M. Haberle, Zonally Symmetric Response to Atmospheric Tidal Forcing in the Dusty Martian Atmosphere, *J. Atmos. Sci.*, *45*, 2469–2485, 1988.

APPENDIX I

Quasi–Random Model

The first step in deriving Martian atmospheric temperature and dust distributions from Mariner 9 IRIS observations is to compute high–resolution atmospheric transmission spectra. The most suitable method for computing atmospheric transmittances in narrow spectral intervals for use in the IRIS retrieval algorithms is the so–called "quasi–random" model. The purpose of this Appendix is to define the concept of the atmospheric transmittance and then to describe in detail the *Crisp* [1990] quasi–random model.

In a plane–parallel, hydrostatic atmosphere, the monochromatic transmittance at wavenumber ν is given by:

$$\mathcal{T}_\nu(p) = \exp\left\{\int_p^0 k(\nu, p', T)\frac{r(p')}{g\cos\theta}dp'\right\} \tag{1}$$

where ν is the wavenumber, p is the pressure, T is the temperature, g is the gravitational acceleration, $r(p)$ is the absorbing gas mass mixing ratio, θ is the zenith angle of the radiation, and $k(\nu, p, T)$ is the total monochromatic absorption coefficient for all constituents. For absorption by gases, k is given by the sum of the k_i for all lines that absorb at ν:

$$k_i(\nu, p, T) \;=\; S_i(T)\, f_i(\nu, \nu_{0_i}, p, T) \tag{2}$$

where $S_i(T)$ is the temperature–dependent line strength and $f_i(\nu, \nu_{0_i}, p, T)$ is the line shape function of the i^{th} spectral line, which is centered at wavenumber ν_{0_i}. Spectral lines are not infinitely narrow; broadening of a line is caused by collisions between neighboring air molecules, which occur more frequently at higher pressures, and Doppler shifts arising from the thermal motion of the molecule during emission or absorption of radiation. For collisional–broadening, the line is described by the Lorentz shape function:

$$f(\nu, \nu_0, p, T) \;=\; \frac{1}{\pi}\,\frac{\alpha_L(p,T)}{(\nu-\nu_0)^2 \,+\, \alpha_L^2(p,T)} \tag{3.1}$$

$$\alpha_L(p,T) = \alpha_0 \left[\frac{p}{p_0}\right] \left[\frac{T_0}{T}\right]^{\kappa} \tag{3.2}$$

where $\alpha_L(p,T)$ is the Lorentz half–width of the line at the half maximum and α_0 is its value at $p_0 = 1$ atm and $T_0 = 296$ K. The temperature exponent κ usually has values between 0.5 and 1.0. For Doppler broadening the line shape function is given by:

$$f(\nu,\nu_0,p,T) = \frac{1}{\alpha_D(\nu,T)\sqrt{\pi}} \exp\left\{-\left(\frac{\nu-\nu_0}{\alpha_D(\nu,T)}\right)^2\right\} \tag{4.1}$$

$$\alpha_D(\nu,T) = \frac{\nu_0}{c}\sqrt{2RT} \tag{4.2}$$

where R is the mean gas constant of the atmosphere and $\alpha_D(\nu,T)\sqrt{\ln 2}$ is the Doppler half–width of the line at the half–maximum. Doppler–broadening and collisional–broadening effects are similar in magnitude in the low–pressure Martian atmosphere, and a Voigt line shape function [see, *e.g.*, *Tiwari*, 1978; *Goody and Yung*, 1989] must be used to account for their combined influence:

$$f(\nu,\nu_0,p,T) = \frac{\alpha_L(p,T)}{\alpha_D(\nu,T)\pi^{3/2}} \int_{-\infty}^{\infty} \frac{\exp\{-t^2/\alpha_D^2(\nu,T)\}}{(t-\nu+\nu_0)^2 + \alpha_L^2(p,T)}\, dt\,. \tag{5}$$

At high pressures, the quantity α_L/α_D becomes large and equation (5) reduces to the Lorentzian case. At low pressures, as α_L approaches zero, the line profile assumes a hybrid form characterized by a Doppler core with Lorentzian wings.

In the presence of multiple absorption lines, the absorption coefficient is given by the sum of all line absorption coefficients, and the total monochromatic transmittance is the product of the transmittances of the individual lines [*Burch et al.*, 1956; *Goody and Yung*, 1989]:

$$\mathcal{T}_\nu(p) = \prod_{i=1}^{N} \exp\left\{\int_p^0 k_i(\nu,p',T)\frac{r(p')}{g\cos\theta}dp'\right\}\,. \tag{6}$$

N is the total number of lines contributing to absorption at this wavenumber, and $k_i(\nu,p,T)$ is the absorption coefficient of the i^{th} absorption line. For a finite spectral

interval of width $\Delta\nu$, the average gas transmittance $\mathcal{T}(\Delta\nu, p)$ is defined by:

$$\mathcal{T}(\Delta\nu, p) = \frac{1}{\Delta\nu} \int_{-\Delta\nu/2}^{\Delta\nu/2} \prod_{i=1}^{N} \exp\left\{ \int_{p}^{0} k_i(\nu, p', T) \frac{r(p')}{g \cos\theta} \, dp' \right\} d\nu \,. \tag{7}$$

The most versatile and accurate approach to solving equation (7) is a straightforward numerical integration over the spectrum. This method, called a line–by–line model, is advantageous because it can incorporate all available information about the spectral line strengths, shapes, and positions into the transmittance calculation. It can explicitly account for both the changes in the absorbing gas mass mixing ratio along the atmospheric optical path and the effects of varying pressures and temperatures on the line strengths and widths. The accuracy of the line–by–line model is therefore primarily limited by the uncertainties in the absorption line parameters. Its chief disadvantage lies in the fact that the absorption spectrum must be divided into a sufficiently large number of spectral intervals such that the narrow cores of individual lines are completely resolved, and the transmittance must be computed in each of these intervals. Because the CO_2 15 μm band encompasses nearly 20,000 spectral lines, some of which require intervals less than 10^{-4} cm^{-1} wide to be resolved [*Crisp et al.*, 1986], the line–by–line model is extremely computationally expensive. It is therefore impractical to use a line–by–line model in this application because the transmittances must be recomputed several times for each spectrum to account for changes in the temperature profile, and our data subset includes more than 2000 spectra.

There are several more efficient approximate methods, employing a variety of simplifying assumptions about the structure of the CO_2 15 μm band, which can be used to calculate atmospheric transmittances more rapidly than the line–by–line model. The so–called "quasi–random" model [*Wyatt et al.*, 1962] was designed to divide the entire band into a series of finite intervals, which are narrow enough to

resolve the band shape, as well as its total absorption. Because the spectral lines are localized in intervals that are small compared to the width of the band, the wavelength dependence of the band strength can be accounted for accurately. The fact that there are thousands of lines of finite width within an absorption band implies that there must be many overlapping lines. The basic premise behind the quasi–random model is that the effects of line overlap can be accounted for by assuming that the line centers are distributed randomly within each narrow spectral interval $\Delta\nu$. That is, the probability of any line being centered at a particular wavenumber is independent of the probability that any other line is centered at any other wavenumber. Because the line positions are assumed to be uncorrelated in wavenumber within this interval, the order of the product and the integral over ν in equation (7) can be reversed, yielding:

$$\mathcal{T}(\Delta\nu, p) = \prod_{i=1}^{N} \frac{1}{\Delta\nu} \int_{-\Delta\nu/2}^{\Delta\nu/2} \exp\left\{ \int_{p}^{0} k_i(\nu, p', T) \frac{r(p')}{g \cos\theta} \, dp' \right\} d\nu$$

$$= \prod_{i=1}^{N} \mathcal{T}_i(\Delta\nu, p) \tag{8}$$

where $\mathcal{T}_i$ is the transmittance for spectral line i. Thus the transmittance is evaluated separately for each line, and the overlap between lines is accounted for by taking the product of the contributions from the individual lines. The assumption of random line spacing is applied only within the finite intervals and not to the entire band, and therefore the model is considered "quasi–random." If the transmittance over a broader spectral range, or over the entire band, is needed, it is calculated by averaging the results for all of the finite intervals contained within the desired range. In *Santee and Crisp* [1992], the transmittances were calculated by dividing the spectral region occupied by the CO_2 15 μm band (450–900 cm^{-1}) into about 1200 intervals, each about 0.39 cm^{-1} wide. The transmittance in 1.18 cm^{-1} intervals, corresponding to the spectral sampling of the IRIS instrument, was then determined by averaging

the higher–resolution transmittance results using a Hamming window apodization function with a full–width at half–maximum of 2.4 cm^{-1} [*Hanel et al.*, 1980].

The number of lines in each spectral interval (N) and the values for several line parameters (S, α_D, α_L, etc.) are required to evaluate equation (8) (see equations (2) and (5)). For this study, these quantities were obtained from the 1986 edition of the AFGL HITRAN database of atmospheric absorption line parameters [*Rothman et al.*, 1987]. In a realistic inhomogeneous atmosphere, the pressure and temperature vary with height, causing associated variations in line half–width and strength. In the quasi–random model, these variations are accounted for through the explicit numerical integration of equation (8).

Because equation (8) must be evaluated for each line in the spectral interval, this model is still computationally expensive for spectral regions where there are many lines. To reduce the number of integrations, lines with similar strengths can be binned into line groups [*Wyatt et al.*, 1962]. A given line group then includes all lines with strengths between S and $S + dS$. Equation (8) is then evaluated only once for each line group, and the transmittance can be expressed as:

$$\mathcal{T}(\Delta\nu, p) = \prod_{j=1}^{J} \left[\mathcal{T}_j(\Delta\nu, p)\right]^{n_j} \tag{9}$$

where n_j is the number of lines in the jth line strength group and J is the number of line strength groups in the spectral interval $\Delta\nu$. $\mathcal{T}_j$ is the transmittance corresponding to the mean line strength and line width of the jth group.

The accuracy of the quasi–random model depends crucially on how well the line strength groups represent the actual line strength distribution in each finite interval. There are several possible ways to resolve the line strength distribution. The simplest approach is for all lines within the band to be allocated into a single set of line strength groups. The transmittance is then calculated only once for each line strength group,

and the group value is used in any finite interval in which a member of that group is present. A disadvantage of this approach is that a large number of line groups is necessary to accommodate the wide range of line strengths and line half–widths that characterize most bands. In addition, lines far from the band center have a much greater temperature–dependence than lines near the band center. If the line strength groups are defined over the entire band, lines from regions both close to and far from the band center may be placed in the same line strength group. Alternatively, the line population in each narrow interval can be apportioned into a small number of line–strength groups. In practice, this method resolves the spectrally–dependent variations in line strengths and half–widths, and their temperature dependence, better than the whole–band grouping approach, but it usually produces even more line strength groups. There is a tradeoff between accuracy and efficiency, because the speed of the quasi–random model decreases as the number of line strength groups increases.

For this study we adopted a hybrid line–grouping algorithm [*Crisp*, 1990] that features the principal assets of both of these methods. The band is divided into both "major" and "minor" intervals. The major intervals are chosen (arbitrarily) to be 1.18 cm^{-1} wide, corresponding to the sampling of the IRIS data, while the minor intervals are 0.39 cm^{-1} wide. Thus there are three minor intervals per major interval. The line strength population in each 1.18 cm^{-1} major interval is sorted into as many as ten line strength groups, which are roughly equally–spaced in the log of the line strength. The effective line strength, S_j, and half–width, α_j, for each group is obtained by averaging the strengths and half–widths of all lines in the group, and these values are used to compute the mean transmittance for that group throughout the atmospheric column. The group mean transmittance is then distributed to all intervals which include lines represented by that group. The total number of lines in

the interval, N, equals:

$$N = \sum_{j=1}^{J} n_j \,. \tag{10}$$

The actual number n_j of spectral lines in any particular wavenumber interval and line strength group is used to calculate the transmittance. Equation (9) is therefore equally valid for only a single line or a large number of lines.

Quasi–random models explicitly account for the transmittance within each finite interval by lines centered both within and outside of the interval. This approach produces more accurate transmittance estimates in spectral regions with rapidly–varying line populations. This is achieved by separating the transmittance within any spectral interval $\Delta\nu$ into two components. The direct contribution to the transmittance in interval $\Delta\nu$, $\mathcal{T}^D$, comes from lines whose centers are located within $\Delta\nu$, whereas the wing contribution to the transmittance in interval $\Delta\nu$, $\mathcal{T}^W$, comes from lines whose centers are located outside of $\Delta\nu$:

$$\mathcal{T}(\Delta\nu, p) = \prod_{l=1}^{N_D} \mathcal{T}_l^D(\Delta\nu, p) \cdot \prod_{k=1}^{N_W} \mathcal{T}_k^W(\Delta\nu, p) \,. \tag{11}$$

To find the direct contribution, $\mathcal{T}^D(\Delta\nu, p)$, from a spectral line, the line is assumed to be positioned at $\nu = 0$, centered within $\Delta\nu$. The *Wyatt et al.* [1962] quasi–random model used a simple analytic line shape function. However, the *Crisp* [1990] quasi–random model employs a true Voigt line shape function, and as a consequence the line transmittance must be determined by numerically integrating over the line profile and the optical path (see equation (8)). The integration over wavenumber in equation (8) is divided into line–core, near–wing, and far–wing segments, and different numerical methods are used to calculate the transmittances in each segment. The transmittance by a single line is then given by the sum of the core and wing components:

$$\mathcal{T}^D(\Delta\nu, p) = \mathcal{T}^c + \mathcal{T}^{nw} + \mathcal{T}^{fw} \,. \tag{12}$$

The line core is defined as that part of the line between the line center and a cut-off wavenumber, ν_c, which is taken to be twice the Doppler half-width from the line center. At distances less than ν_c, the line is assumed to follow a Voigt profile, and the rational approximation to the Voigt line shape function described by *Humlíček* [1982] is used at all levels of the atmosphere. Four-point Gaussian quadrature is used to calculate transmittances in the line-core region, where the line shape function changes very rapidly with wavenumber. The near wing region is defined as that part of the line between ν_c and a second cut-off wavenumber, ν_n, which is about 40 Doppler half-widths from the line center and the point beyond which Voigt effects are no longer important. In the near-wing region between ν_c and ν_n, the Voigt line shape function is also used. Because the line shape function is still varying significantly, the integration is performed using an unequally-spaced trapezoid scheme with the grid spacing increasing with distance from the line center. The far wing region is defined as that part of the line between ν_n and the edge of the interval, $\Delta\nu/2$. The Lorentz profile is used between ν_n and a distance about 5 times the maximum Lorentz half-width encountered along the path. Beyond this point, the line profile is assumed to follow a simplified "far-wing Lorentzian" shape, where the α_L^2 term in the denominator (see equation (3.1)) can be neglected because the $(\nu - \nu_0)^2$ term predominates. With this assumption the transmittance can be evaluated analytically in terms of error functions.

To calculate $\mathcal{T}^W(\Delta\nu, p)$, the transmittance within $\Delta\nu$ from lines centered outside of the interval, two simplifications are made. The first assumes that the far wings of lines from nearby intervals also follow a "far-wing Lorentzian" shape. This assumption is valid as long as $\Delta\nu/2$ is much greater than the Lorentz and Doppler half-widths. The second assumes that each contributing line is centered within the interval in which it is located. This assumption should also be valid as long as $\Delta\nu/2$

is much greater than the Lorentz half–width. With these assumptions, the total absorption within $\Delta\nu$ by all lines outside of this interval is given by:

$$\mathcal{T}^W(\Delta\nu, p) = \prod_{k=1}^{K} \left\{ \prod_{i=1}^{N} \mathcal{T}_i^W(\Delta\nu, p, k) \right\} \tag{13}$$

where $\mathcal{T}_i^W(\Delta\nu, p, k)$ is the contribution within $\Delta\nu$ by a line centered between ν_k and ν_{k+1}. This explicit treatment of lines both within and outside of each interval increases the complexity and decreases the speed of the quasi–random model, but vastly improves its accuracy for high–resolution spectra like those collected by IRIS.

The accuracy of the quasi–random model was demonstrated in *Crisp* [1990], where transmission and brightness temperature spectra from this model were compared to those from a line–by–line model for a spectral region encompassing the CO_2 15 μm band. The results indicated that the quasi–random model rarely introduced transmittance or radiance errors larger than one percent except in the narrow Q branches of the ν_2 fundamental and nearby hot bands, which are not completely resolved by the spectral grid. The quasi–random model proved to be 100–1000 times faster than the line–by–line model at performing the same transmittance calculation. This speed is essential because the IRIS retrieval algorithms require that the transmittances be recomputed often to account for variations in atmospheric temperatures, which produce large variations in the strengths of lines in the far wings of the 15 μm band.

In summary, the quasi–random model has the following characteristics: (1) it accurately represents the distribution of spectral lines within a band; *i.e.*, it does not require the lines to be either randomly or uniformly spaced, (2) it accurately simulates the intensity distribution of the spectral lines, including even very weak lines, which can contribute significantly to absorption along paths at low pressures [*Crisp et al.*, 1986], (3) it accurately assesses the wing contribution to the transmittance from spectral lines whose centers lie outside the given wavenumber interval, so that it can

produce reliable results in spectral regions with rapidly–varying line strengths, (4) it accurately accounts for variations in the line strength and width along inhomogeneous atmospheric optical paths (through the explicit integration of equation (8)), (5) it makes no *ad–hoc* assumptions about either the spectral interval width or the number of lines within the interval, and (6) it uses an accurate representation of the Voigt line shape function, which is essential for applications in the thin Martian atmosphere. These attributes, combined with its relative speed, make the quasi–random model the most suitable means available for calculating atmospheric transmittances for use in Martian atmospheric temperature and dust retrievals.

References

Burch, D. E., J. N. Howard, and D. Williams, Infrared Transmission of Synthetic Atmospheres: V. Absorption Laws for Overlapping Bands, *J. Opt. Soc. Am.*, *46*, 452–455, 1956.

Crisp, D., Infrared Radiative Transfer in the Dust–Free Martian Atmosphere, *J. Geophys. Res.*, *95*, 14,577–14,588, 1990.

Crisp, D., S. B. Fels, and M. D. Schwarzkopf, Approximate Methods for Finding CO_2 15 μm Band Transmission in Planetary Atmospheres, *J. Geophys. Res.*, *91*, 11,851–11,866, 1986.

Goody, R. M. and Y. L. Yung, *Atmospheric Radiation: Theoretical Basis*, p. 519, Oxford University Press, 1989.

Hanel, R., L. Herath, V. Kunde, and J. Pearl, Voyager infrared interferometer spectrometer and radiometer (IRIS) – Documentation for reduced data records (RDR) for Jupiter, NASA Technical Note X-693-821-8, Goddard Space Flight Center, 1980.

Humlíček, J., Optimized Computation of the Voigt and Complex Probability Functions, *J. Quant. Spectrosc. Radiat. Transf.*, *27*, 437–444, 1982.

Rothman, L. S., R. R. Gamache, A. Goldman, L. R. Brown, R. A. Toth, H. M. Pickett, R. L. Poynter, J.–M. Flaud, C. Camy–Peyret, A. Barbe, N. Husson, and M. A. H. Smith, The HITRAN database: 1986 edition, *Applied Optics*, *26*, 4058–4097, 1987.

Santee, M. and D. Crisp, The Thermal Structure and Dust Loading of the Martian Atmosphere During Late Southern Summer: Mariner 9 Revisited, Submitted to *J. Geophys. Res*, 1992.

Tiwari, S. N., Models for Infrared Atmospheric Radiation, *Adv. Geophys.*, *20*, 1–85,

1978.

Wyatt, P. J., V. R. Stull, and G. N. Plass, Quasi–Random Model of Band Absorption, *J. Opt. Soc. Am.*, *52*, 1209–1217, 1962.